

Orientation-Dependent Adaptive Antenna for
Low Earth Orbit Satellite Communications

by
Bo Woods

A Thesis submitted to the Faculty of Graduate Studies of
The University of Manitoba
in partial fulfilment of the requirements of the degree of

MASTER OF SCIENCE

Department of Electrical and Computer Engineering
University of Manitoba
Winnipeg

Copyright © 2017 by Bo Woods

Abstract

In remote areas without conventional cellular service, satellite communication is often the only viable option. Handheld devices for use with satellite communication networks require a high transmit power to obtain a reliable signal. The need for a high transmit power makes it difficult for the device to meet specific absorption rate (SAR) restrictions. An adaptive beam forming technique for shaping radiation away from the user's head is proposed. This technique uses a back-to-back patch antenna design with an impedance monitoring based system capable of adaptively controlling the pattern of the antenna. The adaptive antenna system was designed, simulated, fabricated, and measured. The system could detect a head phantom within 3 cm of the antenna. SAR levels were verified to be within safety restrictions at 3 cm through simulation. By turning off the patch facing the user's head when the phone is transmitting, and the user's head is within 3 cm, it was shown that SAR levels could be reduced to safe levels.

Acknowledgements

Firstly, I would like to thank my advisor, Dr. Greg Bridges, for his countless hours of advice and guidance on the thesis. A huge thanks to Tom Tessier, our industry partner, who dedicated many hours to meetings and consultations regarding the thesis. I would like to thank Michael Kenny from Multiband Antennas for donating commercial antennas for testing. A special thanks to Robin Raju for all his guidance using HFSS, general antenna wisdom and conversations, and help using the measurement equipment at the University of Manitoba.

I would like to thank Tyler Teed for his help on using the Satimo near-field measurement system in the University of Manitoba Antenna Lab. A thanks to Kyle Nemez for the use of his phantom for antenna testing. Thanks to Cory Smit in the machine shop for the many hours required for fabricating antennas and other components. Thanks to Sinisa Janjic and Zoran Trajkoski for their help with soldering components and ordering parts. A special thanks to Brad Tabachnick for all his time in helping with the use of the measurement equipment in the Antenna Lab. An acknowledgement and thank you to James Dietrich for his support with debugging HFSS issues. Thanks to Dwayne Chrusch who regularly helped find materials that could be used for antenna construction and measurements. A special thank you to Dr. Puyan Mojabi and Dr. Lot Shafai for their general wisdom and advice on antenna design and measurement.

I would like to thank the Natural Sciences and Engineering Research Council of Canada and the University of Manitoba for their financial support. Finally, I would like to thank my family, friends, and colleagues for their continual support throughout my Master's degree.

Table of Contents

Abstract	ii
Acknowledgements	iii
Table of Contents	iv
List of Tables	vi
List of Figures	vii
List of Symbols and Acronyms	xi
Chapter 1: Introduction	1
1.1. Motivation and Techniques for Reducing SAR Levels	1
1.2. Thesis Objectives	8
1.3. Thesis Contributions	8
1.4. Thesis Overview	10
Chapter 2: Analysis and Performance Tests of Commercial Antenna Systems	11
2.1. Antennas Used in Mobile Satellite Communication Devices	11
2.2. Measurement and Performance Analysis	12
2.3. Conclusion	18
Chapter 3: Adaptive PEC/PMC Beam Shaping	20
3.1. Overview	20
3.2. Normal-Mode Helix	20
3.2.1. Theory	20
3.2.2. Design and Simulation	23
3.2.3. Fabrication, Reflection Coefficient, and Radiation Pattern Measurements	29
3.2.4. Comparison with the Commercial CSA Stubby Antenna	34

3.3. Adaptive PEC/PMC Beam Shaping Technique	35
3.4. Adaptive PEC/PMC Beam Shaping Simulation	37
3.5. AMC Impedance Surface	42
3.6. Conclusion	46
Chapter 4: Back-to-Back Patch Antenna	48
4.1. Overview	48
4.2. Background Theory	49
4.3. Design and Simulation	51
4.4. Fabrication, Reflection Coefficient, and Radiation Pattern Measurements	59
4.5. Human Head Influence on the Radiation Pattern Using a Crude Phantom	70
4.6. SAR Level Simulation	73
4.7. Beam Shaping Using Feed Phasing	75
4.8. Conclusion	79
Chapter 5: Impedance Monitoring System	81
5.1. Overview	81
5.2. Reflection Coefficient Sensitivity	81
5.3. Operation of the Monitoring System	84
5.4. Conclusion	88
Chapter 6: Conclusion	90
6.1. Future Work	91
References	93
Appendix A: Additional Commercial Antenna Measurements	97

List of Tables

1.1. SAR restrictions for 100 kHz – 6 GHz	3
2.1. Measured CSA Stubby 1 antenna specifications	18
3.1. Simulated normal-mode helix antenna specifications	27
3.2. Measured normal-mode helix antenna specifications	34
4.1. Reflection coefficient and negative insertion loss of the 180° hybrid coupler	61
4.2. Back-to-back patch antenna with both patches on specifications	70
5.1. Resonant frequency shift in the presence of the “blue phantom” with both patches on	83

List of Figures

1.1. Cell phone communications contrasted with satellite communications	1
1.2. Illustration of the optimal coverage for the Iridium satellite network	3
1.3. Concept diagram of adaptive beam shaping approach	7
2.1. CSA Stubby 1 and 2	13
2.2. Reflection coefficient measurement setup	13
2.3. CSA Stubby 1 measured reflection coefficient	14
2.4. CSA Stubby 2 measured reflection coefficient	14
2.5. CSA Stubby 1 radiation pattern measurement setup	15
2.6. CSA Stubby 1 gain measurement	16
2.7. CSA Stubby 1 measured axial ratio bandwidth	17
3.1. Helix geometry	21
3.2. Operation of a helical antenna	21
3.3. HFSS model of the normal-mode helix with a short coaxial feed	24
3.4. Simulated normal-mode helix reflection coefficient	25
3.5. Normal-mode helix gain simulation	26
3.6. Simulated normal-mode helix axial ratio bandwidth	26
3.7. Cross sectional slice of the length of a quarter wave sleeve balun	27
3.8. Reflection coefficient simulation of the normal-mode helix with a 5 cm long coax feed	29
3.9. Fabricated normal-mode helix with the balun installed on the feed	31
3.10. Normal-mode helix reflection coefficient measurement	31
3.11. Normal-mode helix radiation pattern measurement setup	32

3.12. Normal-mode helix gain measurement	33
3.13. Normal-mode helix measured axial ratio bandwidth	34
3.14. An illustration of image theory	36
3.15. HFSS model of the PEC/PMC reflector system with a normal-mode helix	37
3.16. Gain simulation of the normal-mode helix with the adaptive PEC/PMC beam shaping device in the $\phi = 0^\circ$ cut with $0^\circ < \theta < 360^\circ$	39
3.17. Simulated axial ratio bandwidth of the normal-mode helix with the adaptive PEC/PMC beam shaping device turned on	39
3.18. Illustration of the on/off controls of the adaptive PEC/PMC beam shaping device	40
3.19. Illustration of how the adaptive PEC/PMC beam shaping device would operate with a human user	41
3.20. AMC impedance surface model designed in HFSS	44
3.21. Simulation of the reflection coefficient for the AMC impedance surface	45
4.1. Patch antenna fringing fields	49
4.2. Excitation of degenerate modes on a square patch antenna	50
4.3. Illustration of how circular polarization is generated by truncating the corners of a square patch antenna	51
4.4. Design of one element of the back-to-back patch antenna	54
4.5. HFSS model of the back-to-back patch antenna	54
4.6. Simulated back-to-back patch antenna reflection coefficient	55
4.7. Back-to-back patch antenna gain simulation with both patches on	56
4.8. Back-to-back patch antenna gain simulation with the $+\hat{y}$ -patch on the $-\hat{y}$ -patch off	57

4.9. Simulated back-to-back patch antenna axial ratio bandwidth	58
4.10. Identical fabricated patch antenna elements	59
4.11. Block diagram of VNA measurement setup	60
4.12. 180° hybrid coupler under test on the VNA	61
4.13. Back-to-back patch antenna reflection coefficient measurement setup	62
4.14. Reflection coefficient of the back-to-back patch antenna measured on the VNA	63
4.15. Back-to-back patch antenna radiation pattern measurement setup	65
4.16. Back-to-back patch antenna gain measurement with both patches on	67
4.17. Back-to-back patch antenna gain measurement with the $+\hat{y}$ -patch on the $-\hat{y}$ -patch off	68
4.18. Back-to-back patch antenna measured axial ratio bandwidth	69
4.19. Complex permittivity of the “blue phantom”	71
4.20. Back-to-back patch antenna radiation pattern measurement setup with the “blue phantom” used to roughly emulate the human head	72
4.21. Gain measurement with the “blue” phantom 1 mm away from the back-to-back patch antenna in the $\phi = 90^\circ$ cut with $0^\circ < \theta < 360^\circ$	72
4.22. 3D SAR level simulation using a homogenous ellipsoid model of the human head	74
4.23. SAR level simulation along the y -axis using a homogenous ellipsoid phantom at various distances away from the back-back patch antenna	74
4.24. 3D simulation of different feed phasing for the back-to-back patch antenna	76
4.25. Feed phasing effects on shaping the null of the back-to-back patch antenna in the xz -plane	77
4.26. Analysis of the beam steering using feed phasing by looking at the phase of the electric field in the xz -plane	78

5.1. Measurement setup with the “blue phantom” to investigate the reflection coefficient sensitivity of the back-to-back patch antenna	82
5.2. Reflection coefficient in the presence of the “blue phantom” with both patches on	82
5.3. One patch on and one patch off reflection coefficient measured on the VNA	84
5.4. An example of a miniaturized version of the back-to-back patch antenna in a phone with a user making a call	85
5.5. High-level block diagram of the impedance monitoring system	86
5.6. State diagram of the operation of the impedance monitoring system	88
A.1. (a) CSA Stubby mounted on styrofoam while under test. (b) Embedded CSA Stubby mounted on styrofoam while under test.	97
A.2. CSA Stubby 3 reflection coefficient measured on the VNA	98
A.3. CSA Stubby 4 reflection coefficient measured on the VNA	98
A.4. CSA Stubby 5 reflection coefficient measured on the VNA	99
A.5. Embedded CSA Stubby 1 reflection coefficient measured on the VNA	99
A.6. Embedded CSA Stubby 2 reflection coefficient measured on the VNA	100
A.7. Embedded CSA Stubby 3 reflection coefficient measured on the VNA	100

List of Symbols and Acronyms

LEO	Low Earth Orbit
SAR	Specific Absorption Rate
RF	Radio Frequency
GEO	Geosynchronous Earth Orbit
EBG	Electromagnetic Bandgap
AMC	Artificial Magnetic Conductor
PMC	Perfect Magnetic Conductor
ICAO	International Civil Aviation Organization
AR	Axial Ratio
RHCP	Right-Hand Circular Polarization
VNA	Vector Network Analyzer
U of M	University of Manitoba
$ S_{ii} $	Reflection Coefficient Magnitude
HFSS	High Frequency Structural Simulator
PEC	Perfect Electric Conductor
EIL	Electromagnetic Imaging Lab
AUT	Antenna Under Test
HPBW	Half-Power Beamwidth
LHCP	Left-Hand Circular Polarization
ATK	Antenna Toolkit
TM	Transverse Magnetic
IL	Insertion Loss
PET	Polyethylene Terephthalate

Chapter 1

Introduction

1.1. Motivation and Techniques for Reducing SAR Levels

In remote areas without conventional cellular service there is a need for alternative communications. Many of the applications range from simple data transmission to emergency locating, which includes military, commercial, and recreational users. Satellite communications is the only viable option in remote areas [1]. **Low earth orbit (LEO)** communications, such as Iridium, require the transmitting antenna to radiate a substantial amount of power to obtain a reliable signal. This makes adherence to being within maximum radiation exposure levels difficult to achieve [2, 3]. The power radiated by a handheld cell phone and satellite phone is contrasted in Figure 1.1.

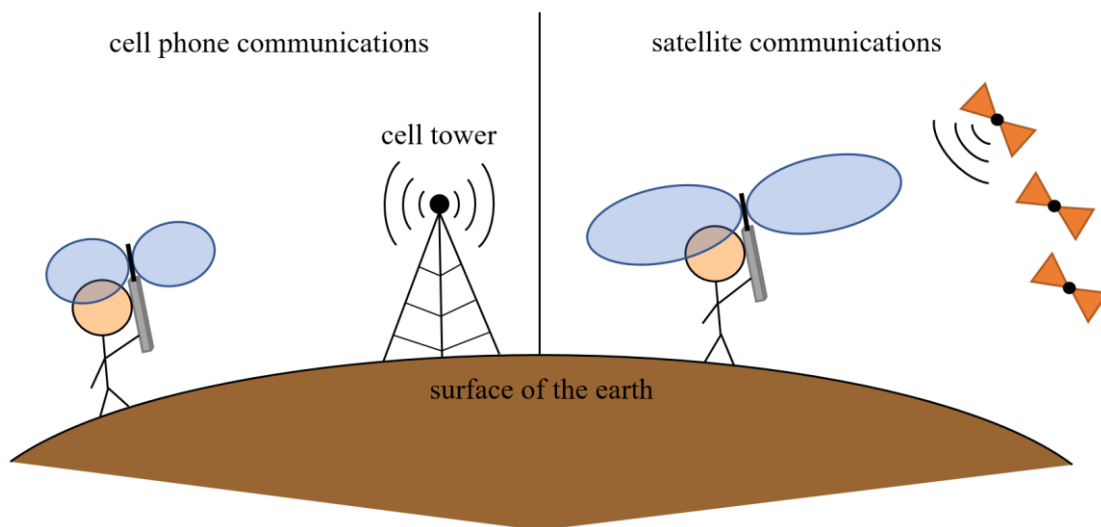


Figure 1.1 *Cell phone communications contrasted with satellite communications.*

Specific absorption rate (SAR) levels are a way of characterizing how much radiation is absorbed in a lossy dielectric such as the human body. SAR restrictions for different parts of the human

body are specified in Health Canada's Safety Code 6 [4]. Due to the high **radio frequency** (RF) power required for Iridium communications, it is possible that the radiation emitted from the antenna may not be within SAR limitations. Current mobile handheld satellite devices often require the user to extend the antenna a certain distance above their head to meet SAR restrictions, which is impractical for creating a compact phone. Assuming that the phone would never be placed near the head, another method around meeting SAR regulations includes restricting the phone use to only data and text. Neither of these methods are optimal. Therefore, compact methods of reducing SAR levels will be explored in this thesis.

Modern commercial mobile phones have a high emphasis placed on compact size. The Iridium satellite system is attractive since it uses multiple high-gain phased arrays on each satellite, which allow for the use of small lightweight handsets to be used on the ground [5]. The Iridium satellite service was initially launched in May 1998 [6]. The network consists of 66 satellites at a height of 780 km [5, 7]. Compared to the **geosynchronous earth orbit** (GEO) at 35,800 km, the proximity of Iridium to the earth provides a much lower propagation delay. The satellites traverse a polar orbit and can provide complete global coverage. It is important for the mobile handheld antenna operating on the Iridium system to have good coverage across the horizon as shown in Figure 1.2. This is because satellite coverage drops to less than 20% as the elevation angle with respect to the horizon increases beyond 40° [8]. The Iridium network operates from 1616 – 1626.5 MHz with a total of 240 channels of 41.67 kHz each [6]. This leaves room for about 2 kHz of guard between each channel.

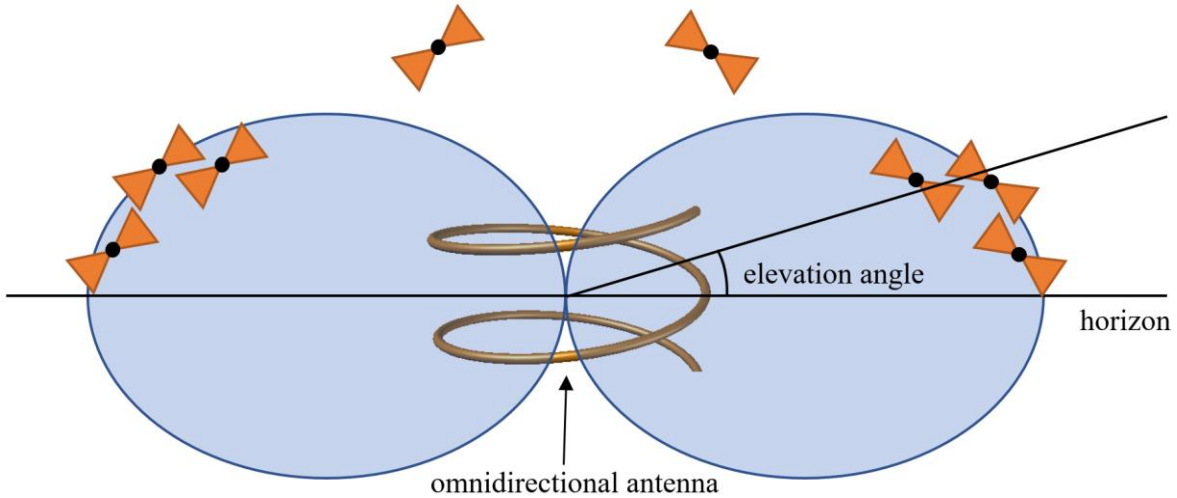


Figure 1.2 *Illustration of the optimal coverage for the Iridium satellite network.*

Typical Iridium handheld devices have a transceiver output power capable of outputting 2 W to the antenna feed network [9]. The SAR restriction of interest for this thesis is the peak averaged SAR for the head in an uncontrolled environment, which is restricted to $1.6 \frac{W}{kg}$ averaged over 1 g of tissue as shown in Table 1.1. A controlled environment is one where the RF field intensities have been well-characterized and the person is aware of the health risks associated with being in that environment. The average consumer is almost always going to be in an uncontrolled environment.

Table 1.1 *SAR restrictions for 100 kHz – 6 GHz [4].*

Condition	Uncontrolled Environment	Controlled Environment
Peak averaged SAR for the head, neck and trunk, averaged over 1 g of tissue	$1.6 \frac{W}{kg}$	$8 \frac{W}{kg}$
Peak averaged SAR in the limbs averaged over any 10 g of tissue	$4 \frac{W}{kg}$	$20 \frac{W}{kg}$

The industry standard IEEE P1528 method of calculating SAR is shown in (1.1) [10]. The local SAR value over a lossy dielectric object is calculated and is then averaged over 1 g or 10 g cubes of tissue. In (1.1), ΔV is the volume of a cube of tissue [m^3], \vec{E} is the electric field vector [$\frac{\text{V}}{\text{m}}$], \vec{J}^* is the conjugate of the volume current density [$\frac{\text{A}}{\text{m}^2}$], ρ is the mass density of the tissue [$\frac{\text{kg}}{\text{m}^3}$], and σ is the conductivity of the tissue [$\frac{\text{S}}{\text{m}}$].

$$\text{SAR} = \frac{1}{\Delta V} \int_V \frac{\vec{E} \cdot \vec{J}^*}{2\rho} dV = \frac{1}{\Delta V} \int_V \frac{\sigma |\vec{E}|^2}{2\rho} dV \quad \text{units in } \frac{\text{W}}{\text{kg}} \quad (1.1)$$

Since power is proportional to $|\vec{E}|^2$, we can determine the SAR level for different input powers using the following approximation:

$$\text{SAR}_x \approx \frac{P_x}{P_{\text{meas}}} \text{SAR}_{\text{meas}} \quad (1.2)$$

In [10], the peak SAR level was measured for a quadrifilar helical antenna, a typical antenna found in mobile Iridium handheld devices. For an output power level of 370 mW, the peak SAR level at the Iridium center frequency of 1621 MHz was measured to be $1.547 \frac{\text{W}}{\text{kg}}$ using a head phantom [10]. Using (1.2), the SAR level for an output power level of 2 W would be $8.36 \frac{\text{W}}{\text{kg}}$, which is well above the restriction of $1.6 \frac{\text{W}}{\text{kg}}$ for an uncontrolled environment. Therefore, to safely take advantage of the maximum output power capability of an Iridium handheld device, a method

of reducing SAR levels is required. To meet the demands of modern commercial phones, the method should be compact and low-cost.

There are several techniques that have been used to reduce SAR levels in mobile phones. The simplest way to reduce SAR levels is to increase the distance between the antenna and user's head. Due to the commercial demand for thinner and thinner phones, increasing the distance is not a practical option. Some alternate methods for reducing SAR levels using shielding techniques were discussed in [11]. The authors discuss using ferrite loading, **electromagnetic bandgap** (EBG)/**artificial magnetic conductor** (AMC) based surfaces, and adaptive beam shaping. All three of these methods were explored in this thesis.

Ferrite sheets can be placed parallel to the electric field of the source to reduce radiation towards the user. The ferrite acts as a good magnetic conductor, which has image currents in phase with the parallel source. See Figure 3.14 for an illustration. This shapes the radiation away from the sheet, which protects the user from harmful exposure levels and improves the radiation away from the user. SAR levels were reduced by up to 50% in [12] using a 4.5×5 cm sheet of ferrite. Unfortunately, ferrite is not commonly available in the GHz frequency range, making it an impractical and costly choice for mass production in phones. This is discussed in further detail in Section 3.3.

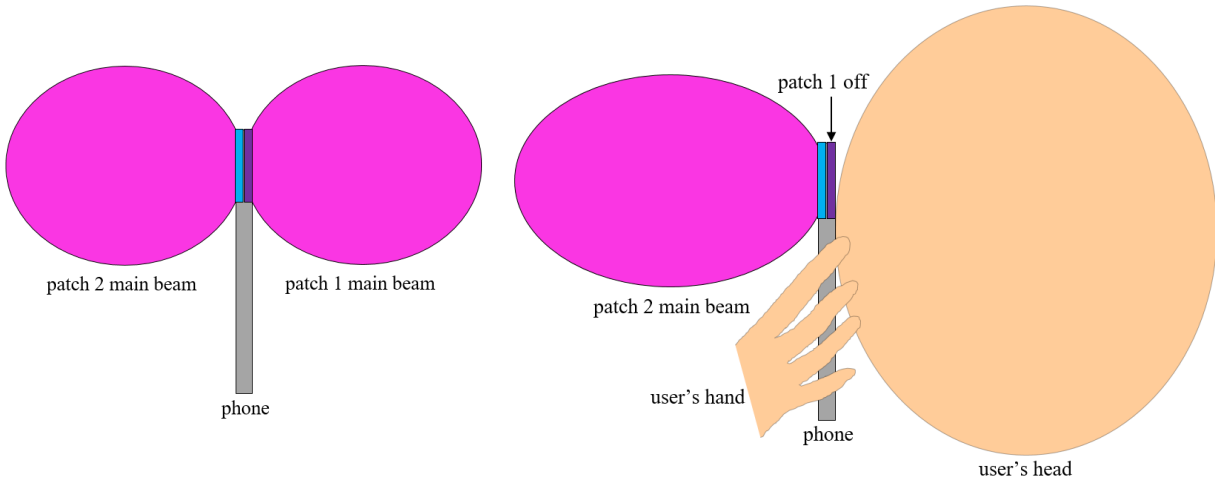
AMC impedance surfaces can mimic **perfect magnetic conductors** (PMCs) over a designed bandwidth [13]. This is done by texturing metallic periodic resonant structures over a grounded substrate [14]. This allows for a magnetic conducting surface in the GHz range to be realized

practically. Different variations of AMC surfaces are discussed in [13–15]. AMC impedance surfaces have been shown to reduce SAR levels by up to 75% while having a negligible effect on the antenna efficiency [16]. AMC impedance surfaces were investigated in more detail in Section 3.5.

Adaptive beam forming can be done using a passive or active approach. A common passive approach is to use a resonant length parasitic wire to shape the main beam of the antenna as discussed in [17–21]. The downside to this approach for a handheld device is that a $\frac{\lambda}{4}$ spacing is required between the active antenna and the parasitic element for the main beam to be properly directed. An active approach can also be done using a two-element phased array. In [22], a simple $\frac{\lambda}{4}$ length monopole array was used to reduce SAR levels by up to 85%. The main disadvantage of this technique is the amount of space required for the multiple elements.

It should be noted that one of the main challenges to shaping the radiation pattern of antennas for satellite communication applications is due to the requirement of circular polarization. This requires a reflecting device that can maintain circular polarization. Since the orientation of the user relative to the satellites is random, circular polarization is necessary to ensure a consistently reliable signal. If linear polarization was used, it is possible that no signal would be received if the antenna onboard the satellite was perpendicular to the mobile user’s antenna polarization. Electromagnetic waves propagating through the ionosphere near 1 GHz also experience significant Faraday rotation due to the presence of Earth’s magnetic field in the ionized medium. This causes a change in a linear polarized wave’s orientation [23, 24]. This effect is eliminated with the use of circular polarization.

Figure 1.3 shows a concept diagram of the adaptive beam shaping approach presented in this thesis.



(a) Both antennas on when the phone is away from the head (b) Patch 1 is turned off when the phone is near the user's head

Figure 1.3 *Concept diagram of adaptive beam shaping approach.*

This approach is based on a back-to-back patch antenna design where one patch would face outwards from the front of the phone and the other patch would face outwards from the back of the phone. The on/off control of the patch facing the user's head (patch 1 in Figure 1.3) would be controlled by an impedance monitoring system that could detect a measurable change in the input impedance of the antenna when a user's head was nearby. When the satellite phone is not transmitting, the power levels being received are very low due to the large path loss between the satellite and the user. Therefore, both patches would be left on to ensure the most optimal coverage as shown in Figure 1.3(a). If the user placed the phone near the head to make or receive a call, patch 1 would be turned off to minimize the radiation emitted towards the head. This will be

discussed in further detail in Chapter 5. The advantage of the presented approach is its ability to be easily miniaturized to fit within a mobile handheld device.

1.2. Thesis Objectives

This thesis had two main objectives. The first objective was to determine a method for directing the radiation emanated by an antenna away from the user's body to reduce human field exposure levels. The second objective was to use the antenna's impedance as a method of detecting the presence of a human head by implementing an adaptive feed network to control the antenna's main beam. Since there were no well-defined standards for handheld satellite communication devices, the **International Civil Aviation Organization** (ICAO) manual for Iridium communications was used as a guideline [25]. The manual suggested that the gain of the antenna should be greater than -3.5 dB and the **axial ratio** (AR) should be less than 4 dB in the direction of maximum radiation. The antenna was required to operate across the Iridium frequency bandwidth of 1616 – 1626.5 MHz and provide **right-hand circular polarization** (RHCP). The pattern of the antenna should also be as omnidirectional as possible to optimize the signal with the Iridium satellites. The SAR levels for the human head should remain below $1.6 \frac{\text{W}}{\text{kg}}$ at all times [4].

1.3. Thesis Contributions

Tom Tessier, the president and founder of Solara Remote Data Delivery Incorporated, had monthly meetings with Dr. Bridges and myself to discuss the radiation requirements for antennas used for current mobile Iridium communication devices. Solara is a Canadian company based out

of Winnipeg that produces handheld satellite communication devices for use with the Iridium satellite system. Tom also provided us with some industry standard antennas for Iridium and GPS applications. Solara was interested in a method for reducing radiation exposure to the human user to ensure that their handheld devices were meeting SAR requirements. The commercial CSA Stubby antennas measured in Section 2.2 were donated by Multiband Antennas. Multiband Antennas is a company that specializes in designing cutting edge antennas for use with Iridium, Orbcomm, Globalstar, and Thuraya networks.

The Keysight **vector network analyzer** (VNA) model E5063A in the **University of Manitoba** (U of M) RF Lab was used for all **reflection coefficient magnitude** ($|S_{ii}|$) measurements. The Satimo spherical near-field system, which was housed in one of the anechoic chambers in the U of M Antenna Lab, was used for all antenna pattern measurements. I was responsible for carrying out all the antenna measurements done on the VNA and Satimo system. Brad Tabachnick, the lab technician for the Antenna Lab at the U of M, helped me with the antenna mounting for all the measurements done in the Satimo system. The normal-mode helix and back-to-back patch antennas designed in this thesis, including the feed networks and balun, were designed by myself. The antenna simulations were all done using Ansys **High Frequency Structural Simulator** (HFSS) and were performed by myself with help from Robin Raju, a PhD student of Dr. Bridges. I also designed and simulated the adaptive **perfect electric conductor** (PEC)/PMC beam shaping device discussed in Chapter 3. Cory Smit, in the machine shop at the U of M, was responsible for fabricating the plexiglass helix mold and the balun in Chapter 3. Cory also fabricated the back-to-back patch antenna discussed in Chapter 4. Zoran Trajkoski, from the machine shop at the U of M, soldered the SMA connectors onto the fabricated back-to-back patch antenna. Kyle Nemez, an

MSc student in the **Electromagnetic Imaging Lab (EIL)** at the U of M, provided us with one of his phantoms (“blue phantom”) for simulating a nearby human head for measurements done in Chapter 4 and 5. Lastly, I designed and tested the impedance monitoring system discussed in Chapter 5.

1.4. Thesis Overview

This thesis is organized into six chapters. Chapter 1 gives an introduction on Iridium communications and the need to reduce SAR levels in handheld satellite communication devices. In Chapter 2, the current antennas used for mobile satellite communication applications were explored. A commercial state of the art antenna was measured to develop a blueprint of the radiation properties required in a mobile handheld satellite communication device. This allowed for a simpler helical antenna model with similar radiation properties to be generated in software to explore the different beam shaping techniques discussed in Chapter 3. A normal-mode helix was successfully designed in Chapter 3 and was used to simulate the adaptive PEC/PMC beam shaping technique proposed in Section 3.3. AMC impedance surfaces were also explored through simulation. Chapter 4 investigates a back-to-back patch antenna design. The back-to-back patch antenna can turn one of the patches off to reduce radiation towards the human user. The SAR levels of the back-to-back patch were also simulated in HFSS using a homogenous phantom of the human head. Beam shaping by feeding the patches with different phases was explored as well. In Chapter 5, an impedance monitoring system was investigated for adaptively controlling the pattern of the back-to-back patch antenna. The thesis is concluded in Chapter 6 where future work is also addressed.

Chapter 2

Analysis and Performance Tests of Commercial Antenna Systems

2.1. Antennas Used in Mobile Satellite Communication Devices

The most commonly used antenna for satellite communications is the quadrifilar helical antenna [26]. The quadrifilar helix is attractive due to its robust circular polarization, wide beamwidth, compact size, and insensitivity to nearby objects. The quadrifilar helix operates in the axial-mode, which means that the main beam of the antenna radiates on the axis of the helix. This is also known as the end-fire mode and will be discussed in further detail in Section 3.2. See Figure 3.2 for an illustration of the axial-mode radiation pattern. A quadrifilar helix typically provides a maximum gain of +1 to +6 dB [26–28]. A method of further reducing the size of the quadrifilar helix by up to 53% was proposed in [26]. By meandering the four line elements of the antenna, the resonance of the structure could be lowered while decreasing the axial length of the antenna. A disadvantage of the meandering technique was that the maximum gain was lowered by about 2.5 dB in comparison to a standard quadrifilar helix design.

Microstrip patch antennas are also used for satellite communications due to their low-cost, thin profile, and robustness [5]. Patch antennas are commonly miniaturized by using a high dielectric material such as ceramic. The problem with using high permittivity materials is that the bandwidth of the patch is inversely proportional to ϵ_r [29]. Higher ϵ_r materials will cause the fields of the patch antenna to become more tightly bound, which will reduce the radiation efficiency and lead to greater losses [29]. Consequently, there is a trade-off between the gain and size of the patch antenna.

The next section explores the performance of a state of the art dipole-helical based antenna. This antenna is attractive due to its small height of 2.7 cm, lightweight, low-cost, omnidirectional pattern, and RHCP. It will be used as a benchmark for designing a software model that can mimic similar radiation characteristics for exploring different adaptive beam shaping techniques through simulation as discussed in Chapter 3.

2.2. Measurement and Performance Analysis

A measurement and performance analysis was done on the CSA Stubby model antenna from Multiband Antennas to create a blueprint of its radiation properties. The CSA Stubby antenna has a compact state of the art dipole-helical based design, which provides RHCP for satellite communication applications. By characterizing its radiation properties, a simpler helical antenna could be modelled in software to match its performance to simulate different adaptive beam shaping techniques discussed in Chapter 3. This would ensure these techniques were being tested with an antenna that had industry standard radiation properties. Two identical CSA Stubby antennas are shown in Figure 2.1. The pattern is omnidirectional and designed to have maximum radiation in the broadside direction to communicate with satellites that are just above the horizon. As mentioned in Chapter 1, satellite coverage drops to less than 20% as the elevation angle with respect to the horizon increases beyond 40° [8]. Therefore, it is advantageous to have an antenna pattern with maximum gain near the horizon to optimize coverage.

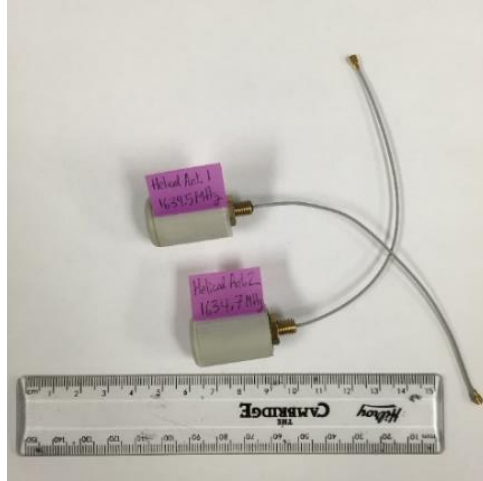


Figure 2.1 *CSA Stubby 1 and 2.*

The reflection coefficient measurement setup for the CSA Stubby is shown in Figure 2.2. The antenna was mounted on styrofoam, which had a permittivity close to free space so it would not influence the reflection coefficient measurement.

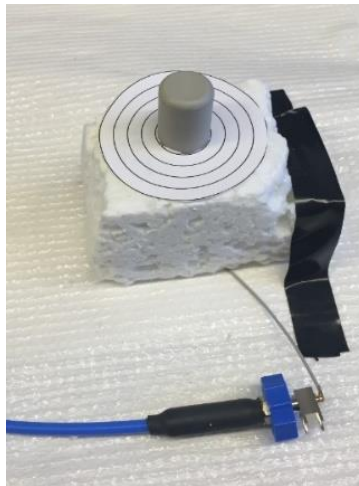


Figure 2.2 *Reflection coefficient measurement setup.*

The resonant frequency of CSA Stubby 1 was measured to be 1639.5 MHz with a reflection coefficient of -12.7 dB as shown in Figure 2.3. The resonant frequency of CSA Stubby 2 was measured to be 1634.75 MHz with a reflection coefficient of -13.88 dB as shown in Figure 2.4.

The edges of the Iridium frequency band have been shown on Figures 2.3 and 2.4 for convenience (1616 MHz and 1626.5 MHz). Both antennas are slightly detuned above the Iridium frequency band.

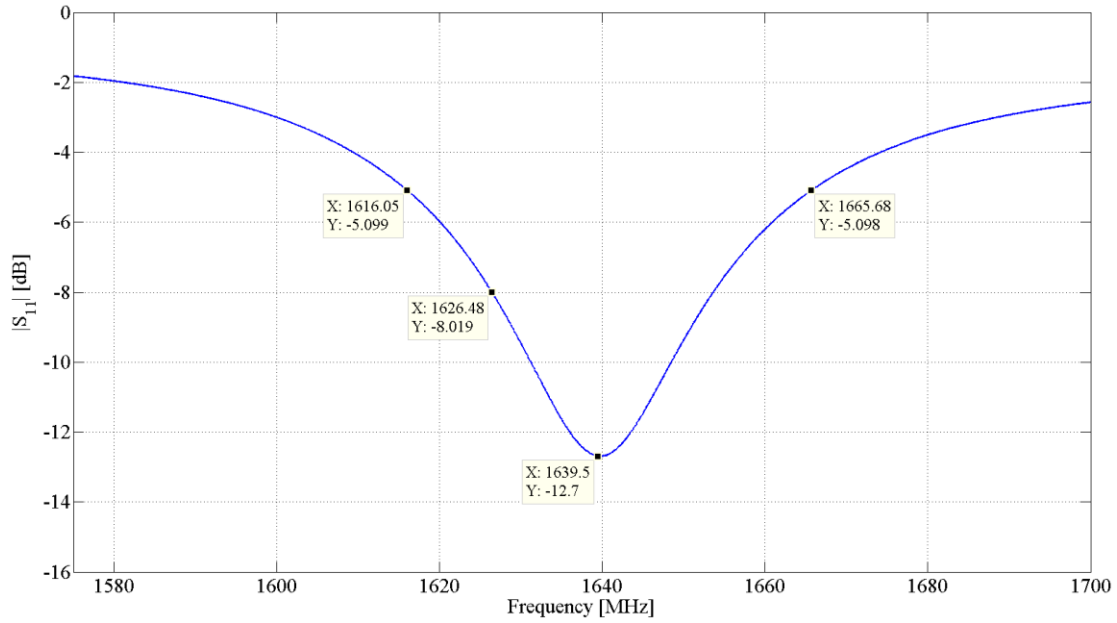


Figure 2.3 *CSA Stubby 1 measured reflection coefficient.*

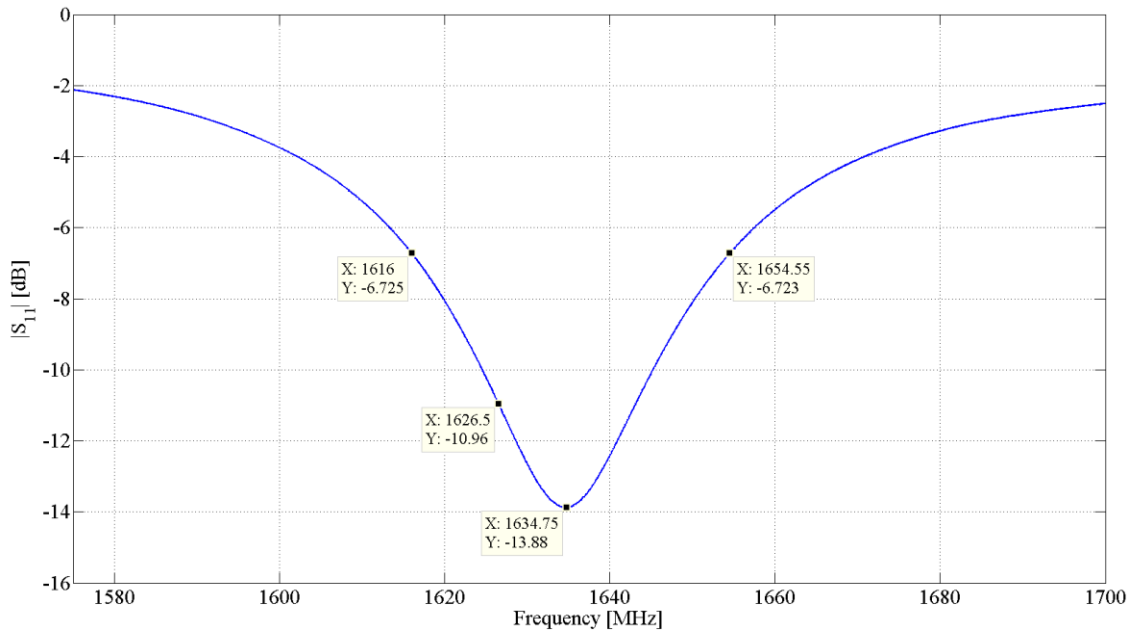


Figure 2.4 *CSA Stubby 2 measured reflection coefficient.*

The CSA Stubby 1 was mounted inside the Satimo spherical near-field system for radiation pattern measurement. The measurement setup is shown in detail in Figure 2.5.

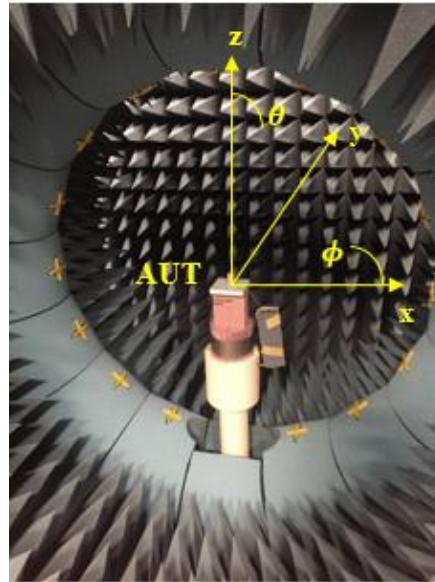
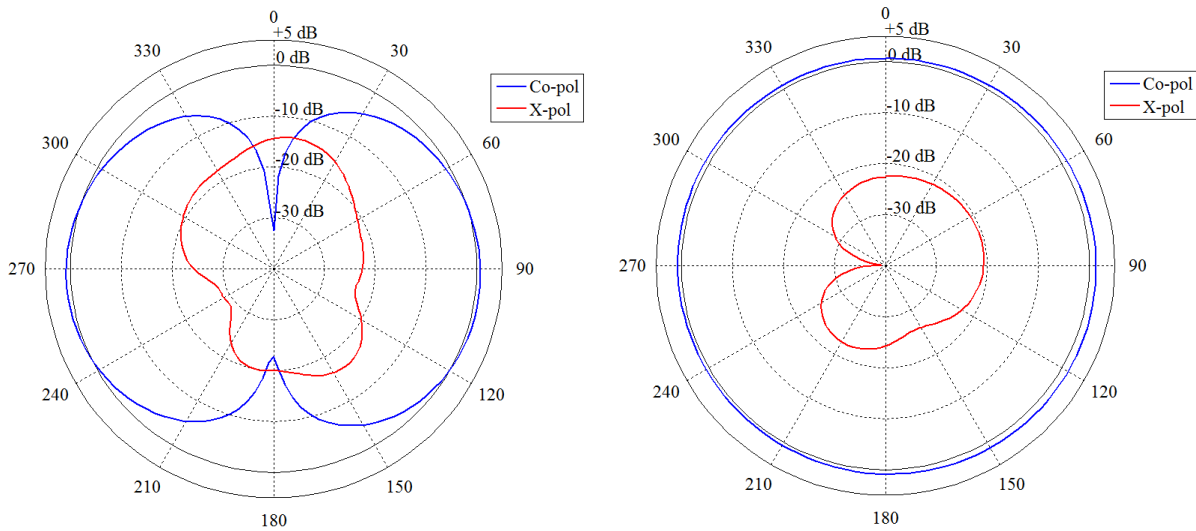


Figure 2.5 *CSA Stubby 1 radiation pattern measurement setup.*

The Satimo system had 15 crossed-dipole probes evenly spaced 22.5° around an arch. The **antenna under test** (AUT) was rotated to obtain a complete near-field distribution. Post processing software then applied a near-field to far-field transformation, which allowed us to extract the far-field radiation pattern of the AUT. The Satimo system had a gain accuracy of approximately ± 2 dB. A frequency sweep of 1600 – 1650 MHz with a step size of 1 MHz was used to determine the far-field radiation pattern. The maximum gain of CSA Stubby 1 occurred at 1632 MHz and the radiation patterns were plotted at this frequency in Figure 2.6. It is important to note that the maximum gain did not occur at the CSA Stubby 1 resonant frequency of 1639.5 MHz that was measured on the VNA. Since we were unable to measure the input impedance of our AUT in the Satimo set up, it is possible that a device before the AUT was causing a slight frequency shift. Current also peaks at the resonant frequency, therefore, it is possible that

a device in the matching network or external circuitry may be introducing some losses. These losses would reduce the measured gain at the resonant frequency.

The gain in the elevation cut, $\phi = 0^\circ$, was directional with maximums broadside to the antenna as shown in Figure 2.6(a). The **half-power beamwidth** (HPBW) was determined from Figure 2.6(a) and was found to be 90° .



(a) $\phi = 0^\circ$ cut with $0^\circ < \theta < 360^\circ$

(b) $\theta = 90^\circ$ cut with $0^\circ < \phi < 360^\circ$

Figure 2.6 CSA Stubby 1 gain measurement. The co-polarization is with respect to a RHCP receiver and the cross-polarization is with respect to a LHCP receiver.

The gain in the broadside direction, $\theta = 90^\circ$ cut, is shown in Figure 2.6(b) and was uniform with a value of approximately +1 dB. Since the CSA Stubby model was supposed to have RHCP, so the gain was measured with respect to an RHCP receiver to determine the co-polarization and with respect to a **left-hand circular polarized** (LHCP) receiver to determine the cross-polarization. As expected, the gain was uniform in the broadside direction ($\theta = 90^\circ$ cut) and directional in the elevation cut ($\phi = 0^\circ$ cut), therefore, the pattern was omnidirectional.

Figure 2.7 shows the axial ratio bandwidth of the antenna in the direction of maximum radiation ($\theta = 90^\circ, \phi$) across 1600 – 1650 MHz. The axial ratio is defined as the ratio of $\frac{|E_\theta|}{|E_\phi|}$, where an AR = 0 dB indicates a perfectly circularly polarized antenna. A mobile user’s antenna is generally required to have an AR < 4 dB for Iridium satellite communications [25]. The axial ratio across the Iridium frequency band of 1616 – 1626.5 MHz was less than 1.5 dB, which was well below the 4 dB guideline. To further specify the polarization performance, the axial ratio was investigated as the elevation angle was changed at the center frequency. The axial ratio for the CSA Stubby 1 was less than 4 dB for elevation angles less than 55° with respect to the horizon. 55° is well above the 40° elevation angle discussed in Section 1.1 for providing sufficient coverage with the Iridium system. Therefore, the CSA Stubby 1 has adequate circular polarization for Iridium communications. A summary of the CSA Stubby 1 antenna specifications is shown in Table 2.1.

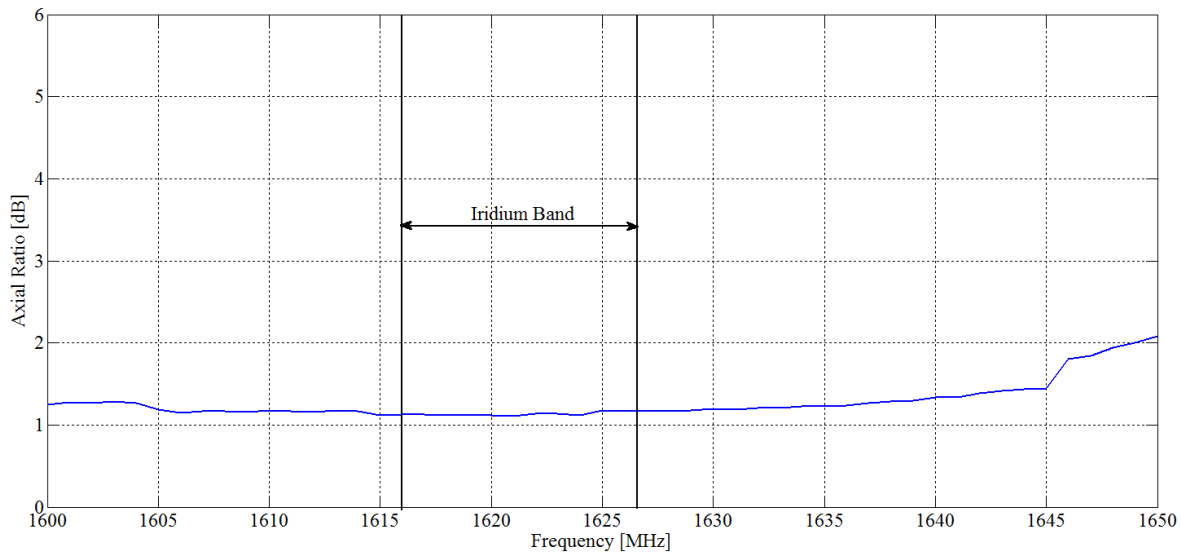


Figure 2.7 CSA Stubby 1 measured axial ratio bandwidth shown for the direction of maximum radiation ($\theta = 90^\circ, \phi$), which was less than 1.5 dB across the Iridium band of 1616– 1626.5 MHz.

Table 2.1 *Measured CSA Stubby 1 antenna specifications.*

Specifications	Value
Center Frequency	1639.5 MHz
–10 dB Bandwidth	17.5 MHz (1631 – 1648.5 MHz)
Maximum Gain	1 dB \pm 2 dB
HPBW	90°
Axial Ratio < 4 dB	Elevation angle < 55°
Polarization	RHCP
Impedance	50 Ω

2.3. Conclusion

We can conclude that both the CSA Stubby antennas had sufficient bandwidth for Iridium satellite communications, however, their resonant frequencies would need to be fine-tuned once installed in a handheld device. Based on the radiation pattern measurements of CSA Stubby 1, the antenna had an acceptable omnidirectional pattern, sufficient gain, and provided the RHCP necessary for Iridium communications. The CSA Stubby was also compact enough to fit into a handheld device. Based on the SAR discussion in Section 1.1, since the CSA Stubby had a similar gain to a typical quadrifilar helical antenna (+1 to +6 dB), the SAR levels of the CSA Stubby would be well above the SAR limit of $1.6 \frac{\text{W}}{\text{kg}}$ for a 2 W transceiver output. Therefore, a method of reducing the radiation towards the human user is still necessary to safely take advantage of the full power capabilities of the typical Iridium handheld device. In the next chapter, a normal-mode helical antenna will be designed to match the radiation properties of the CSA Stubby. The normal-mode helix was chosen due to its compact size and similar radiation pattern to the CSA Stubby. This will allow for a model with industry standard antenna characteristics to be constructed in

software. The adaptive PEC/PMC beam shaping device proposed in the next chapter will then be able to be simulated with an accurate representation of a commercial Iridium antenna.

Chapter 3

Adaptive PEC/PMC Beam Shaping

3.1. Overview

As discussed in Chapter 1, the high transmit power required for handheld satellite communication devices can create a high radiation exposure for a nearby human user. The main challenge for reducing the radiation exposure stems from the circular polarization that is required for satellite communications. Section 3.2 starts with the design of a normal-mode helix, which was used to model the industry standard CSA Stubby antenna discussed in Chapter 2. The normal-mode helix provides us with a direct representation of how the adaptive beam shaping device in Section 3.3 would perform for Iridium communication applications. Section 3.3 starts with the trivial case of shaping a linearly polarized antenna to illustrate the principles of beam shaping. Circular polarization is more complicated to shape because both the E_θ and E_ϕ components needed to be reflected equally to maintain a sufficient axial ratio. This chapter investigates shaping a circularly polarized omnidirectional pattern using image theory concepts to reduce radiation exposure for the human user.

3.2. Normal-Mode Helix

3.2.1. Theory

A helical antenna can operate in many different modes, but the most commonly used modes are the normal-mode and axial-mode [29]. A diagram of the basic helix geometry is shown in Figure 3.1.

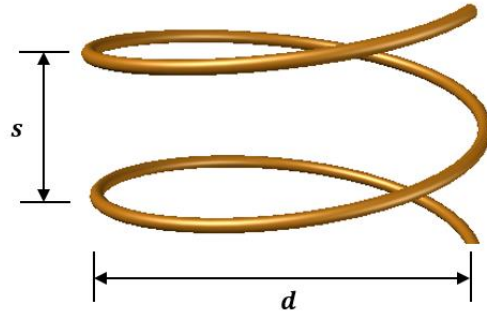


Figure 3.1 Helix geometry.

When the diameter $d < 0.1\lambda$ and the spacing between turns $s < 0.05\lambda$, the helix will operate in the normal-mode with maximum radiation occurring broadside to the antenna [30]. The helix will begin to operate in the axial-mode as the circumference of the helix $C \approx \lambda$. The axial-mode has only one major lobe, which is maximum along the axis of the helix. The axial-mode of operation is also known as the end-fire mode and generally the helix is placed over a ground plane. An illustration of the main beam of these two modes is shown in Figure 3.2.

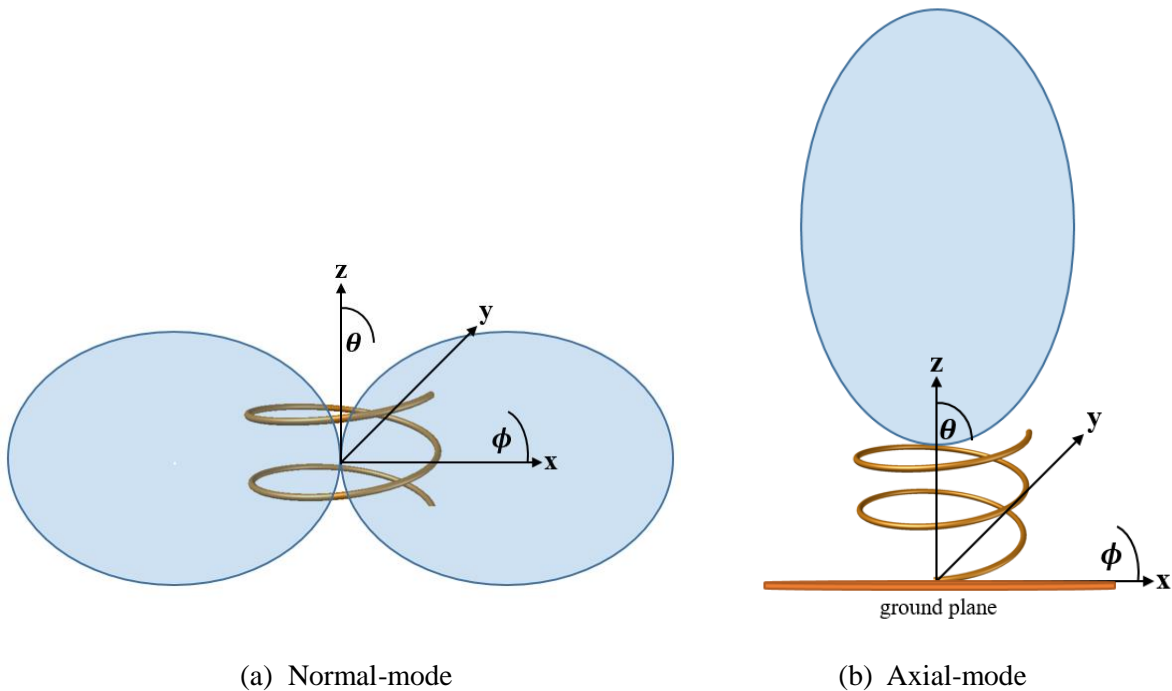


Figure 3.2 Operation of a helical antenna.

A normal-mode helical antenna design was chosen since it mimicked a similar radiation pattern to the commercial CSA Stubby antenna discussed in Section 2.2. Since the CSA Stubby antenna was too complicated to model in software, this allowed for a similar performing antenna to be used in-place of it for simulation. The normal-mode helix was chosen due to its simplistic geometry, omnidirectional pattern, and its ability to provide circular polarization when designed properly. In Section 3.3, the adaptive PEC/PMC beam shaping device could then be simulated with a comparable industry standard antenna model.

The normal-mode helix can be understood as the superposition of infinitesimal electric and magnetic dipoles (infinitesimal current loops). The current, I , along the helix is assumed to be uniform in both amplitude and phase. The electric field equation for the normal-mode helix is shown in (3.1) [31]. N is the number of turns of the helix, μ_0 is the permeability of free space, $\beta = \frac{2\pi}{\lambda}$ is the phase constant, R and θ are the spherical coordinates of the observation point in free space. The $\hat{\theta}$ -component of $\vec{E}_{\text{normal-mode}}$ is due to the vertical spacing between turns of the helix, which is modelled as infinitesimal electric dipoles. The $\hat{\phi}$ -component is due to the loop part of the helix. From (3.1) we can see that the maximum radiation will occur broadside to the antenna when $\theta = \pm 90^\circ$ and the radiation will be minimum when $\theta = 0^\circ, 180^\circ$.

$$\vec{E}_{\text{normal-mode}} = \hat{\theta}E_\theta + \hat{\phi}E_\phi = \frac{N\omega\mu_0 I e^{-j\beta R}}{4\pi R} \left[\hat{\theta}js + \hat{\phi}\beta\pi \left(\frac{d}{2}\right)^2 \right] \sin(\theta) \quad (3.1)$$

Since \vec{E}_θ and \vec{E}_ϕ are 90° out of phase, the antenna will provide circular polarization when $|\vec{E}_\theta| = |\vec{E}_\phi|$. When $|\vec{E}_\theta| = |\vec{E}_\phi|$, (3.1) gives the following relation between the diameter and spacing between turns of the helix:

$$d = \sqrt{\frac{2s\lambda}{\pi^2}} \quad (3.2)$$

For the normal-mode helix to be resonant its total stretched-out length needs to be close to $\frac{\lambda}{2}$. Once the proper length is selected, the position of the feed can be adjusted along the length of the helix to match it to the 50Ω cable. Note that a ground plane cannot be used with a normal-mode helix when circular polarization is desired. This is because the loop part of the helix will have image currents in the opposite direction over a PEC ground plane, causing the E_ϕ -component to go to zero. This was verified by simulation in HFSS.

3.2.2. Design and Simulation

The normal-mode helix was designed in Ansys's HFSS using the **antenna toolkit** (ATK) and then tweaked after until it was tuned to the Iridium frequency band with acceptable circular polarization. Initially, the helix was designed with a very short coaxial feed to simulate optimal feed conditions with minimal interference from the feed. As the coax feed length was increased to a more practical length, it was determined that the helix would require a balun for the antenna to operate properly. A custom quarter wavelength sleeve balun was designed for the coaxial feed in

HFSS. A physical model of the antenna and balun were then constructed in Section 3.2.3 after verifying the reflection coefficient and far-field radiation patterns in HFSS.

The diameter and spacing between turns were chosen so that the helix would be a practical size to build while still having enough turns to obtain a satisfactory pattern and impedance characteristics [30]. The spacing between turns was chosen to be $s = 0.525$ cm, which gave a diameter of $d = 1.4$ cm using (3.2). Both these dimensions satisfied the conditions $s < 0.05\lambda$ and $d < 0.1\lambda$ respectively for exciting the normal-mode of the helix. We recall that the center frequency for the Iridium band is $f_0 = 1621$ MHz, which has a free space wavelength of $\lambda = 18.5$ cm. The helix in Figure 3.3 was designed and simulated in HFSS using a very short coaxial feed. The position of the feed was adjusted until the antenna was matched at the Iridium frequency band.

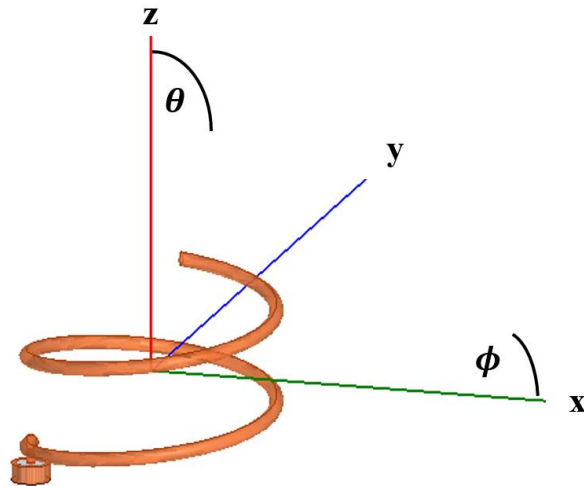


Figure 3.3 HFSS model of the normal-mode helix with a short coaxial feed.

Figure 3.4 shows the simulated reflection coefficient with the resonant frequency and the edges of the Iridium band marked for convenience. The -10 dB bandwidth was 6.5 MHz, which was slightly narrower than the Iridium frequency, but reasonable enough to be used as a basic model.

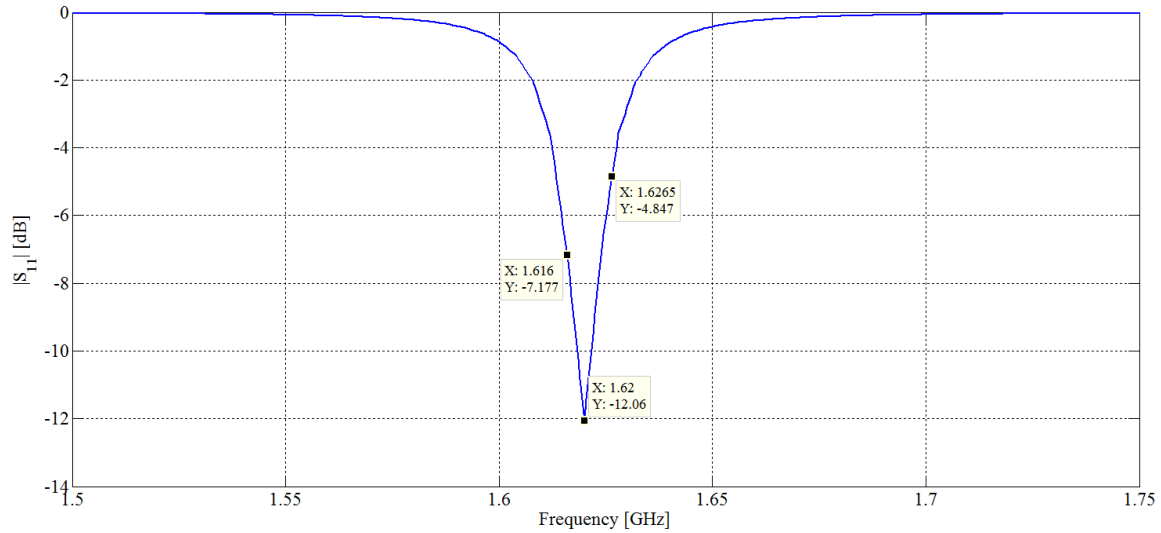
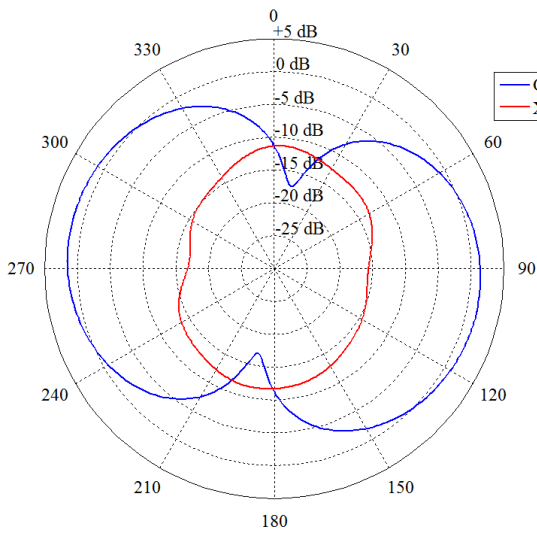


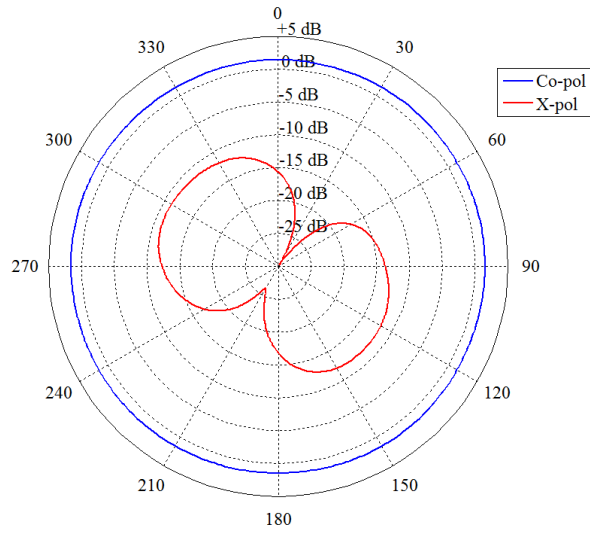
Figure 3.4 *Simulated normal-mode helix reflection coefficient.*

Figure 3.5(a) shows the gain in the elevation cut $\phi = 0^\circ$. Since the helix was designed to have RHCP, the gain with respect to a RHCP receiver shows the co-polarization and the gain with respect to a LHCP receiver shows the cross-polarization. The slight asymmetries in the pattern in Figure 3.5(a) were accounted for by the non-centered feed. Using a horizontal wire to center the feed of the helix was explored in HFSS, however, it did not improve the axial ratio. Figure 3.5(b) shows that the gain was uniform and +2 dB in the broadside direction ($\theta = 90^\circ$ cut).

The axial ratio bandwidth has been plotted in Figure 3.6 in the direction of maximum radiation ($\theta = 90^\circ, \phi$). The simulated axial ratio was less than 2.5 dB across the Iridium bandwidth, which met the requirement of $AR < 4$ dB for Iridium communications. A summary of the simulated normal-mode helix specifications is shown in Table 3.1.



(a) $\phi = 0^\circ$ cut with $0^\circ < \theta < 360^\circ$



(b) $\theta = 90^\circ$ cut with $0^\circ < \phi < 360^\circ$

Figure 3.5 Normal-mode helix gain simulation. The co-polarization is with respect to a RHCP receiver and the cross-polarization is with respect to a LHCP receiver. See Figure 2.6 for comparison with the measured CSA Stubby pattern.

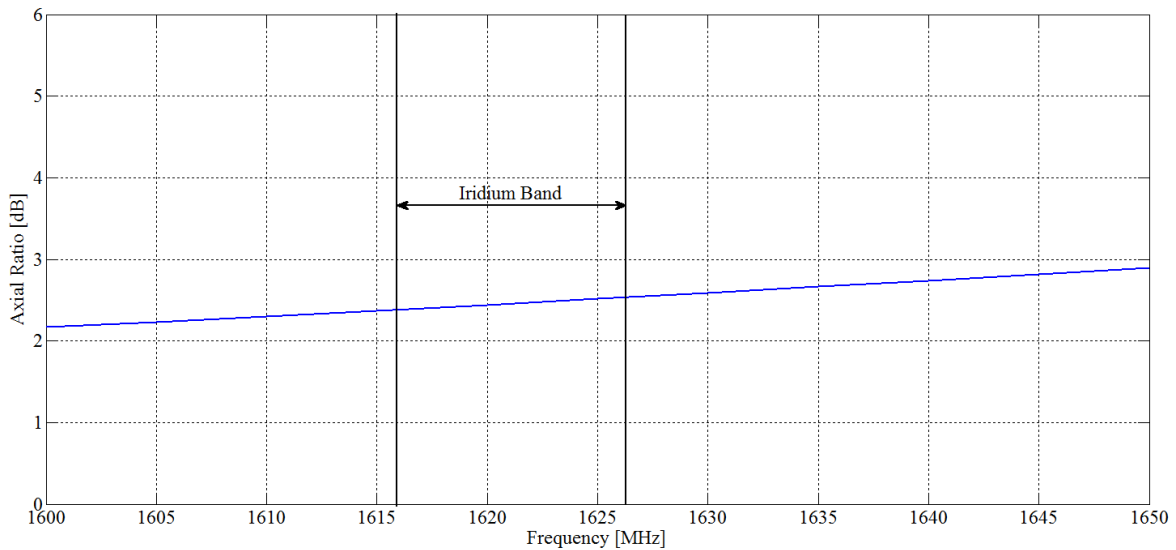


Figure 3.6 Simulated normal-mode helix axial ratio bandwidth shown in the broadside direction ($\theta = 90^\circ, \phi$), which is shown to be less than 2.5 dB across the Iridium band of 1616 – 1626.5 MHz.

Table 3.1 Simulated normal-mode helix antenna specifications.

Specifications	Value
Center Frequency	1620 MHz
-10 dB Bandwidth	6.5 MHz (1618 – 1624.5 MHz)
Maximum Gain	+2 dB
HPBW	93°
Axial Ratio < 4 dB	Elevation angle < 45°
Polarization	RHCP
Impedance	50 Ω

An illustration of the balun used for feeding the normal-mode helix is shown in Figure 3.7.

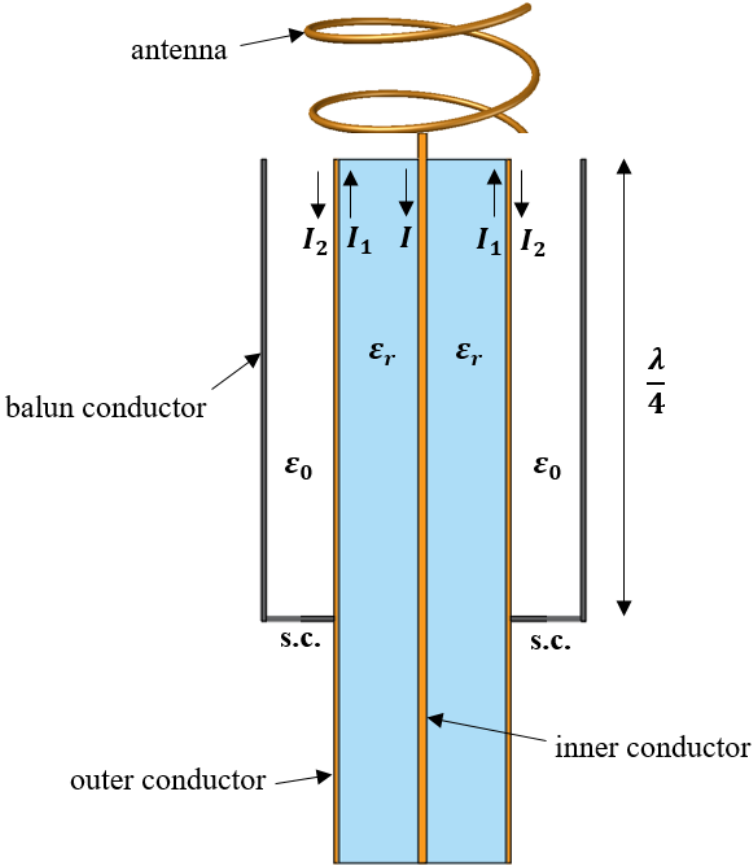
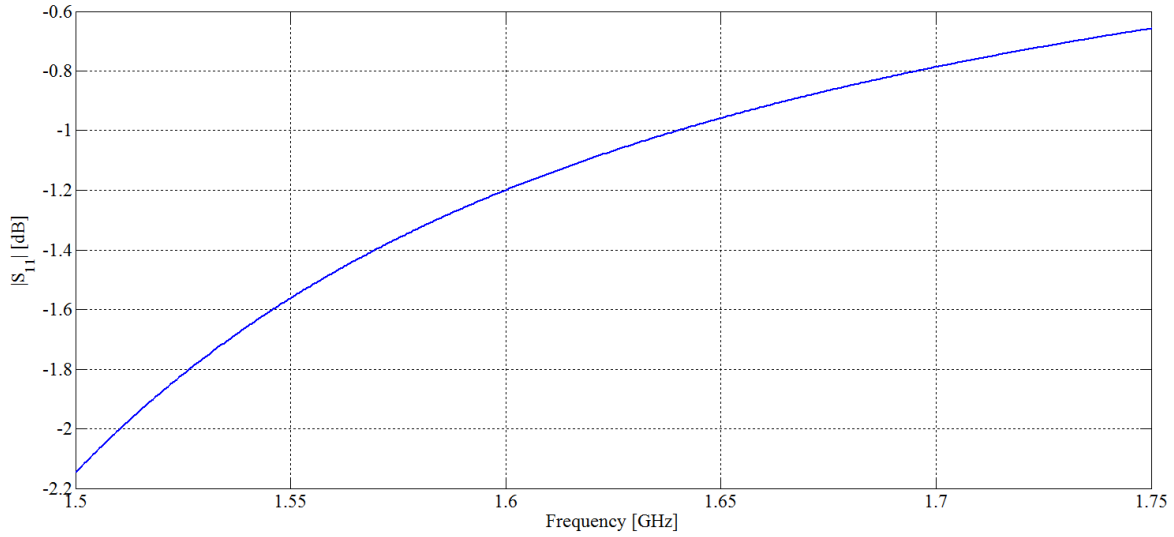
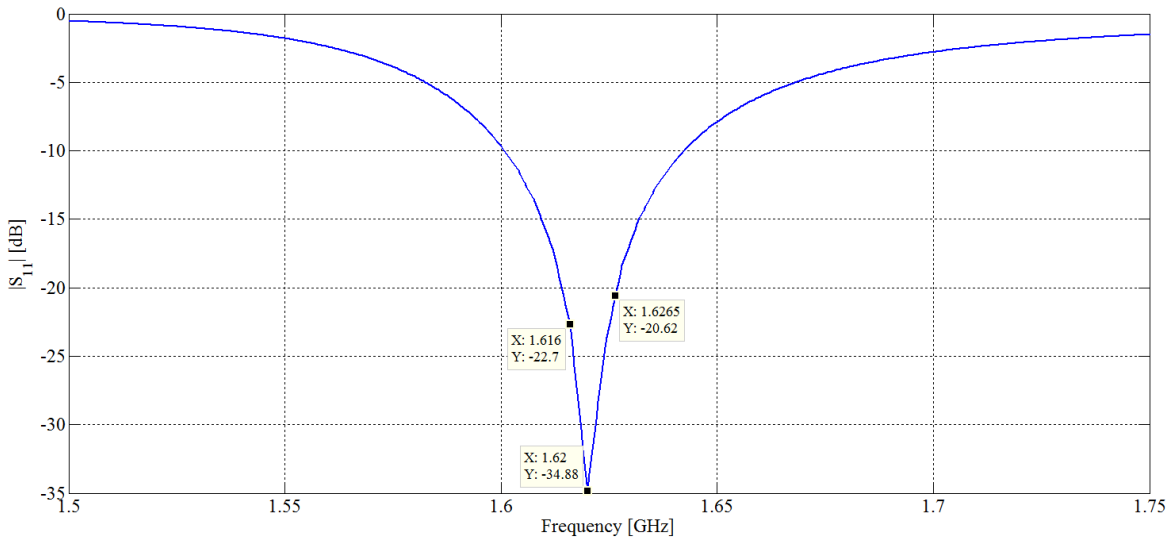


Figure 3.7 Cross sectional slice of the length of a quarter wave sleeve balun.

Once the length of the coaxial feed becomes comparable to wavelength, the current flowing on the inner surface of the outer conductor, I_1 , will spill over and flow onto the outer surface of the outer conductor, I_2 , due to the open-end of the coax. This will cause the feed to become unbalanced ($I_1 \neq I$). Therefore, a balun design was required before fabricating normal-mode helix. From transmission line theory, we know that a shorted piece of quarter wavelength line will look like a high impedance at the other end. The balun presents a high impedance at the outer surface of the outer conductor so that $I_2 \approx 0$ at the open-end of the coax. This ensures that the current flowing in the outer conductor remains on the inner surface, which keeps the feed balanced ($I_1 = I$). The balun was simulated in HFSS. Figure 3.8(a) shows the reflection coefficient of a 5 cm long coax feed without a balun, where the antenna is completely detuned and unusable. Figure 3.8(b) shows the improvement in matching when the balun is present.



(a) No balun



(b) With the balun

Figure 3.8 Reflection coefficient simulation of the normal-mode helix with a 5 cm long coax feed.

3.2.3. Fabrication, Reflection Coefficient, and Radiation Pattern Measurements

A semi-rigid coaxial cable was chosen as the feed for the helix due to its availability. Two different sizes of 50 Ω semi-rigid coax was available. The thinner of the two cables was chosen to minimize the amount of space the feed would take up. The inner conductor diameter was 0.49 mm,

the outer dielectric diameter was 1.65 mm, and the outer conductor diameter was 2.19 mm. The inner and outer conductors were made of copper and the dielectric was Teflon with a permittivity of 2.1. The normal-mode helix was constructed using 0.8 mm diameter shellac-coated copper wire. A solid plexiglass tube with a diameter of 1.4 cm was manufactured as a mold for winding the helix. The wire was hand wound around the plexiglass mold. The spacing between turns of the helix was then measured with digital calipers and adjusted until the designed helix was obtained.

A quarter wavelength balun was constructed out of an aluminum tube due its availability. The air gap between the outer conductor of the coax and inner surface of the balun was 1.925 mm since that was the smallest inner diameter of aluminum tubing available. The aluminum tubing was thinned out on a lathe to minimize the size and weight of the balun. The length of the balun was chosen to be 4.625 cm, which is $\frac{\lambda}{4}$ at the Iridium frequency band. The balun was installed on the semi-rigid coaxial cable using a nylon spacer at the open-end. Since aluminum is very difficult to solder, a metal washer was silver epoxied onto the short circuit end of the balun and cured in an oven at 170 °F for 1 hour. The washer also served as a spacer so the end of the balun could then be easily soldered onto the semi-rigid cable to create the short circuit. The helix was then soldered onto the semi-rigid feed cable with the balun as shown in Figure 3.9.

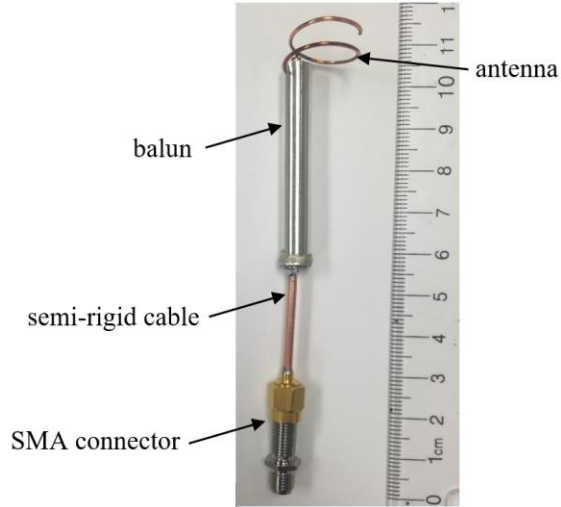
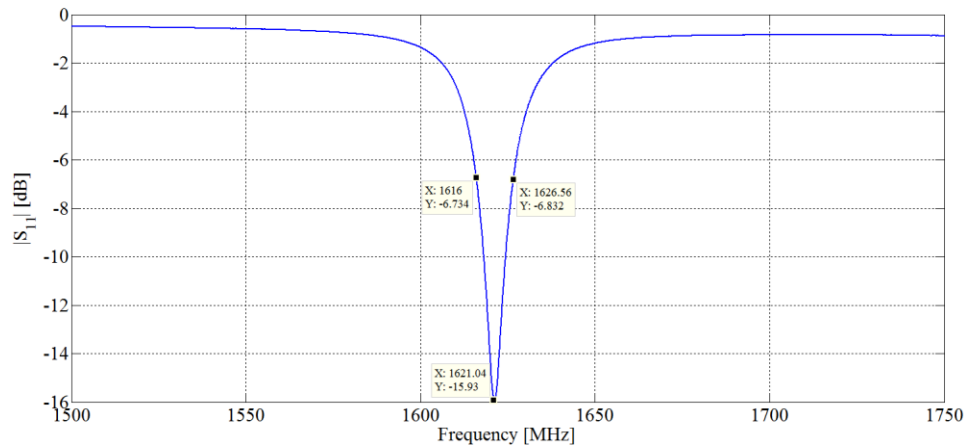


Figure 3.9 *Fabricated normal-mode helix with the balun installed on the semi-rigid coaxial feed cable.*

The reflection coefficient was measured to tune and match the helix to the Iridium frequency band. The helix was tuned to the resonant frequency of 1.621 GHz with a reflection coefficient of -15.93 dB by cutting each end of the helix a little bit at a time. The reflection coefficient is shown in Figure 3.10.



(a) Setup



(b) Reflection coefficient

Figure 3.10 *Normal-mode helix reflection coefficient measurement.*

The normal-mode helix radiation pattern was measured by placing an absorber around the feed cable to minimize the amount of induced currents on the surface of the feed. The induced surface currents would compromise the axial ratio performance by causing more radiation in the $\hat{\theta}$ -direction (radiation due to the infinitesimal electric dipoles), which would make $|\vec{E}_\theta| \neq |\vec{E}_\phi|$. The maximum measured gain occurred at 1627 MHz, which was 6 MHz higher than the resonant frequency measured on the VNA (see Section 2.2 for explanation).

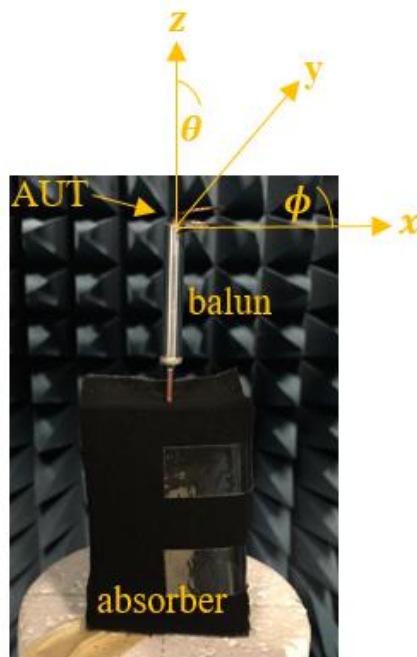
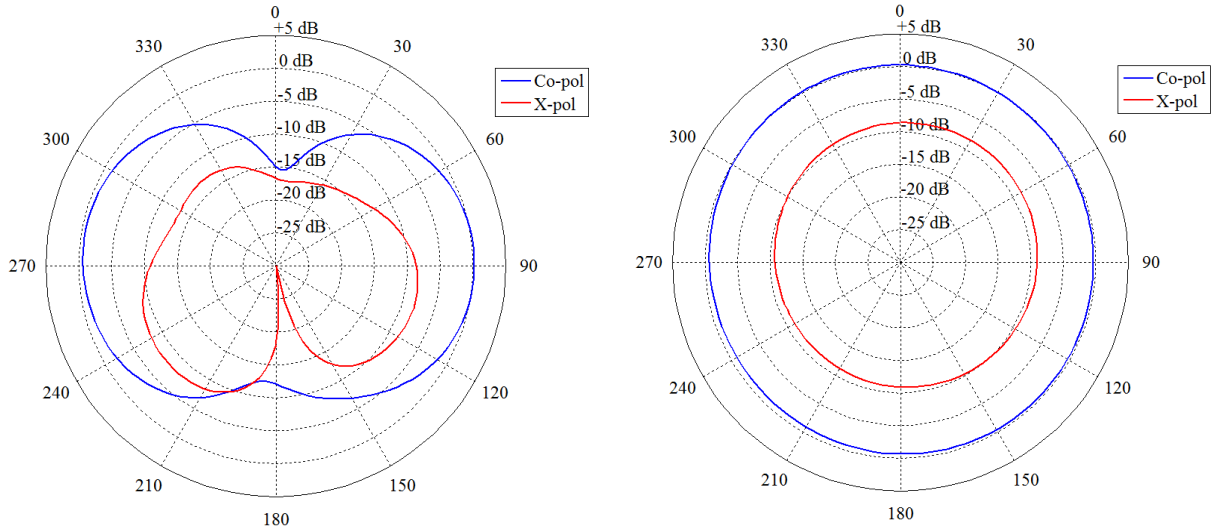


Figure 3.11 Normal-mode helix radiation pattern measurement setup with an absorber wrapped around the feed cable for electromagnetic shielding.

Figure 3.12(a) shows the measured gain in the elevation cut $\phi = 0^\circ$. Figure 3.12(b) shows the measured gain in the broadside direction, $\theta = 90^\circ$ cut. The maximum gain occurred broadside to the normal-mode helix and was approximately 0 dB.



(a) $\phi = 0^\circ$ cut with $0^\circ < \theta < 360^\circ$

(b) $\theta = 90^\circ$ cut with $0^\circ < \phi < 360^\circ$

Figure 3.12 Normal-mode helix gain measurement. The co-polarization is with respect to a RHCP receiver and the cross-polarization is with respect to a LHCP receiver. See Figure 2.6 for comparison with the measured CSA Stubby pattern and Figure 3.5 for comparison with the simulated normal-mode helix.

The axial ratio across the Iridium frequency band of 1616 – 1626.5 MHz is shown in Figure 3.13 and was less than 5.5 dB. This is high when compared to the less than 4 dB guideline for Iridium communications. The reason the axial ratio measurement did not match the simulation in Figure 3.6 was due to currents being induced on the outer surface of the balun. Since the outer surface of the balun then acted like a vertical dipole, this degraded the axial ratio due to the increased radiation in the $\hat{\theta}$ -direction. Unfortunately, the absorber could not be placed directly over the balun without significantly reducing the gain since it acted as a lossy material. A major disadvantage to using a normal-mode helix is an easily de-tunable axial ratio due to the presence of any external wavelength comparable conducting objects. Based on these findings, the normal-mode helix would be an unstable choice for use with a handheld device requiring circular polarization. A summary of the fabricated normal-mode helix specifications is shown in Table 3.2.

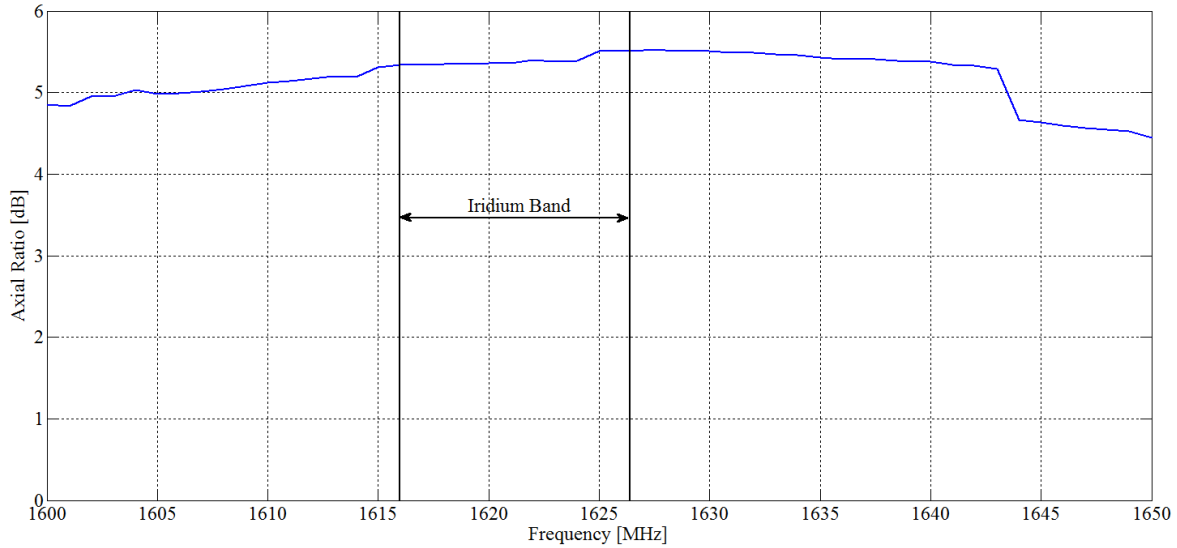


Figure 3.13 Normal-mode helix measured axial ratio bandwidth in the broadside direction ($\theta = 90^\circ, \phi$), which is shown to be less than 5.5 dB across the Iridium band of 1616 – 1626.5 MHz.

Table 3.2 Measured normal-mode helix antenna specifications. See Table 3.1 for comparison to the simulated normal-mode helix.

Specifications	Value
Center Frequency	1621 MHz
–10 dB Bandwidth	6.5 MHz (1618 – 1624.5 MHz)
Maximum Gain	0 dB \pm 2 dB
HPBW	82°
Axial Ratio < 4 dB	N/A
Polarization	RHCP
Impedance	50 Ω

3.2.4. Comparison with the Commercial CSA Stubby Antenna

The fabricated normal-mode helix and the CSA Stubby both had RHCP with omnidirectional patterns. The maximum gain occurred in the broadside direction with minimum radiation along the axes for both antennas. The CSA Stubby had a maximum gain of +1 dB and the normal-mode helix had a maximum gain of 0 dB. The CSA Stubby and the normal-mode helix had an AR <

1.5 dB and AR < 5.5 dB respectively across the Iridium bandwidth. The main reason for the CSA Stubby's superior axial ratio was due to its electrically small fed network. All the external circuitry in the CSA Stubby pattern measurement could be covered with absorbers without compromising the gain of the antenna. In the case of the normal-mode helix, a quarter wave balun was required to create a balanced feed network that would allow the antenna to function properly. Because of the proximity of the balun to the antenna, we were unable to cover the balun with absorbers without sacrificing gain. Consequently, the axial ratio was degraded because of induced currents radiating on the outer surface of the balun.

3.3. Adaptive PEC/PMC Beam Shaping Technique

The concept of shaping a linearly polarized antenna pattern using a parasitic PEC element is similar to a Yagi-Uda antenna reflector. A $\frac{\lambda}{2}$ length piece of conducting wire can be used as the reflector for a linearly polarized source that is parallel to it when there is a separation of $\frac{\lambda}{4}$ [32]. The $\frac{\lambda}{4}$ distance the wave must travel between the source and reflector creates a 90° phase shift. When the wave hits the reflector, it will experience another 180° phase shift. Both phase shifts, coupled with another 90° phase shift on the return path, create a full 360° phase shift when the reflected wave arrives back at the source. Therefore, the reflected wave will add in phase with the source and radiate with +3 dB more gain away from the reflector. A more challenging solution is required for parasitically reflecting circular polarization in a compact manner. In Section 3.2, it was noted that a normal-mode helix could be modelled as the superposition of elemental electric

and magnetic dipoles. From image theory [29], shown in Figure 3.14, we know that an electric source parallel to a PEC will have an image with a 180° phase difference.

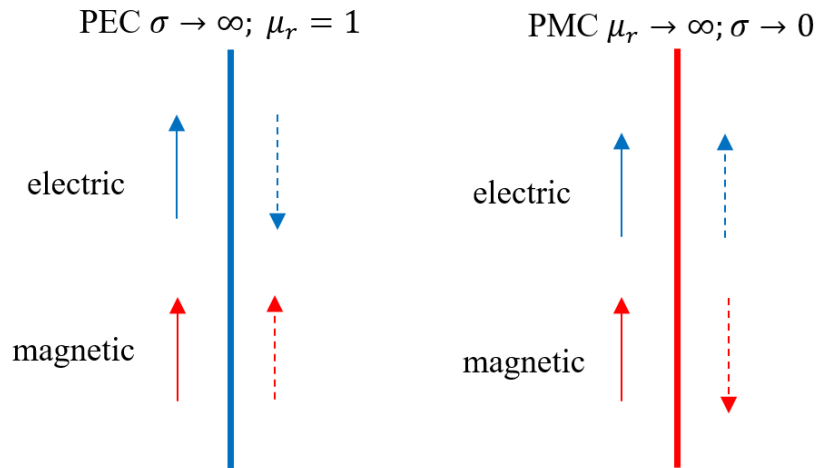


Figure 3.14 *An illustration of image theory with the sources shown on the left side of the surface and the images shown on the right side.*

By the principle of duality an artificial equivalent magnetic source parallel to a PMC will also have an image with 180° phase difference. If we move a distance of $\frac{\lambda}{4}$ away from these surfaces, the waves will experience another 180° phase shift from travelling from the source to the surface and back. This will provide an image that looks like it is in phase with the source.

Given the normal-mode helix can be modelled as independent elemental electric and magnetic sources, it is theoretically possible to reflect a circularly polarized wave since both components can be reflected when the helix is a quarter wavelength away from a parallel PEC and PMC surface. The challenge is that the PMC surface does not exist practically and most high permeability materials do not behave well above 1 GHz [33]. Ferrite was considered as option to use as a good magnetic conductor, however, it is not commonly available in the GHz frequency range.

3.4. Adaptive PEC/PMC Beam Shaping Simulation

To prove the adaptive PEC/PMC beam shaping technique discussed in the previous section, a simulation in HFSS was performed using the normal-mode helix designed in Section 3.2 and is shown in Figure 3.15. The source antenna was chosen to be a normal-mode helix due to its RHCP and similar radiation pattern to industry standard antennas for Iridium communications as discussed in Chapter 2. The normal-mode helix was centered at the origin and the PEC/PMC reflector was placed at a distance of $x = \frac{\lambda}{4}$ in the yz -plane.

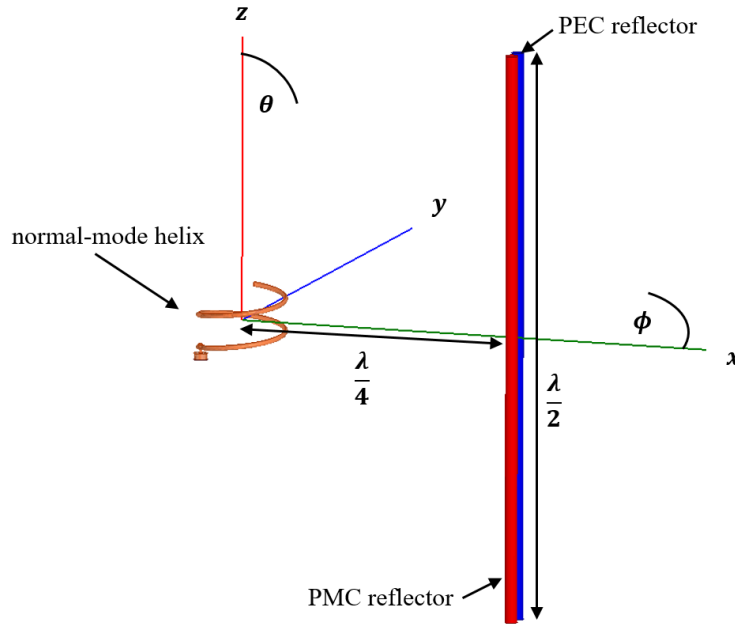


Figure 3.15 HFSS model of the PEC/PMC reflector device (located in the yz -plane) with a normal-mode helix source at the origin.

A $\frac{\lambda}{2}$ length copper wire was used for the PEC reflector and a $\frac{\lambda}{2}$ length wire was created that had a relative permeability $\mu_r = 10^{15}$ and conductivity $\sigma = 10^{-15}$ to simulate the PMC reflector. The diameter of the wires was chosen to be 2 mm to satisfy the condition that a dipole's diameter must be much less than the wavelength of operation ($\lambda = 18.5$ cm) [29]. The basis of the reflectors is

that they would act like parasitic dipoles. The adjacent spacing between the PEC and PMC reflectors, located in the yz -plane, was arbitrarily chosen to be 1 mm to simulate a hybrid-like surface that would ensure both reflectors would provide an equal reflection in the same direction. Increasing the number of reflectors was not investigated further due to the success of the single PEC/PMC reflector, which minimized the space needed to fit a handheld device. The adjacent spacing between the PEC and PMC reflectors was not considered further since the 1 mm spacing was sufficient for providing proper beam shaping.

Another identical simulation was done using $\frac{\lambda}{4}$ length reflectors to investigate making the reflector system look semi-transparent to the source when turned off. Since the wires are no longer resonant length, they should have a negligible impact on the radiation pattern of the source antenna. Figure 3.16(a) shows the simulated gain of the source antenna with the PEC/PMC reflecting system turned on and Figure 3.16(b) shows the gain with the system turned off. The gain was +5 dB in the direction away from the reflectors and -5 dB towards the reflectors with the system turned on. The slight asymmetries in the pattern are mostly due to the non-centered feed of the normal-mode helix. When the system was turned off, the pattern was nearly symmetric with a maximum gain of +2 dB. Therefore, the gain is decreased in the reflector direction by 7 dB with the system turned on. Figure 3.17 shows the axial ratio bandwidth in the direction of maximum radiation ($\theta = 90^\circ, \phi = 180^\circ$) when the adaptive beam shaping system is turned on. The axial ratio across the Iridium frequency band was less than 1.5 dB, which meets the 4 dB guideline for Iridium communications.

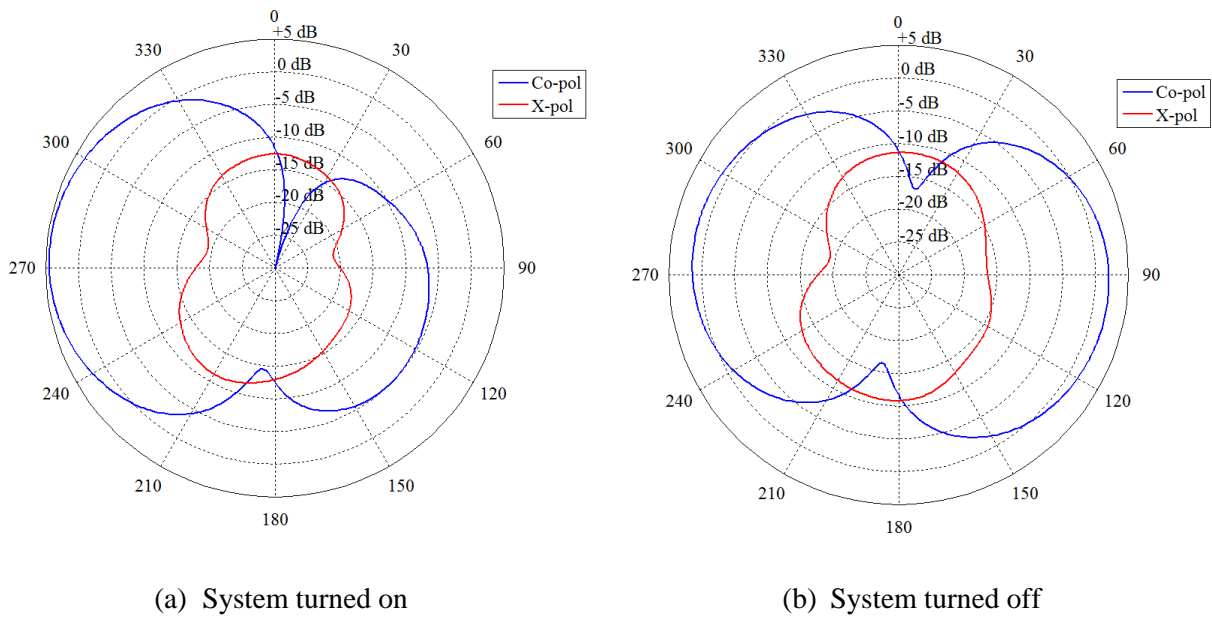


Figure 3.16 Gain simulation of the normal-mode helix with the adaptive PEC/PMC beam shaping device in the $\phi = 0^\circ$ cut with $0^\circ < \theta < 360^\circ$. The co-polarization is with respect to a RHCP and the cross-polarization is with respect to a LHCP receiver. See Figure 3.5(a) for a comparison of the simulated gain with no PEC/PMC reflector present.

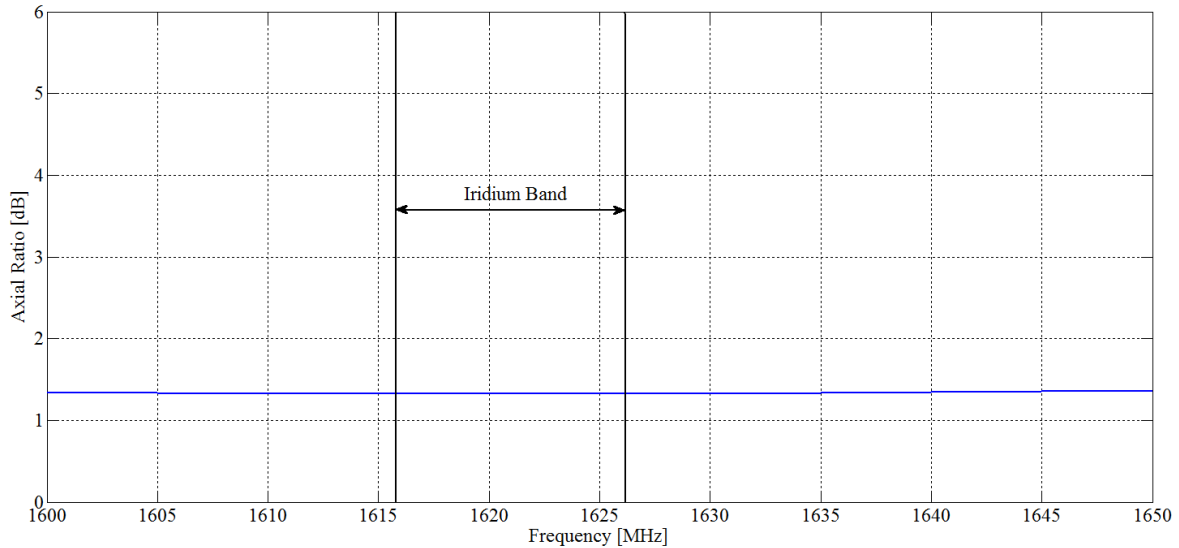


Figure 3.17 Simulated axial ratio bandwidth of the normal-mode helix with the adaptive PEC/PMC beam shaping device turned on. The axial ratio was less than 1.5 dB across the Iridium band of 1616 – 1626.5 MHz in the broadside direction away from the reflector ($\theta = 90^\circ, \phi = 180^\circ$).

A practical implementation for turning the reflector system on and off would be to open circuit the center of the $\frac{\lambda}{2}$ wires to make them a non-resonant length, which would be controlled by the impedance monitoring system. A possible implementation of this is shown in Figure 3.18 using a diode based switching system. A concept diagram showing a theoretical implementation of the adaptive PEC/PMC beam shaping device is shown in Figure 3.19.

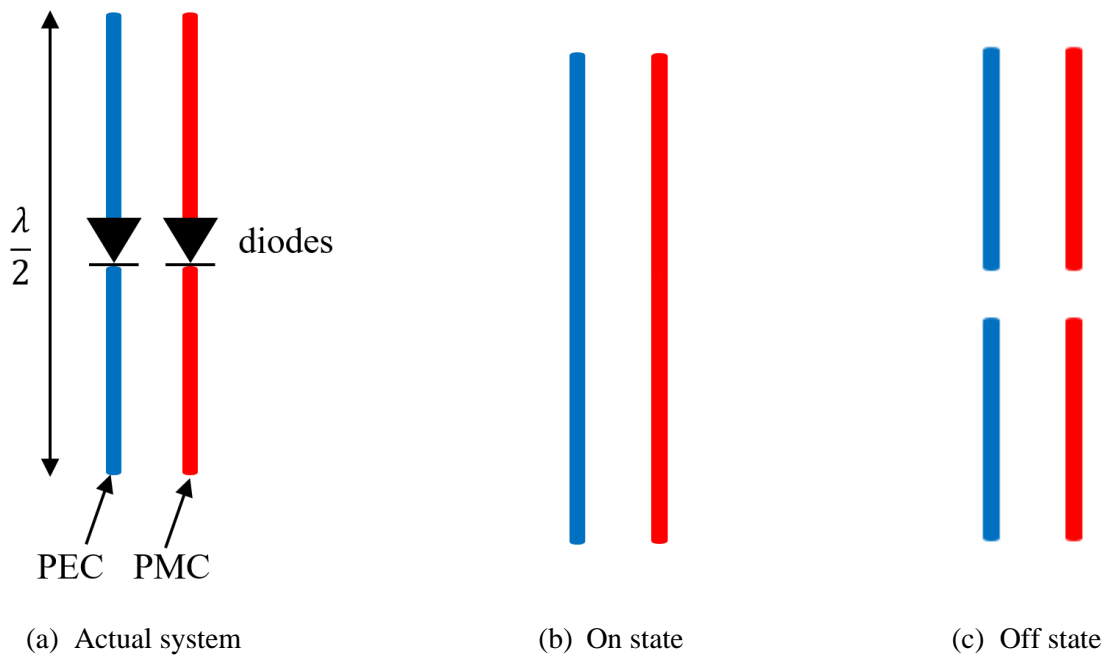
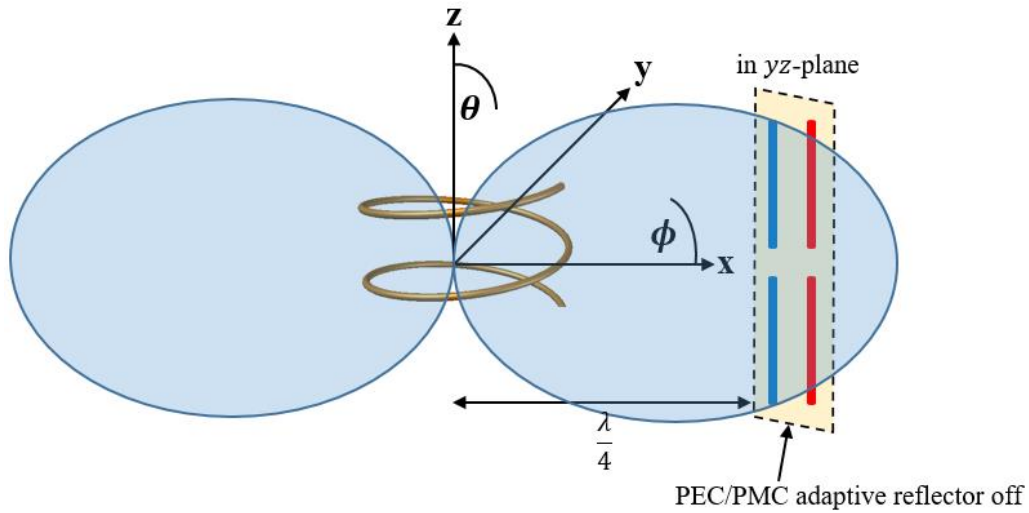
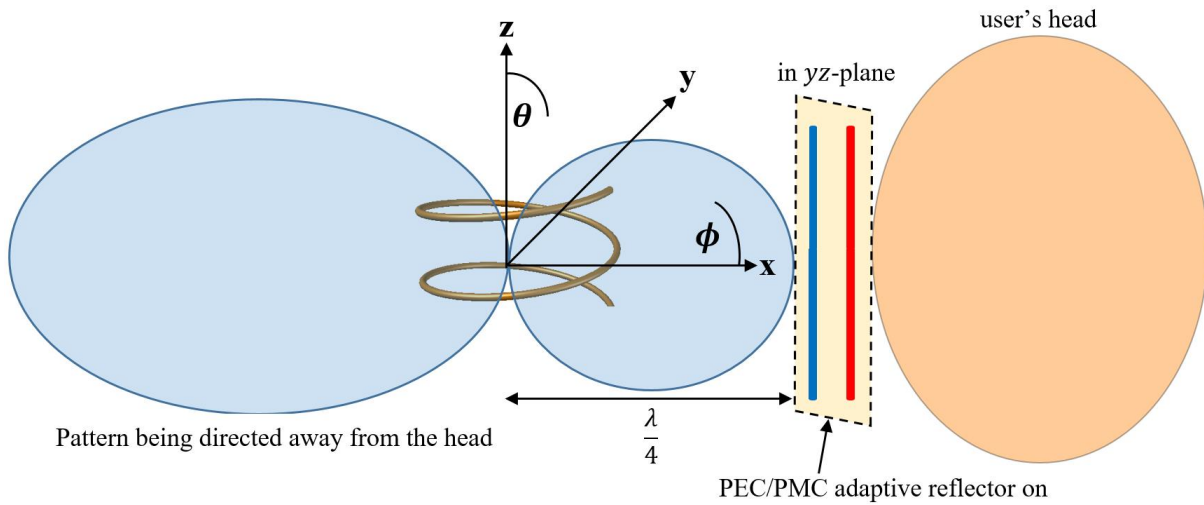


Figure 3.18 *Illustration of the on/off controls of the adaptive PEC/PMC beam shaping device.*



(a) Reflector system turned off when a head is not nearby



(b) Reflector system turned on when a head is nearby

Figure 3.19 Illustration of the how the adaptive PEC/PMC beam shaping device would operate with a human user.

Since the gain is decreased by 7 dB with the adaptive system turned on in Figure 3.16(b), this corresponds to about an 80% drop in power radiated towards the human user's head based on the far-field results. The adaptive PEC/PMC beam shaping device would reduce peak SAR levels to $1.67 \frac{\text{W}}{\text{kg}}$ when turned on based on a SAR level of $8.36 \frac{\text{W}}{\text{kg}}$ for a 2 W transceiver output power for

the industry standard quadrifilar helical antenna discussed in [10]. This is within reason of the $1.6 \frac{W}{kg}$ limitation using the crude approximation discussed in Section 1.1, assuming that the quadrifilar helical antenna in [10] has a similar gain to the normal-mode helix.

A high permittivity material could be used to minimize the physical space that the electric spacing of $\frac{\lambda}{4}$ between the antenna and the reflector would require. The main obstacle of physically implementing the adaptive PEC/PMC beam shaping device would be fabricating a material small enough that behaved like a PMC in the GHz frequency range. The next section will explore AMCs that have potential for providing the PMC-like behavior.

3.5. AMC Impedance Surface

A PMC surface does not exist practically, however, EBG/AMC surfaces can mimic the characteristics of a PMC across a defined bandwidth [14]. An ideal PMC surface will have a reflection coefficient of +1, whereas a PEC will have a reflection coefficient of -1 . The intrinsic impedance of an ideal PMC surface assuming $\mu_r \rightarrow \infty$, $\sigma \rightarrow 0$, and $\epsilon_r = \text{finite}$ is shown below:

$$\eta_{\text{pmc}} = \sqrt{\frac{j\omega\mu_0\mu_r}{\sigma + j\omega\epsilon_0\epsilon_r}} \Rightarrow \eta_{\text{pmc}} \rightarrow \infty \quad (3.2)$$

The reflection experienced by a wave hitting a PMC/high impedance surface coming from free space ($\eta_0 = 377 \Omega$) is then given by:

$$\Gamma_{\text{pmc}} = \frac{\eta_{\text{pmc}} - \eta_0}{\eta_{\text{pmc}} + \eta_0} = +1 \quad (3.3)$$

Texturing a conducting surface with a periodic structure makes it possible to create a high impedance surface for a fixed frequency band. The frequency range where the reflection phase is within $\pm 90^\circ$ is defined as the PMC bandwidth due to the surface displaying PMC-like behavior [13].

An AMC can be modelled as a parallel LC circuit provided the periodicity of the repeating structure is much less than the wavelength. The repeating structure is known as the unit cell. The capacitance, C , represents the interaction between two adjacent square patches and the inductance, L , represents a segment of shorted transmission line with a length equal to the dielectric thickness h [13]. In Sievenpiper's paper, each unit cell had dimensions of lattice constant \times lattice constant with a copper square patch with side lengths lattice constant $- s$ centered over top of a grounded dielectric [14]. Starting with Sievenpiper's original design in HFSS it was possible to obtain 0° of reflection phase near the Iridium center frequency of 1.621 GHz by scaling the unit cell appropriately. The unit cell is shown in Figure 3.20(a) and the dimensions were chosen as follows:

- $\epsilon_r = 2.2$
- lattice constant = 2.088 cm
- $h = 1.392$ cm
- $s = 1.305$ mm
- $w = 3.132$ mm

The dielectric chosen was Rogers RT/duroid 5880 with a height of h and dielectric constant of ϵ_r . A cylindrical via with diameter w was centered across the unit cell to connect the top patch to the ground, providing the inductance L .

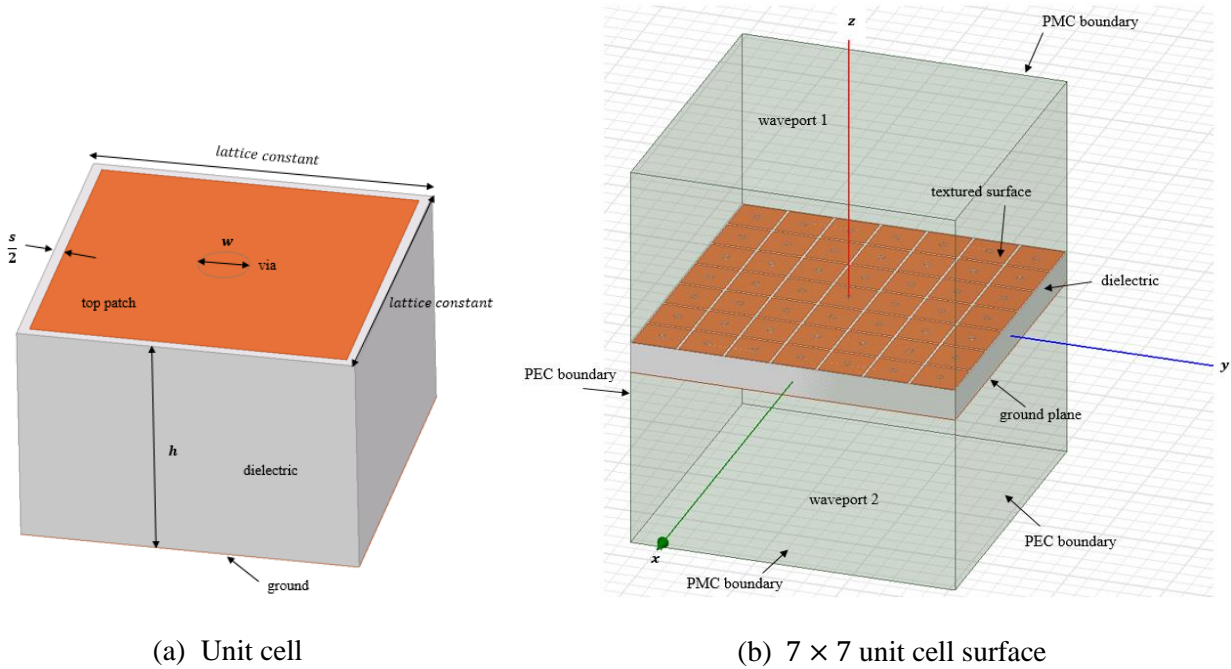
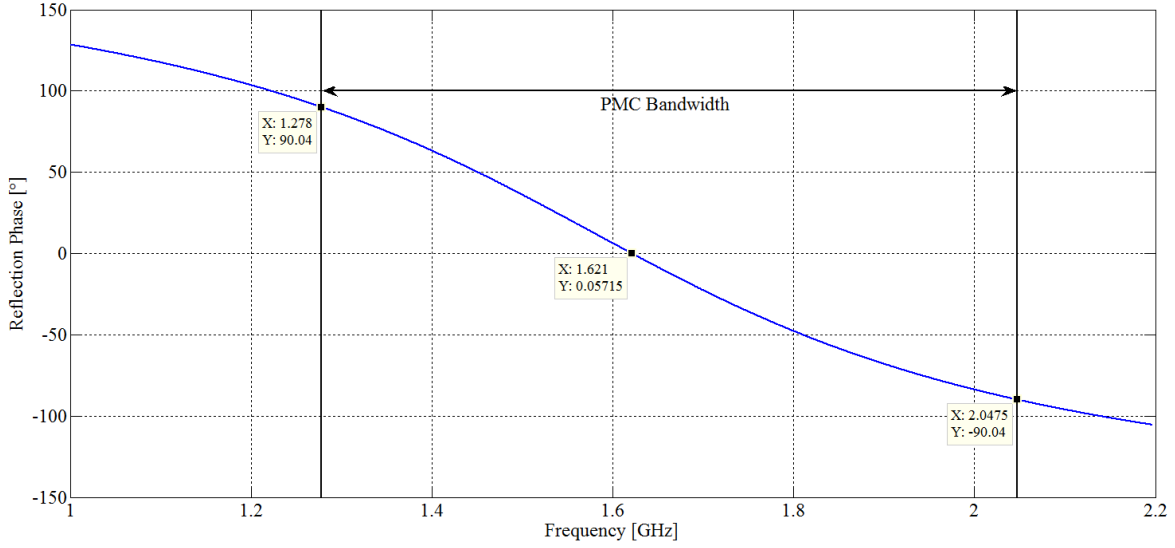
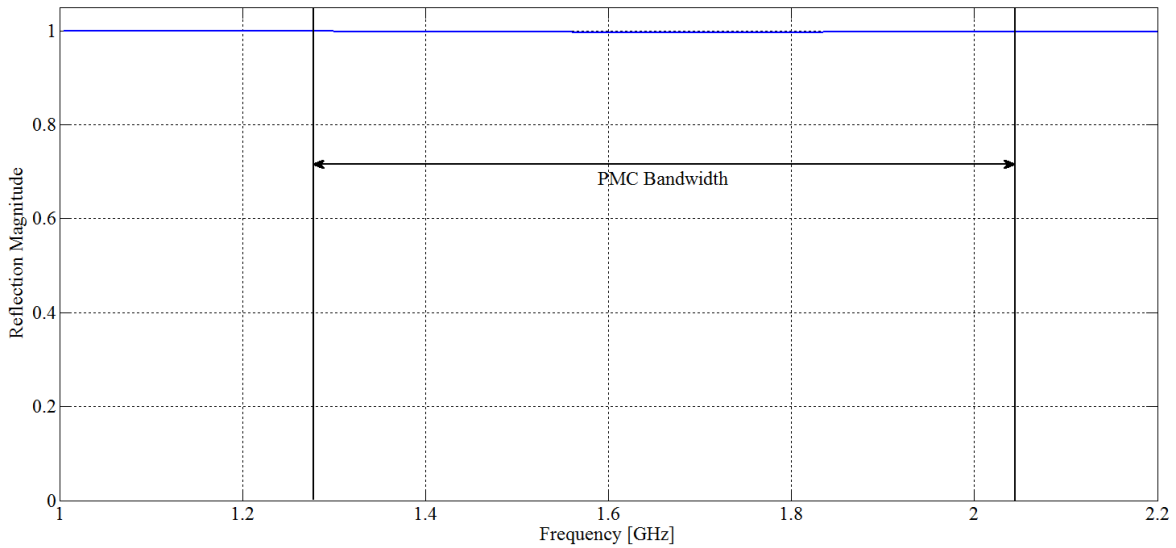


Figure 3.20 AMC impedance surface model designed in HFSS based off [14].

An AMC impedance surface was constructed in HFSS using 7×7 unit cells and is shown in Figure 3.20(b). The structure was excited with wave ports on the top and bottom surface of the outer boundary with a \hat{y} -polarized electric field. The $+\hat{y}$ and $-\hat{y}$ boundary walls were assigned to be PECs and the $+\hat{x}$ and $-\hat{x}$ boundaries were assigned to be PMCs to create a TEM waveguide structure. An incident wave was excited at waveport 1, which allowed the reflection phase of the wave at the surface of the AMC to be measured as shown in Figure 3.21(a). The reflection magnitude is also shown to be $+1$ across the PMC bandwidth in Figure 3.21(b). The PMC bandwidth of the AMC surface was 769.5 MHz between 1.278 GHz and 2.0475 GHz.



(a) Phase



(b) Magnitude

Figure 3.21 Simulation of the reflection coefficient for the AMC impedance surface.

A single column of the AMC impedance surface was also simulated using a 1×7 unit cell structure to mimic the PMC wire that was discussed in Section 3.4. The single column structure performed poorly in HFSS since the operation of the AMC design in [14] relies on the capacitance between neighboring unit cells.

Therefore, to successfully miniaturize the AMC structure to fit inside a handheld device it would need to be explored in much further detail, which is outside the scope of this thesis. A method of making the AMC surface look semi-transparent when the reflector system is turned off would also need to be determined.

3.6. Conclusion

A PEC/PMC based structure was explored in this chapter for adaptively shaping a circularly polarized omnidirectional pattern. A normal-mode helix was designed to mimic the far-field radiation properties of Multiband Antenna's CSA Stubby. This ensured that the adaptive PEC/PMC beam shaping device was tested with the current state of the art antennas for Iridium communications. The simplicity of the normal-mode helix allowed for an easy, but effective model for simulating the adaptive beam shaping device in HFSS. The normal-mode helix was also fabricated and measured to see how it compared to the CSA Stubby measurements. Because of the small electrical size of the normal-mode helix, but large electrical size of the feed network, the antenna was only able to provide an axial ratio of 5.5 dB across the Iridium band. Industry standard antennas should generally have an AR < 4 dB for applications using Iridium satellites.

The theoretical model of the adaptive PEC/PMC beam shaping device was successful in shaping the normal-mode helix pattern away from the reflector in simulation. With the reflector system turned off, the helix had a maximum gain of +2 dB in the broadside direction. When the reflector was turned on, the gain was directed away from the reflector by +5 dB with only -5 dB of gain directed towards the reflector. The decreased gain towards the reflector would ensure less

radiation was absorbed by a nearby human body while optimizing the signal strength away from the body. Using the rough approximation discussed in Section 1.1, it was shown that the SAR levels could be reduced from $8.36 \frac{\text{W}}{\text{kg}}$ to $1.67 \frac{\text{W}}{\text{kg}}$ with the adaptive beam shaping system turned on based on the far-field results.

The main obstacle in fabricating the adaptive PEC/PMC beam shaping device is finding a compact enough material that behaves as a PMC in the GHz frequency range. In Section 3.5, we explored periodic resonant structures called AMCs, which have a bandgap where they behave like a PMC. An AMC impedance surface model was successfully designed and simulated. The challenge with the AMC was reducing the size small enough to fit into a handheld device. Due to the unlikelihood of being able to further miniaturize the AMC, a back-to-back patch antenna design was explored in the next chapter as an alternative to the adaptive PEC/PMC beam shaping device.

Chapter 4

Back-to-Back Patch Antenna

4.1. Overview

Patch antennas are commonly used for satellite communications since they are low-cost, low-profile, compact, and can be easily modified to provide circular polarization [5, 34]. The disadvantage with using a single patch antenna is that there is only one hemisphere of coverage. Consequently, the signal of the handheld device would be compromised if it were oriented in such a way that the plane of the patch was facing into the ground. This chapter explores a back-to-back patch antenna design that can provide both hemispheres with coverage. The design was based on two identical RHCP patch antennas. One patch would face towards the front of the phone and the other towards the back of the phone, allowing for a compact design. Both patches would have their own separate feed. The separate feeds would allow for simple on/off control of one of the patches to reduce radiation exposure to a human user when used in conjunction with the impedance monitoring system proposed in Chapter 5. The back-to-back patch antenna design was simulated, fabricated, and tested. In Section 4.5, a homogenous phantom was placed near the back-to-back patch antenna to emulate a user's head. Radiation pattern measurements were taken with the phantom to investigate how a nearby head would influence the pattern of the antenna. In Section 4.6, a SAR simulation was done in HFSS using a homogenous ellipsoid model of the human head. This simulation was done to determine an approximate distance at which radiation from the back-to-back patch antenna would be within an acceptable level for human exposure. Beam shaping using feed phasing was also investigated in Section 4.7.

4.2. Background Theory

After exploring the normal-mode helix in Chapter 3, a patch antenna was decided on due to its more ubiquitous use in satellite communications and its ability to be easily modified to provide RHCP. To better understand how a circularly polarized patch antenna works, we will first start by briefly analyzing a standard patch antenna as shown in Figure 4.1. The length of the patch should be close to $\frac{\lambda}{2}$ in the direction of the feed. This creates a voltage distribution as shown on the red curve in Figure 4.1. Because the edges of the patch look like an open circuit, the voltage magnitude will be maximum there. There will be fringing fields between the edge of the patch and the ground plane due to the patch's finite size [29]. Since the patch has a length $L = \frac{\lambda}{2}$, the voltage at one edge will be maximum while the other edge will be minimum. This creates in phase electric fields in the \hat{y} -direction off both edges, which allow the patch antenna to radiate. Electric fields in the \hat{z} -direction will not radiate since they are out of phase and will cancel each other out. Since the edges of the patch look like a high impedance, a feed network is required to deliver power to the antenna. A quarter wavelength transformer is one method of feeding the patch antenna as shown in Figure 4.1.

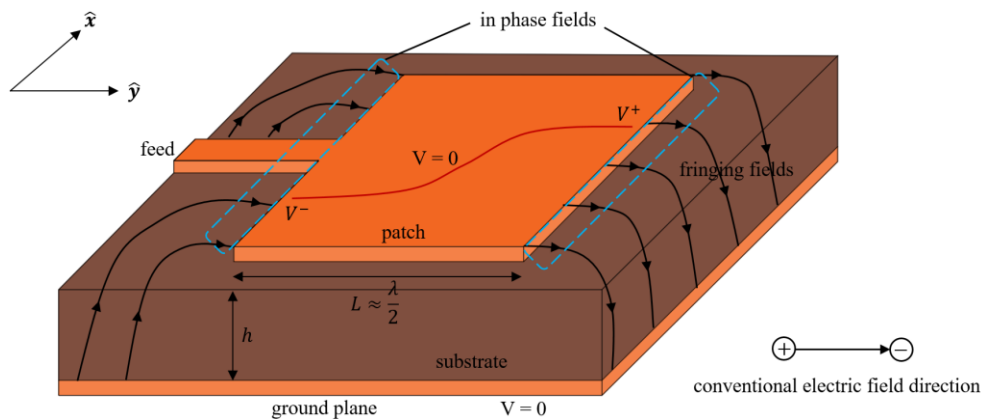


Figure 4.1 Patch antenna fringing fields.

A square patch antenna will have two dominant orthogonal modes as shown in Figure 4.2(a). Since the \hat{x} and \hat{y} dimensions of the patch are the same length, the two dominant modes, TM_{10} and TM_{01} , are known as degenerate modes because they share the same resonant frequency. Degenerate modes can be used to generate circular polarization if they are excited 90° out of phase [5]. One way to generate circular polarization using a single feed is to truncate opposite corners of the patch as shown in Figure 4.2(b).

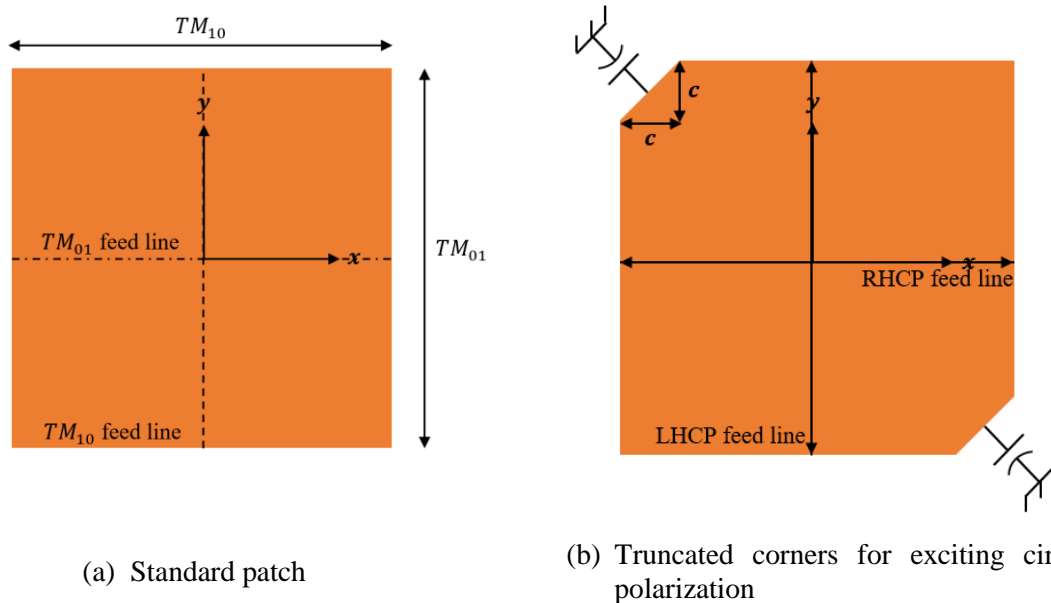


Figure 4.2 Excitation of degenerate modes on a square patch antenna.

RHCP or LHCP can be excited depending on what line the feed is located on. Truncating an appropriate amount off the corners makes the resonant frequency of the two orthogonal modes slightly different. This also causes a perturbation that creates coupling between the two edges, which allows us to use a single feed. The coupling between the corners will look capacitive, thus providing a 90° phase shift between the two modes. An illustration of the 90° phase shift between the two orthogonal modes is shown in Figure 4.3. The optimal circular polarization will occur

between mode 1 and mode 2's resonant frequencies f_1 and f_2 respectively. This frequency is labelled as f_0 in Figure 4.3, which is where the 90° phase shift occurs.

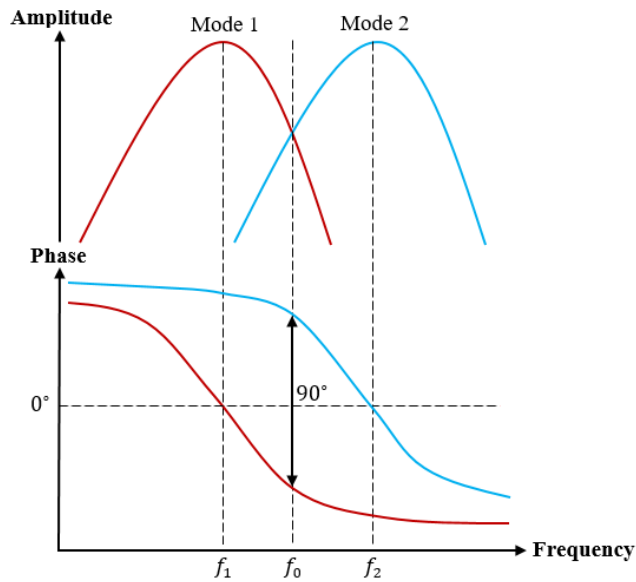


Figure 4.3 Illustration of how circular polarization is generated from truncating the corners of a square patch [5].

There are several papers discussing how much to truncate off the corners to generate circular polarization [34–36]. [34] used a truncation value of $c = 0.046L$, [35] used $c = 0.072L$, and [36] used $c = 0.107L$. Due to the variation in truncation values found in the literature, optimization will be required to determine the optimal circular polarization for a given patch design.

4.3. Design and Simulation

A square patch antenna design with truncated corners was chosen for generating the required RHCP needed for satellite communications. A method of feeding the patch was explored. In Section 4.2, it was mentioned that the impedance at the edge of the patch was too high to deliver

significant enough power to the antenna. This is because the current goes to zero there and the voltage magnitude is maximum. Therefore, a feed network is required to deliver optimal power to the antenna. Since the back-to-back patch antenna would require the two patches to be back-to-back, a traditional coaxial probe feed would be inappropriate. Several different feeding methods were explored such as proximity coupling in [37], coplanar waveguide in [38], and inset feeding in [39]. Proximity coupling was simulated in HFSS, however, it was ruled out since it nearly doubled the thickness of the back-to-back patch antenna and would require complicated multi-layer PCB technology for fabrication. Inset feeding was also explored, however, it was very difficult to excite and tune the circular polarization. The perturbation, due to the inset feed, disrupts the surface currents on the patch and makes it difficult to generate and tune the circular polarization. [39] discusses some various methods for generating circular polarization using an inset feed. One of the methods discussed in the paper involved adding a thin slit at one or more of the patch edges. The slit combined with the truncated corners helped to meander the surface currents appropriately for generating circular polarization. Adding a slit to an inset fed patch antenna was explored in HFSS, however, it was still quite difficult to excite and tune the circular polarization. Therefore, it was decided that inset fed was not the most suitable method for this design.

For initial investigation and implementation, a single quarter wave transformer feed would provide the most robust and easily tunable design since the Iridium frequency band is narrow. A low permittivity substrate was chosen for the initial antenna design with miniaturization of the antenna left for future work. A truncated corner square patch antenna was designed in HFSS using RT/duroid 5880. RT/duroid 5880 has a permittivity of $\epsilon_r' = 2.2$ and loss tangent of $\tan\delta =$

0.0009 [40]. A substrate thickness of $h = 1.57$ mm was chosen due to its availability. A coax probe was placed at one of the edges of the patch to simulate the edge impedance. This allowed us to determine the necessary characteristics of the quarter wavelength line to properly match the antenna. The impedance at the edge of the patch was tuned by varying the truncation value, c , until the two impedances of the degenerate modes were nearly the same as illustrated in Figure 4.3. This made the tuning of the circularly polarized center frequency much simpler. The edge impedance of the midpoint between the two modes was determined to $Z_{\text{edge}} = 138 \Omega$. The characteristic impedance required for the quarter wave transformer to provide a 50Ω match to the patch was then calculated using (4.1).

$$Z_{\text{in}} = \frac{Z_{0t}^2}{Z_L} \rightarrow Z_{0t} = \sqrt{50 \times 138} \rightarrow Z_{0t} = 83 \Omega \quad (4.1)$$

The TRL calculator in Ansoft Designer was used to calculate the physical parameters of the quarter wavelength line at 1621 MHz. The width and length were determined to $w_t = 1.85$ mm and $L_t = 34.66$ mm respectively after further optimization in HFSS. To ensure that the ground plane was symmetric around the entire patch, the length of the quarter wave transformer was used as the amount of substrate extending beyond each edge of the patch. The dimensions of the optimized patch antenna are shown in Figure 4.4.

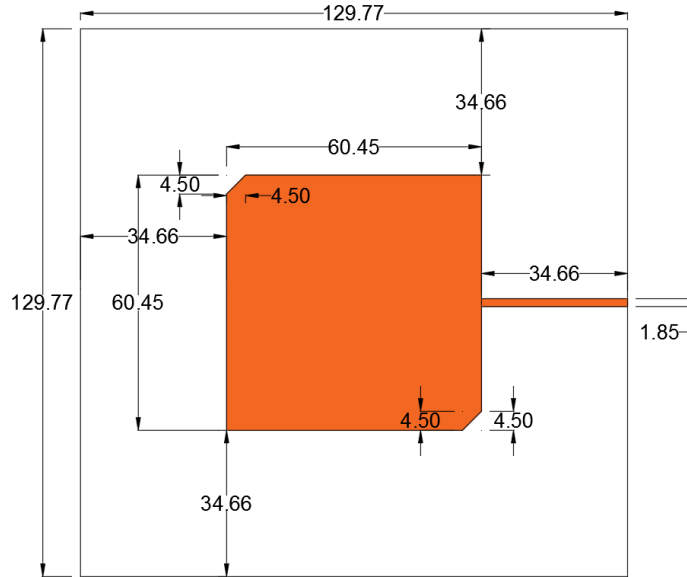


Figure 4.4 Design of one element of the back-to-back patch antenna with a quarter wave transformer feed. All units are in mm.

An identical copy of the patch antenna was placed back-to-back with first patch except with its feed along the $-\hat{x}$ -axis instead of the $+\hat{x}$ -axis as shown in Figure 4.5. This was done on purpose to minimize the coupling between the feeds.

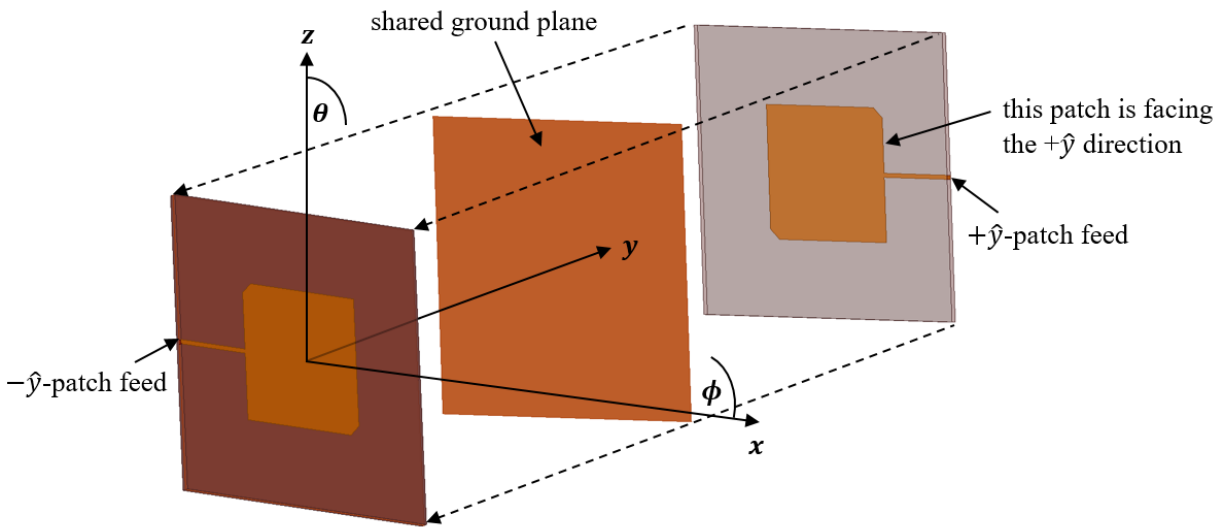


Figure 4.5 HFSS model of the back-to-back patch antenna with quarter wave transformer feeds to each element.

The reflection coefficient of the back-to-back patch antenna was simulated with both patches excited as shown in Figure 4.6.

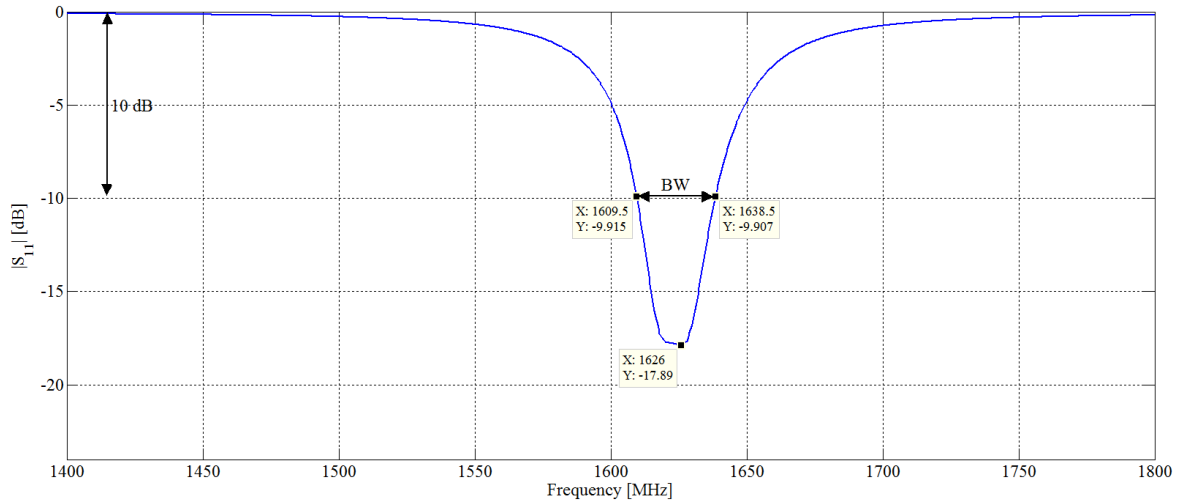
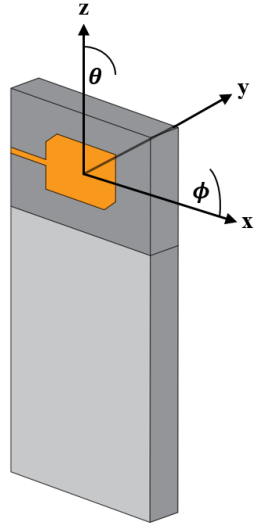


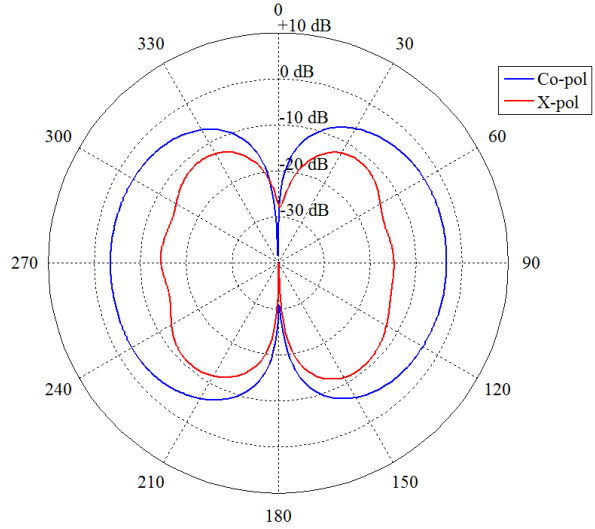
Figure 4.6 Simulated back-to-back patch antenna reflection coefficient.

We can see that the Iridium frequency band of 1616 – 1626.5 MHz is all below –10 dB. The –10 dB bandwidth of the back-to-back patch was 29 MHz, which was well above the required 10.5 MHz for an Iridium handheld device.

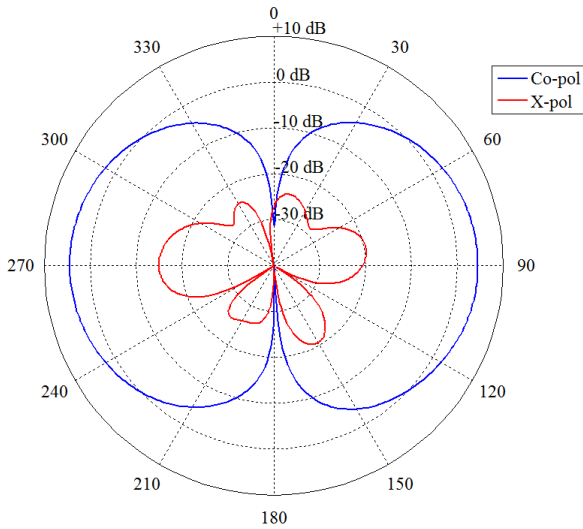
The gain when both patches were turned on was simulated and is shown in Figure 4.7. Figure 4.7(b) shows the gain in the elevation cut $\phi = 0^\circ$ with a maximum gain of –3 dB and Figure 4.7(c) shows the gain in the $\phi = 90^\circ$ cut with a maximum gain of +4.5 dB. Both cuts had nulls at $\theta = 0^\circ, 180^\circ$. Figure 4.7(d) shows a more uniform gain in the $\theta = 90^\circ$ cut, with the gain varying between –3 dB and +4.5 dB. Thus, the maximum gain of the simulated back-to-back patch antenna was +4.5 dB. Since the antenna was designed to be RHCP, the co-polarization is with respect to what a RHCP receiver would receive and the cross-polarization is with respect to a LHCP receiver.



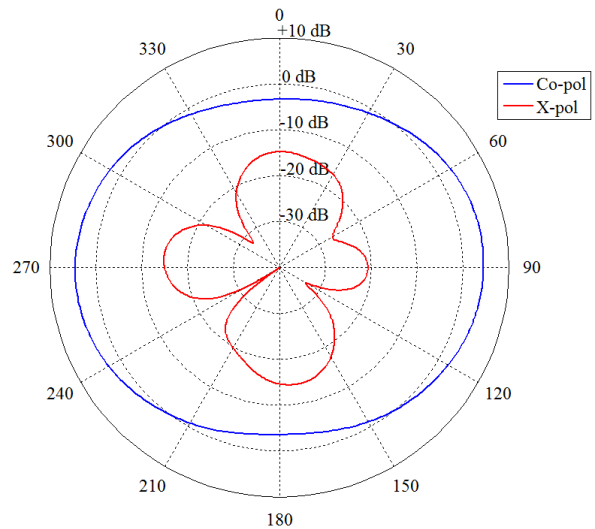
(a) Orientation of the antenna



(b) $\phi = 0^\circ$ cut with $0^\circ < \theta < 360^\circ$



(c) $\phi = 90^\circ$ cut with $0^\circ < \theta < 360^\circ$



(d) $\theta = 90^\circ$ cut with $0^\circ < \phi < 360^\circ$

Figure 4.7 Back-to-back patch antenna gain simulation with both patches on. The co-polarization is with respect to a RHCP and the cross-polarization is with respect to a LHCP receiver. Note the phone case was not present in the simulation.

Figure 4.8 shows the gain when the $-\hat{y}$ -patch was not excited and only the $+\hat{y}$ -patch was left on. Both the $\phi = 90^\circ$ and $\theta = 90^\circ$ cuts have very similar patterns, giving us the expected hemispherical pattern shape of a standard patch antenna. The maximum gain was $+7.5$ dB in the broadside direction of the active patch.

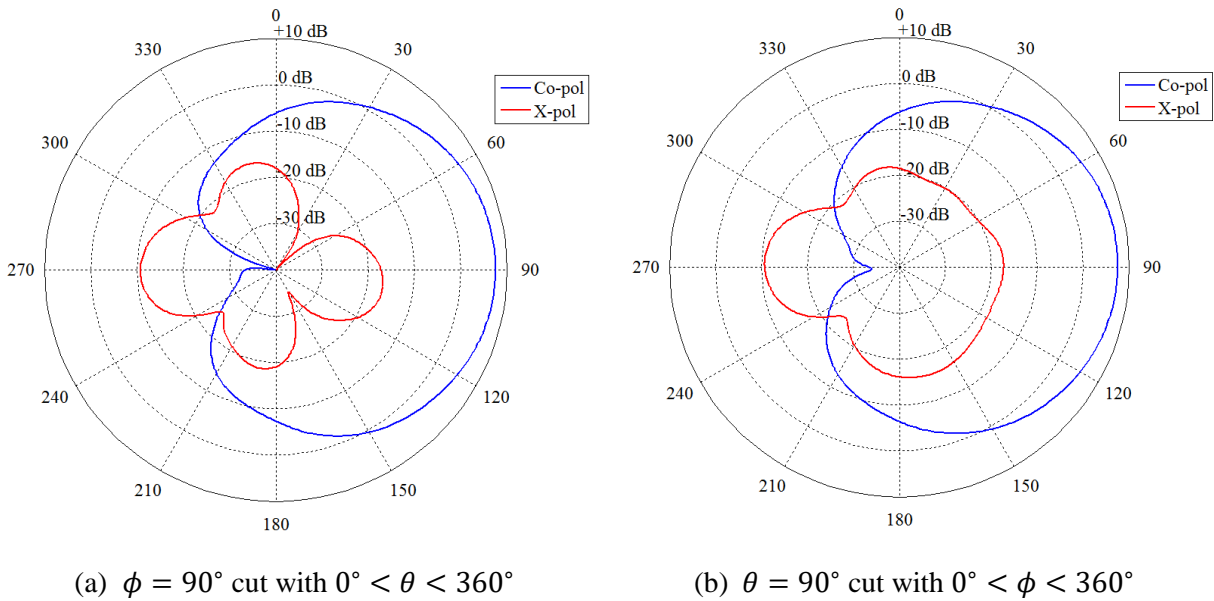
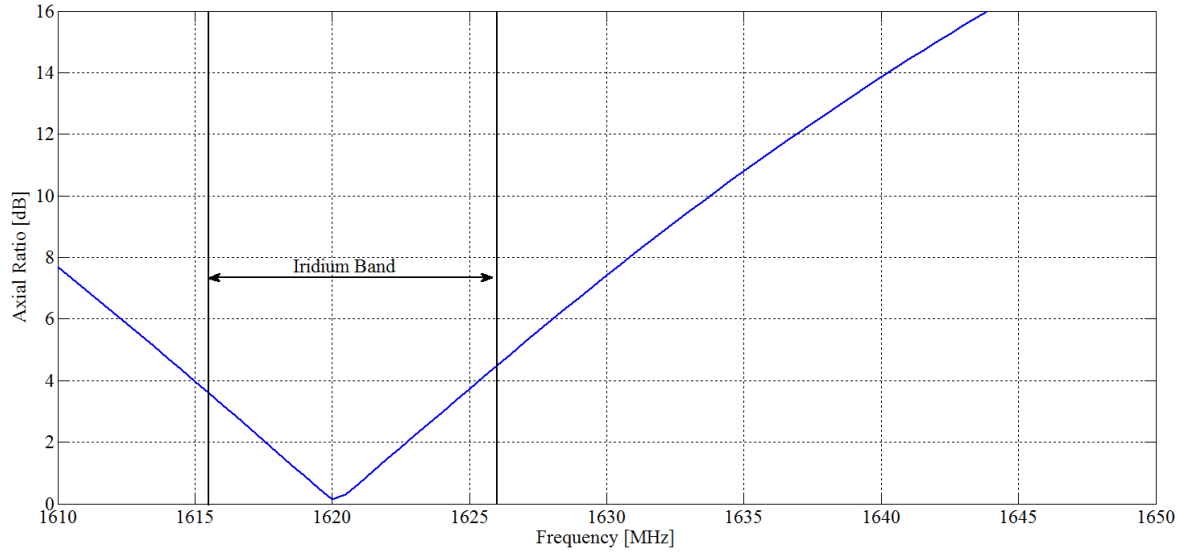


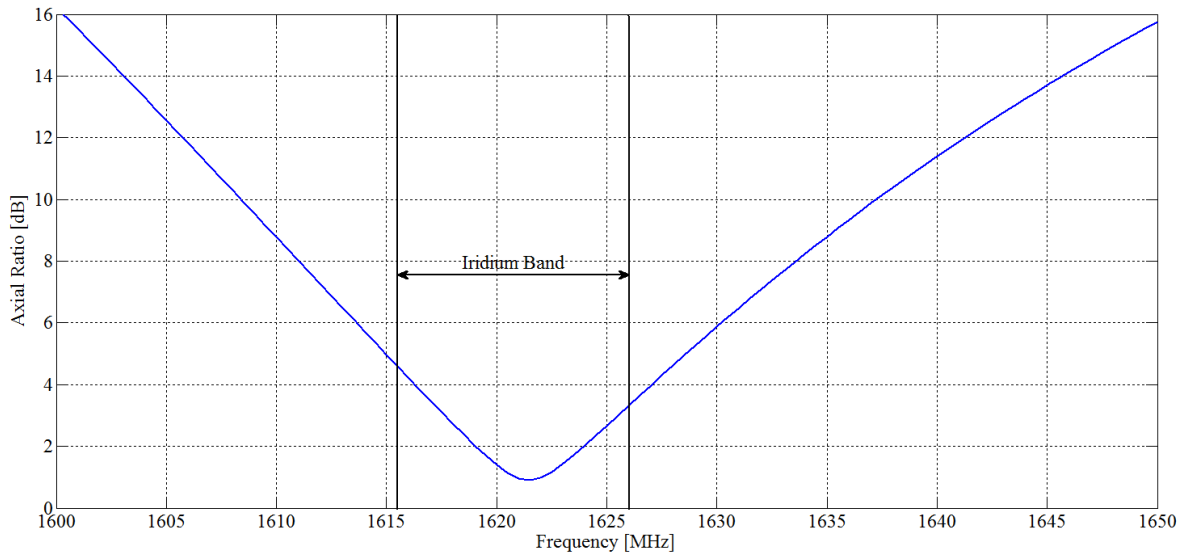
Figure 4.8 Back-to-back patch antenna gain simulation with the $+\hat{y}$ -patch on and the $-\hat{y}$ -patch off. The co-polarization is with respect to a RHCP and the cross-polarization is with respect to a LHCP receiver. Note that the gain is +3 dB higher in this case when compared to both patches being on in Figure 4.7.

It should be stressed that when only a single patch is on, the gain is +3 dB more than when both patches are on. The finite sized ground plane allows the fields along the $+\hat{x}$ - and $-\hat{x}$ -axes to add in and out of phase when both patches are on. This causes the more uniform looking pattern in Figure 4.7(d). Therefore, since the pattern is less directional, the maximum gain with both patches excited is decreased. The interaction of the fields of the two patches will be explored in further detail in Section 4.7.

Figure 4.9 shows the simulated axial ratio performance of the back-to-back patch antenna when both patches were turned on and when only one patch was on. In both cases, the axial ratio was less than 4.5 dB across the Iridium band as shown in Figure 4.9(a). This was very close to the required $AR < 4$ dB guideline. Therefore, the antenna would provide sufficient RHCP for satellite communications.



(a) Both patches on



(b) +ŷ-patch on; -ŷ-patch off

Figure 4.9 Simulated back-to-back patch antenna axial ratio bandwidth at $\phi = 90^\circ, \theta = 90^\circ$.

4.4. Fabrication, Reflection Coefficient, and Radiation Pattern Measurements

Two identical patch antenna elements were fabricated using the dimensions as shown in Figure 4.4. The patches were manufactured on RT/duroid 5880 material with a permittivity of $\epsilon_r' = 2.2$ and loss tangent of $\tan\delta = 0.0009$ [40]. The substrate thickness was $h = 1.57$ mm with double-sided 1 oz electrodeposited copper cladding. The fabricated patches are shown below in Figure 4.10. A female SMA connector was soldered onto each of the patches at the edge of the quarter wave transformer feed.

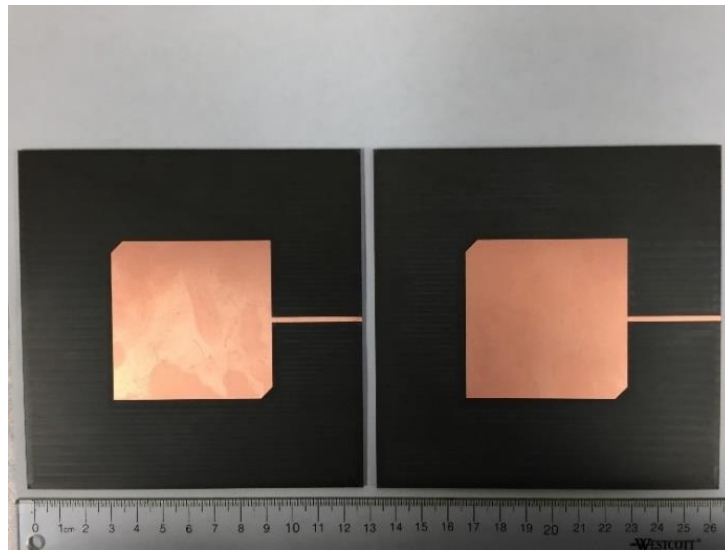


Figure 4.10 *Identical fabricated patch antenna elements.*

Figure 4.11 shows a block diagram of the back-to-back patch antenna setup used for measurement on the VNA. A 180° hybrid coupler was used as a 3 dB power splitter for the two patch antennas by match terminating the Δ -port with a $50\ \Omega$ load. Patch 1 was connected to the 0° -port and patch 2 was connected to the $0^\circ/180^\circ$ -port. Both antennas were fed with a 0° phase shift.

The reflection coefficient and **insertion loss** (IL) of the hybrid coupler was measured on the VNA as shown in Figure 4.12. Table 4.1 summarizes the reflection coefficient ($|S_{ii}|$ [dB]) and the negative insertion loss ($|S_{ij}|$ [dB]) for the hybrid coupler.

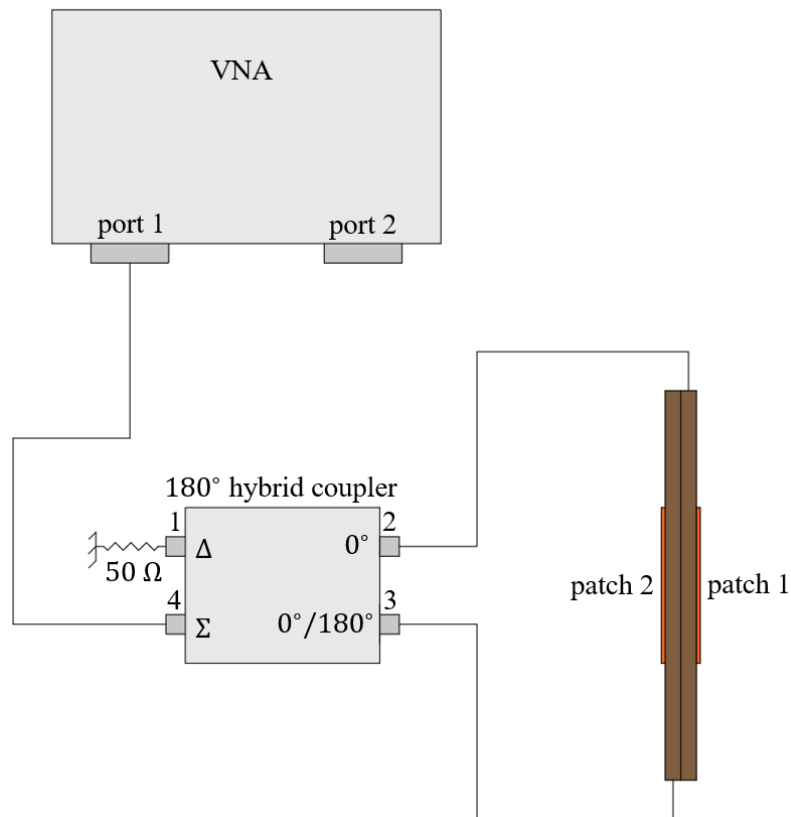
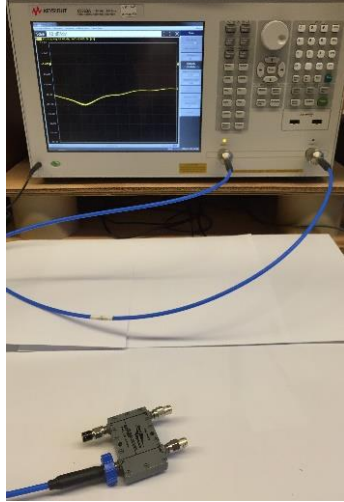
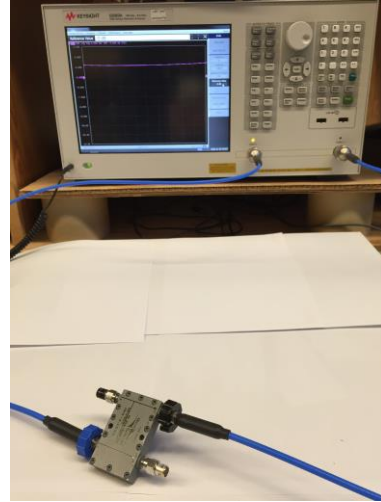


Figure 4.11 Block diagram of the VNA measurement setup.



(a) Reflection coefficient measurement



(b) Insertion loss measurement

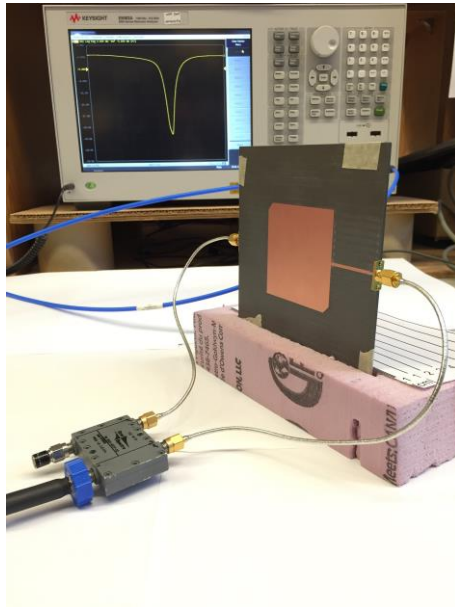
Figure 4.12 180° hybrid coupler under test on the VNA

Table 4.1 Reflection coefficient and negative insertion loss of the 180° hybrid coupler.

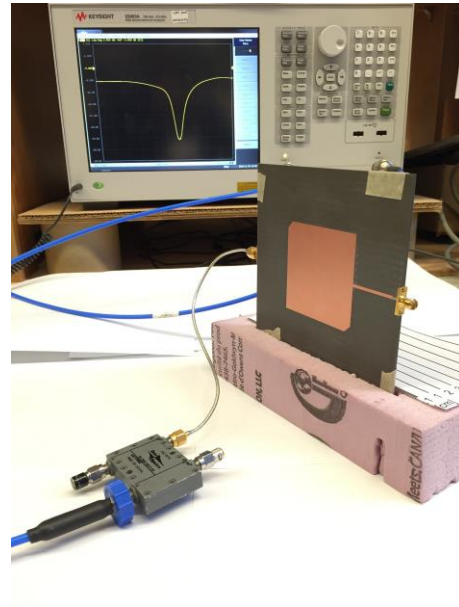
Path	Value ($1400 < f < 1800$ MHz)
Δ -port	$ S_{11} \leq -33$ dB
0° -port	$ S_{22} \leq -19$ dB
$0^\circ/180^\circ$ -port	$ S_{33} \leq -20$ dB
Σ -port	$ S_{44} \leq -30$ dB
Σ -port to 0° -port	$ S_{24} = -4.1$ dB
Σ -port to $0^\circ/180^\circ$ -port	$ S_{34} = -3.4$ dB

It was important to have a low reflection coefficient value at the Σ -port since anything reflected to the VNA from here would distort the reflected data from the antennas. This would give an inaccurate reflection coefficient measurement of the back-to-back patch system. The reflection coefficient of all four ports of the coupler was measured for completeness, but the other three ports were less important for the scope of this thesis. The negative insertion loss from the Σ -port to the 0° -port and the Σ -port to $0^\circ/180^\circ$ -port was -4.1 dB and -3.4 dB respectively.

The back-to-back patch antenna reflection coefficient was measured using the two different setups as shown in Figure 4.13. Figure 4.13(a) shows the setup when both antennas are on and Figure 4.13(b) shows the setup when one antenna is on and the other is off. An antenna is considered off when it is left open circuited and its port on the coupler has been match terminated.



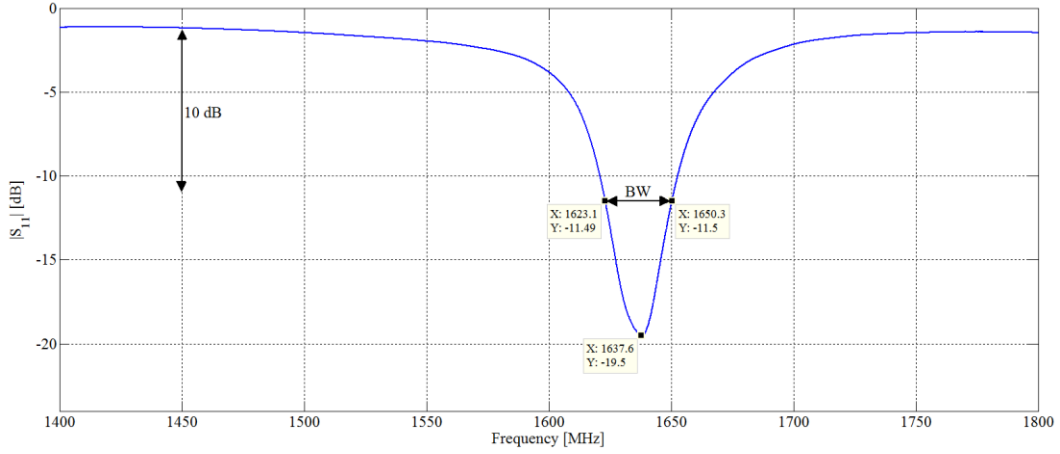
(a) Both patches on



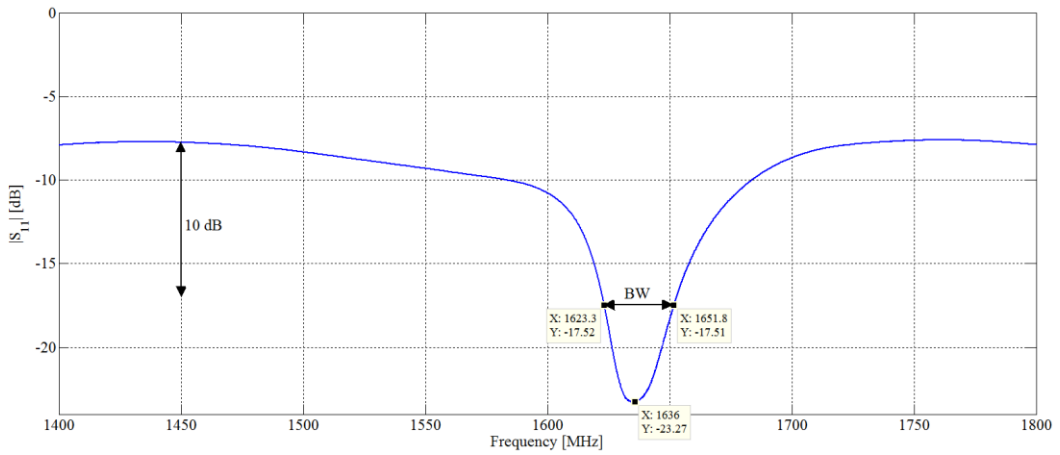
(b) One patch on and the other patch off

Figure 4.13 *Back-to-back patch antenna reflection coefficient measurement setup.*

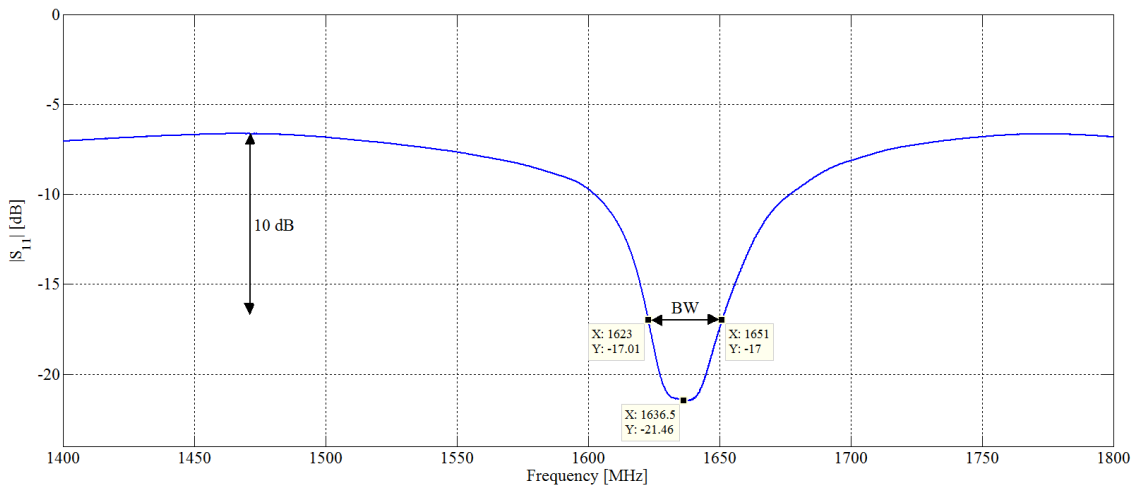
The reflection coefficient when both patches were turned on is shown in Figure 4.14(a). The resonant frequency was 1637.6 MHz with a reflection coefficient of -19.5 dB. Figure 4.14(b) shows the reflection coefficient when patch 1 was on and patch 2 was off. The resonant frequency was 1636 MHz with a reflection coefficient of -23.27 dB. Figure 4.14(c) shows the resonant frequency when patch 1 was off and patch 1 was on. The resonant frequency was 1636.52 MHz with a reflection coefficient of -21.46 dB.



(a) Both patches on



(b) Patch 1 on; patch 2 off



(c) Patch 1 off; patch 2 on

Figure 4.14 Reflection coefficient of the back-to-back patch antenna measured on the VNA.

We were unable to do any tuning since the fabricated patches had a higher resonant frequency than the Iridium center frequency of 1621 MHz. To decrease the resonant frequency, the patches would need to be slightly larger, which would require the antennas to be refabricated. This will not be done in this thesis. Patch 1 and patch 2 had slightly different reflection coefficients due to manufacturing intolerances. The bandwidth was measured -10 dB down from the baseline. The reason the baseline was not at 0 dB was due to the insertion loss of the hybrid coupler. The baseline when patch 1 was on and patch 2 was off was about -8 dB. This was accounted for by the -4.1 dB of negative insertion loss experienced as the reflected wave had to forward and backward through the coupler. The baseline when patch 2 was on and patch 1 was off was about -7 dB since the negative insertion loss of the coupler through the Σ - to $0^\circ/180^\circ$ -ports was -3.4 dB. The baseline when both patches were on was about -1.5 dB. When one patch was turned off, the baseline was dropped down approximately -6 dB due to the 3 dB of power lost each way through the coupler. The -10 dB bandwidth when both patches were turned on was 27.2 MHz. When patch 1 was turned on and patch 2 was off the bandwidth was 28.5 MHz and when patch 2 was turned on and patch 1 was turned off was 28 MHz. As expected, the -10 dB bandwidth is roughly the same for all three cases since both antennas were nearly identical. Although the frequency bandwidth of the fabricated antennas was shifted slightly higher than the simulation, the bandwidth values were within agreement. We recall that the simulation -10 dB bandwidth in Section 4.3 was 29 MHz.

The back-to-back patch antenna was mounted in the Satimo spherical near-field system to measure its radiation pattern as shown in Figure 4.15.

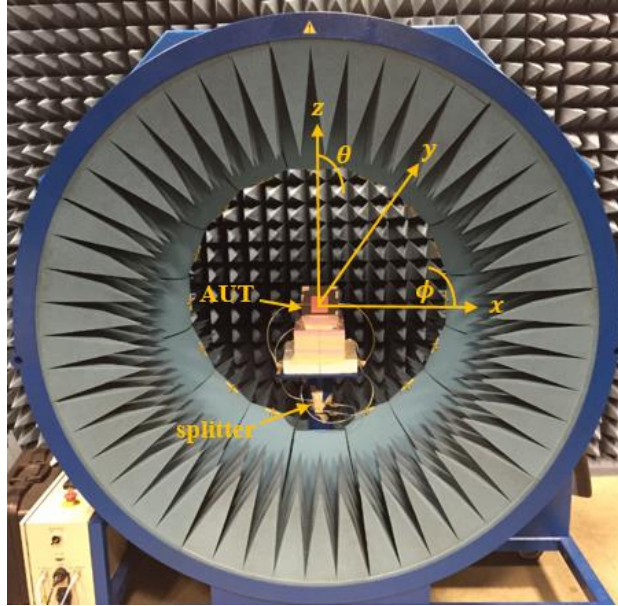
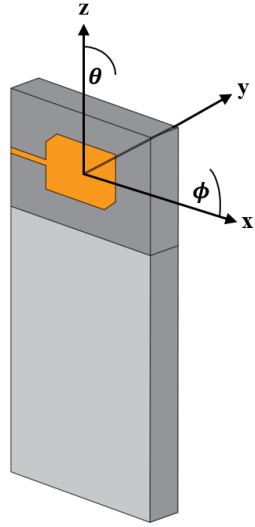


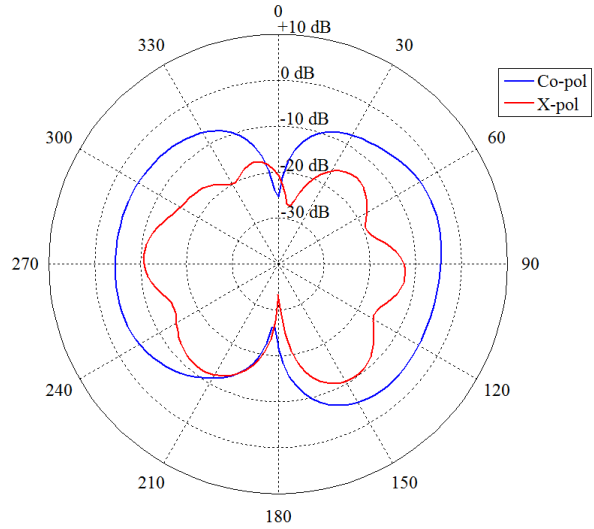
Figure 4.15 *Back-to-back patch antenna radiation pattern measurement setup.*

The insertion loss of the cables and devices in front of the AUT in the Satimo system was measured on the VNA and determined to be -1.5 dB for $1610 < f < 1660$ MHz. All radiation pattern measurements below include the insertion loss of the cables and devices in front of the AUT. The frequency was swept from $1610 - 1660$ MHz with a step size of 0.5 MHz for all radiation pattern measurements. To model the Iridium frequency band, we chose 1633 MHz as the center frequency since it had the lowest axial ratio. Had this frequency been lower than the Iridium center frequency, we would have been able to tune the antenna by trimming the patches until 1621 MHz was obtained. However, refabricating the antennas was unnecessary for this thesis and therefore a 10.5 MHz bandwidth equivalent of $1628 - 1638.5$ MHz with a center frequency of 1633 MHz was chosen to represent the Iridium frequency band in this thesis. Note that $1628 - 1638.5$ MHz was still within the -10 dB bandwidth of the back-to-back patch antenna as verified in Figure 4.14. Both antennas were fed with an identical 0° phase shift.

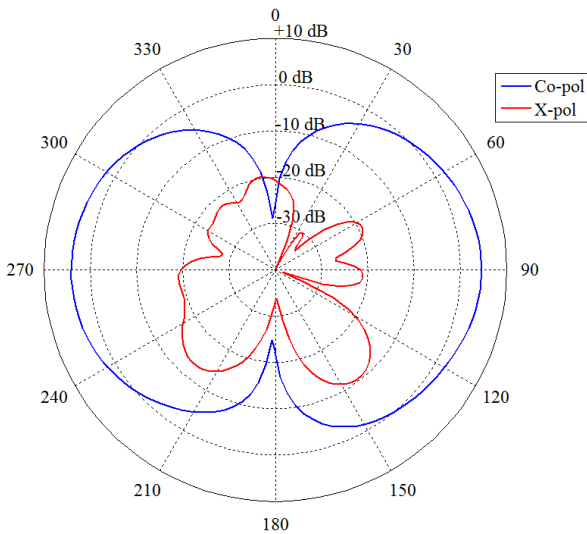
The radiation pattern when both patch antennas were turned on was measured as shown in Figure 4.16. The maximum gain was determined to be +4.5 dB, which included the insertion loss of the front-end devices before the antenna. Since the front-end insertion loss of 1.5 dB was not simulated, 1.5 dB needs to be added to the measured gain to get a direct comparison. In this case, the maximum measured gain would be +6 dB compared to the simulated gain of +4.5 dB. We note that the Satimo system had a gain tolerance of ± 2 dB, so the +1.5 dB difference in gain is accounted for. Figure 4.16(b) shows the measured gain in the $\phi = 0^\circ$ cut, Figure 4.16(c) shows the measured gain in the $\phi = 90^\circ$ cut, and Figure 4.16(d) shows the measured gain in the $\theta = 90^\circ$ cut. The pattern had very prominent nulls in the $\phi = 0, 90^\circ$ cuts and had a more uniform look in the $\theta = 90^\circ$ cut with a gain varying between +4.5 dB and -4.5 dB. All three patterns matched the simulation in Figure 4.7.



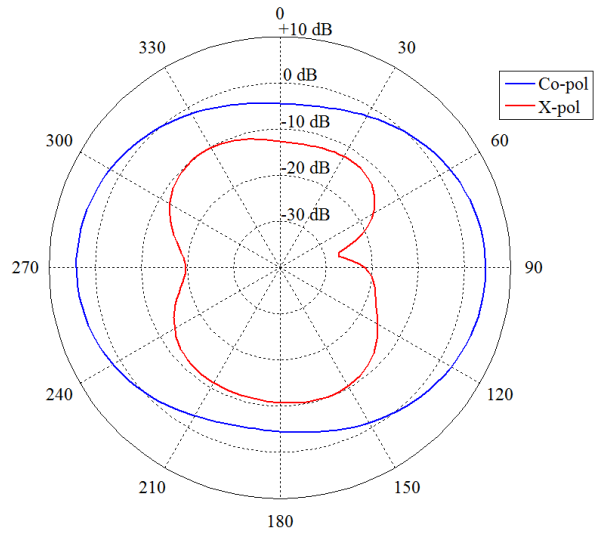
(a) Orientation of the antenna



(b) $\phi = 0^\circ$ cut with $0^\circ < \theta < 360^\circ$



(c) $\phi = 90^\circ$ cut with $0^\circ < \theta < 360^\circ$



(d) $\theta = 90^\circ$ cut with $0^\circ < \phi < 360^\circ$

Figure 4.16 Back-to-back patch antenna gain measurement with both patches on. The co-polarization is with respect to a RHCP and the cross-polarization is with respect to a LHCP receiver. See Figure 4.7 for comparison with the simulated gain. Note the phone case was not present in the measurement.

The radiation pattern when one of the patches was turned off while the other was left on is shown in Figure 4.17. The off patch was left open circuited and the disconnected cable was terminated in a matched load. The maximum gain remained at +4.5 dB. Since neither the 3 dB

splitter nor the 1.5 dB insertion loss was modelled in the simulation, +4.5 dB needs to be added to the measured value for a direct gain comparison with the simulation. In this case, the measured maximum gain would be +9 dB compared to the simulated gain of +7.5 dB. This is within the ± 2 dB tolerance of the Satimo system. Figure 4.17(a) shows the measured gain in the $\phi = 90^\circ$ cut and Figure 4.17(b) shows the measured gain in the $\theta = 90^\circ$ cut, which matches the simulation in Figure 4.8.

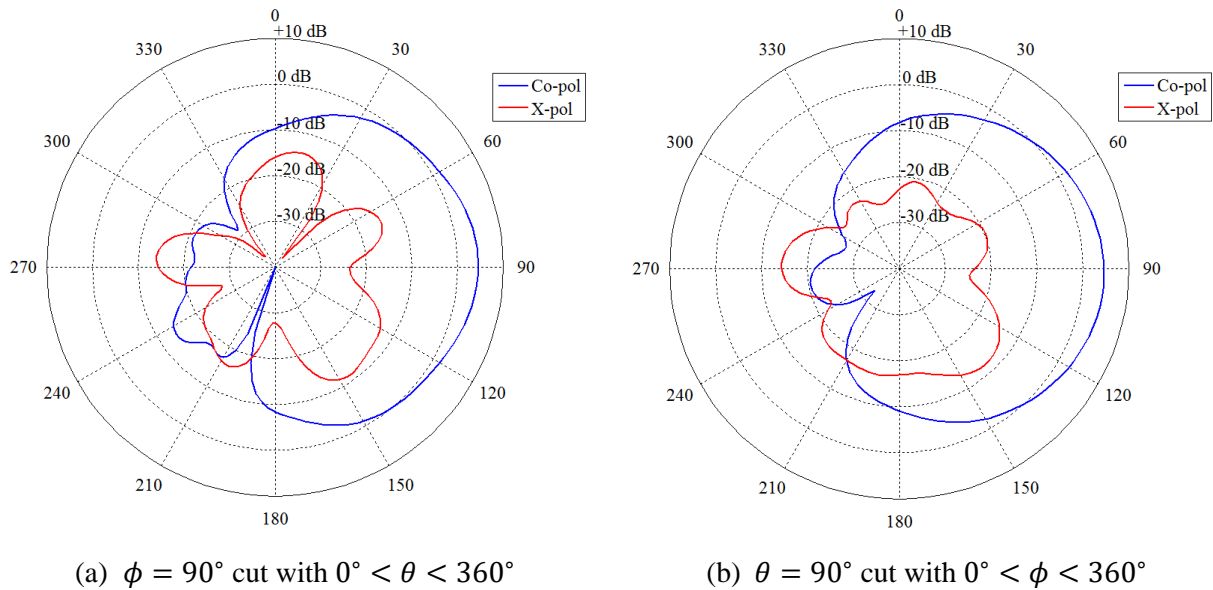
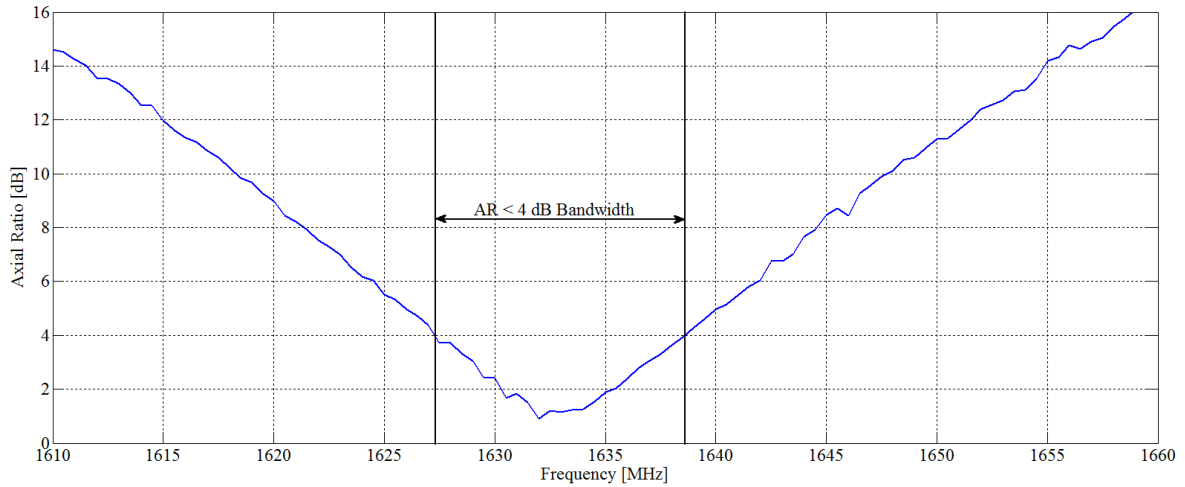


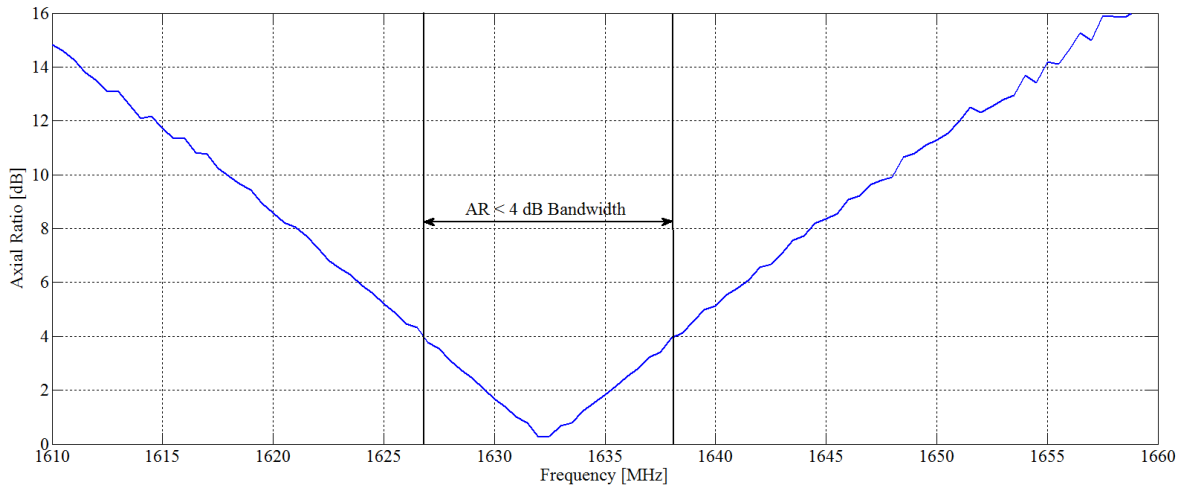
Figure 4.17 Back-to-back patch antenna gain measurement with the $+\hat{y}$ -patch on and the $-\hat{y}$ -patch off. The co-polarization is with respect to a RHCP and the cross-polarization is with respect to a LHCP receiver. See Figure 4.8 for comparison with the simulated gain.

The measured axial ratio of the back-to-back patch antenna with both patches on and then only one patch on is shown in Figures 4.18(a) and 4.18(b) respectively in the direction of maximum radiation. In both cases, the axial ratio was less than 4 dB for the defined bandwidth of 1628 – 1638.5 MHz. With proper tuning to the Iridium frequency band, the back-to-back patch antenna design would have suitable RHCP for Iridium communications. The axial ratio at the center

frequency of 1633 MHz was also measured against elevation angle. For an elevation angle of less than 70° with respect to the horizon, the axial ratio was less than 4 dB.



(a) Both patches on



(b) $+\hat{y}$ -patch on, $-\hat{y}$ -patch off

Figure 4.18 Back-to-back patch antenna measured axial ratio bandwidth at $\phi = 90^\circ, \theta = 90^\circ$.

A summary of the fabricated back-to-back patch antenna design is shown in Table 4.2. Based on the measurements done in this section, we can conclude that the back-to-back patch antenna would meet the guidelines for Iridium communications. However, the antenna would need to be

tuned to the proper frequency and be miniaturized before being suitable for use in a handheld device.

Table 4.2 *Back-to-back patch antenna with both patches on specifications.*

Specifications	Value
Center Frequency	1637.5 MHz
−10 dB Bandwidth	27 MHz (1623 – 1650 MHz)
Maximum Gain with Front-End @ 1633 MHz	+4.5 dB ±2 dB
HPBW	64°
Axial Ratio < 4 dB	Elevation angle < 70°
Polarization	RHCP
Impedance	50 Ω

4.5. Human Head Influence on the Radiation Pattern Using a Crude Phantom

To investigate the effects of RF energy on human beings, usually a phantom is first used in place of a real human subject. A phantom is a dielectric model of a specific part of the human body. In SAR certification report for the iPhone 5, a table of the electrical properties of a human head model were shown at various frequencies with a complex relative permittivity of $\hat{\epsilon}_r = 40.3 - j14.1$ at 1640 MHz [41]. A homogenous liquid phantom made of glycerin and water was used as a crude model of the head. Figure 4.19 shows a plot of the complex permittivity versus frequency for two different mixtures of glycerin and water. The complex permittivity of the “blue phantom” was $\hat{\epsilon}_r \approx 42.5 - j22.5$ at 1600 MHz. This provided us with similar properties to that used in [41].

The bottle containing the “blue phantom” was made of 1.88 mm thick **polyethylene terephthalate** (PET) with a diameter of 7.2 cm and a height of 21.6 cm.

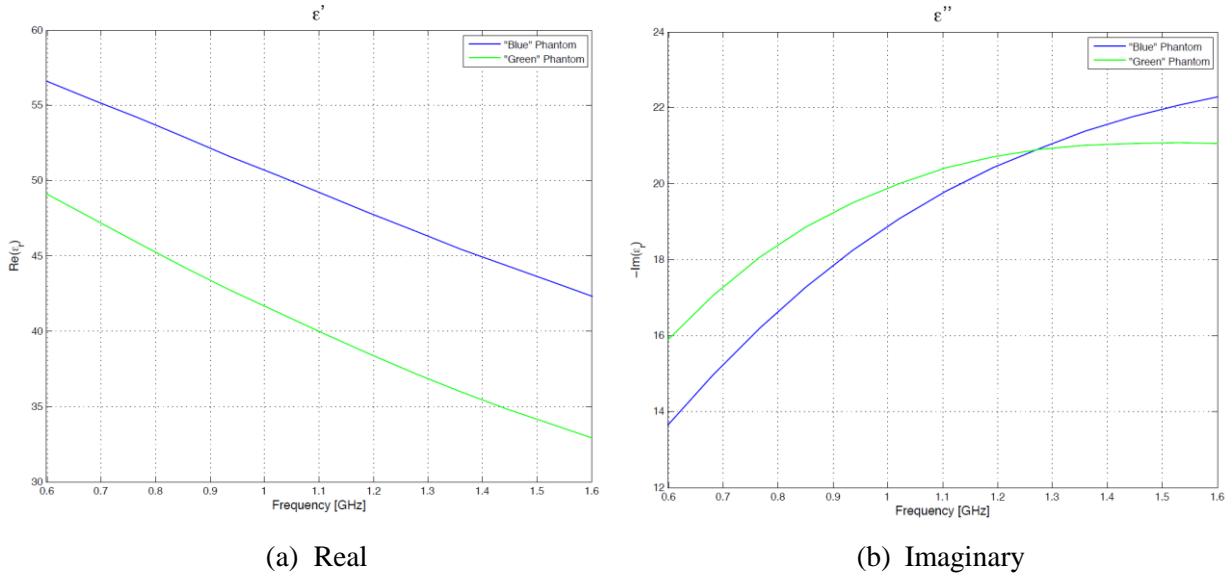


Figure 4.19 Complex permittivity of the “blue phantom” that was used as a crude model of the human head.

To investigate the effects of the phantom on the back-to-back patch antenna, the phantom was placed 1 mm away from the $-\hat{y}$ -patch as shown in Figure 4.20. A measurement was taken with both patches turned on as shown in Figure 4.21(a). We can see that the phantom is perturbing the pattern of the $-\hat{y}$ -patch at $\theta = 270^\circ$. The gain at $\theta = 270^\circ$ is now around -4 dB, where it was previously $+4.5$ dB with no obstructions as shown in Figure 4.17(c). The $-\hat{y}$ -patch was turned off with the $+\hat{y}$ -patch left on to determine whether the phantom would look invisible to the opposite patch. The results are shown in Figure 4.21(b). Figure 4.21(b) matched Figure 4.17(a) very closely, which indicated that the phantom had a negligible effect on the patch opposite to it. Therefore, we would expect little radiation to be absorbed by a nearby human head when the patch facing the human head is turned off based on the far-field results.

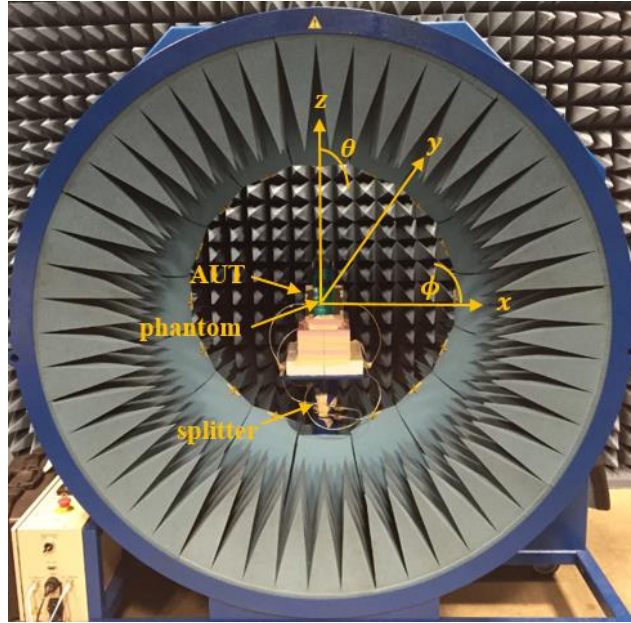


Figure 4.20 Back-to-back patch antenna radiation pattern measurement setup with the “blue phantom” used to roughly emulate the human head.

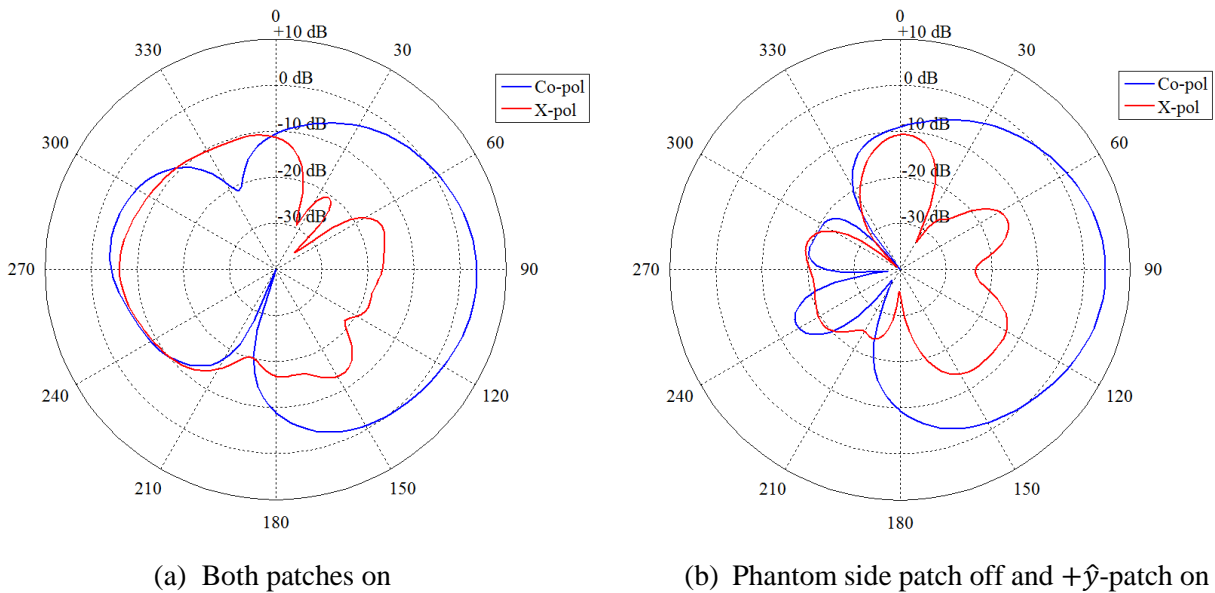


Figure 4.21 Gain measurement with the “blue phantom” 1 mm away from the back-to-back patch antenna in the $\phi = 90^\circ$ cut with $0^\circ < \theta < 360^\circ$. The co-polarization is with respect to a RHCP and the cross-polarization is with respect to a LHCP receiver. See Figures 4.16(c) and 4.17(a) for a comparison of the gain when no phantom was present.

4.6. SAR Level Simulation

A SAR level simulation was done in HFSS using the back-to-back patch antenna model from Section 4.3 with a homogenous phantom of the human head. The phantom was placed at various distances away from the antenna to determine where the peak SAR levels would become safe for human exposure. In [42], the 50th percentile for a human head size in the side plane of the head was found to be 23.2×19.7 cm for males and 21.8×18.7 cm for females. The average male human head size was modelled as an ellipsoid in HFSS with a major axis of 23.2 cm and a minor axis of 19.7 cm. The complex relative permittivity used for the phantom was $\hat{\epsilon}_r = 40.3 - j14.1$ at 1640 MHz. This was the industry standard for modelling the human head for SAR level certification [41]. The SAR simulation was done at 1621 MHz to best represent the Iridium frequency band. Solara's Field Tracker 2100 was used as a reference for the maximum transceiver power since it is an industry standard handheld Iridium device. The Field Tracker 2100 can produce 2 W of power at the output of the transceiver [9]. Since the power in the back-to-back patch antenna was split between the two patches and 1.5 dB of power was lost in the front-end (see Section 4.4), 0.71 W of power would be delivered to each patch. The built-in SAR calculator in HFSS was used since it uses the industry standard IEEE P1528 method of calculating SAR in (1.1), which is required for device certification [41]. See Section 1.1 for more detail on how SAR is calculated.

Figure 4.22 shows the SAR simulation setup for the back-to-back patch antenna in HFSS. The phantom was moved to various distances away from the back-to-back patch antenna to determine

what distance the SAR <math> < 1.6 \frac{W}{kg}</math>. The SAR level in the phantom along the \hat{y} -axis at various distances away from the antenna is shown in Figure 4.23.

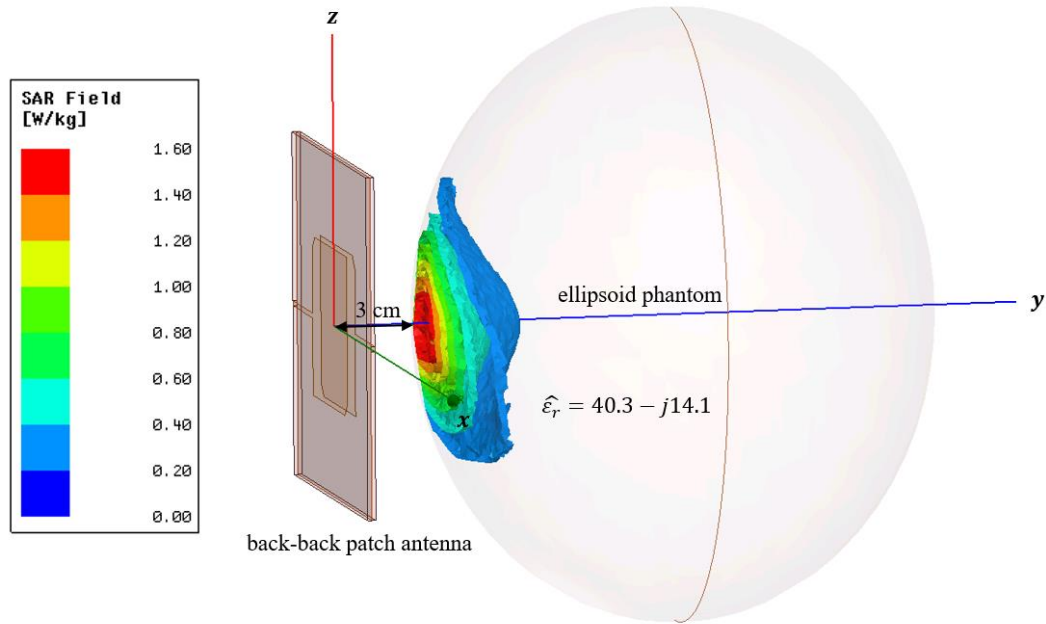


Figure 4.22 3D SAR level simulation using a homogenous ellipsoid model of the human head 3 cm away from the back-to-back patch antenna for 0.71 W power delivered to each patch.

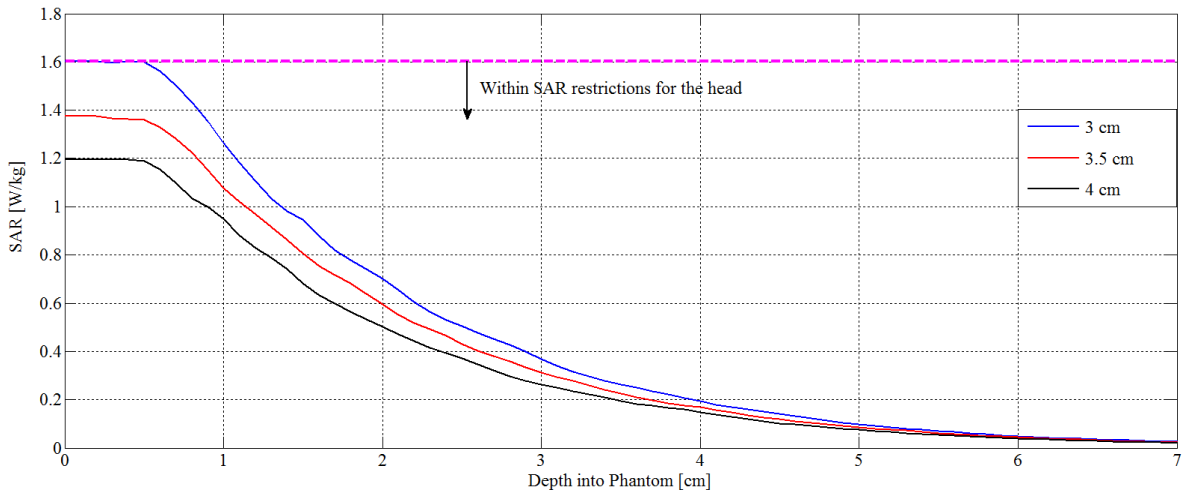
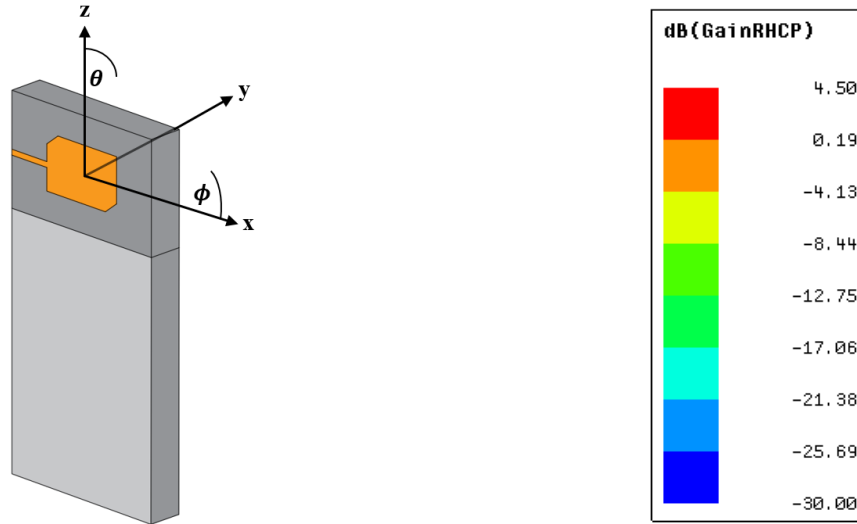


Figure 4.23 SAR level simulation along the y-axis using a homogenous ellipsoid phantom at various distances away from the back-to-back patch antenna for 0.71 W power delivered to each patch. Figure 4.22 shows the orientation of the antenna and the phantom.

Figure 4.23 shows that the SAR level was the highest near the surface and decreased as the power penetrated through the phantom. Outside of 3 cm, the peak SAR $\leq 1.6 \frac{\text{W}}{\text{kg}}$. This distance will be investigated further in Chapter 5 since as a human head approaches 3 cm, the impedance monitoring system would need to turn off the patch facing the user's head to be within SAR limitations.

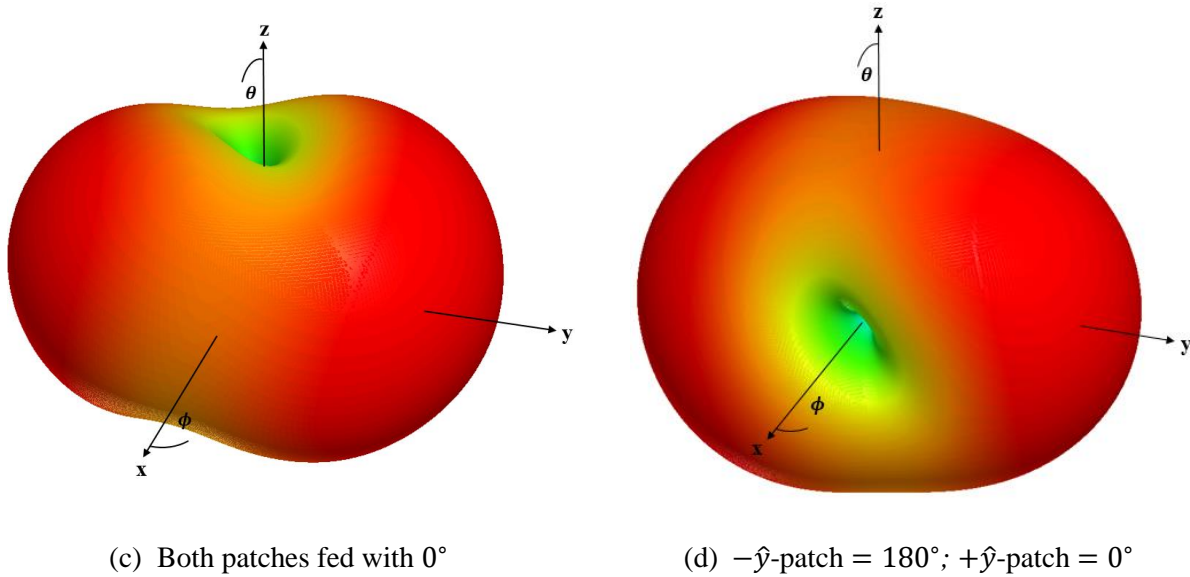
4.7. Beam Shaping Using Feed Phasing

The motivation for the design of the back-to-back patch antenna was to create a somewhat omnidirectional antenna. This means that we want as uniform of gain as possible in the broadside direction of the antenna. Initially, both patches were fed with identical phase shifts to try to provide 360° degrees of coverage in the broadside direction. From Figure 4.7(d), we see that the simulated antenna provided a $+4.5 \text{ dB} > G_{\text{RHCP}} > -3 \text{ dB}$ in the broadside direction. The phase of the $-\hat{y}$ -patch feed was changed from 0° to 180° in HFSS. The phase of the $+\hat{y}$ -patch was left at 0°. When both patches were on, a phase difference between the two patches caused the nulls along the $+\hat{z}$ - and $-\hat{z}$ -axes to rotate by 90° in the xz -plane. A 3D illustration of this is shown in Figure 4.24 with the back-to-back patch antenna centered at the origin in the xz -plane.



(a) Orientation of the antenna

(b) Legend



(c) Both patches fed with 0°

(d) $-\hat{y}$ -patch = 180° ; $+\hat{y}$ -patch = 0°

Figure 4.24 3D simulation of different feed phasing for the back-to-back patch antenna (located in the xz -plane). Note the phone case was not present in the simulation.

Figure 4.25 shows only the xz -plane of Figure 4.24. Figure 4.25(a) shows the gain when both patches are excited with a 0° phase shift and Figure 4.25(b) shows the gain when there is a 180° phase shift between the two patches. By comparing Figures 4.25(a) to 4.25(b), we can see that the

null was rotated by 90° . Both gains are with respect to a RHCP receiver with a maximum gain of -3 dB.

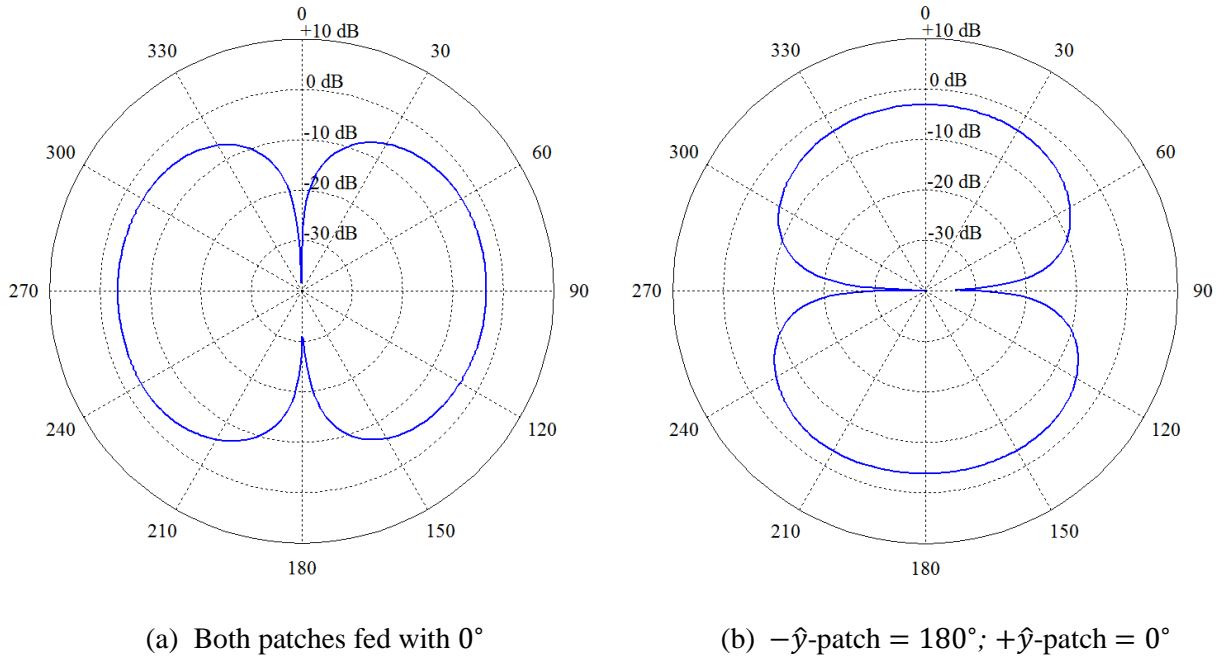
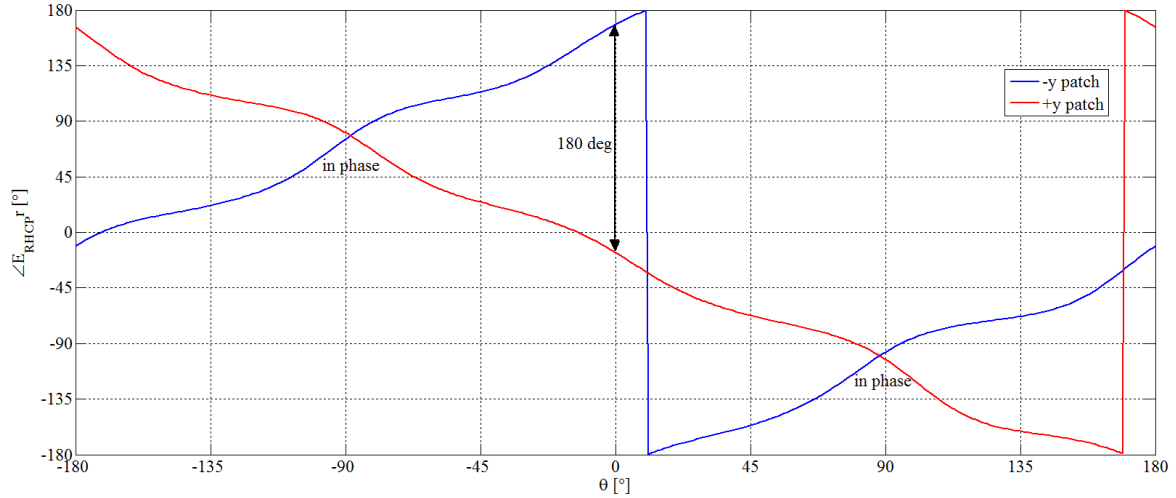
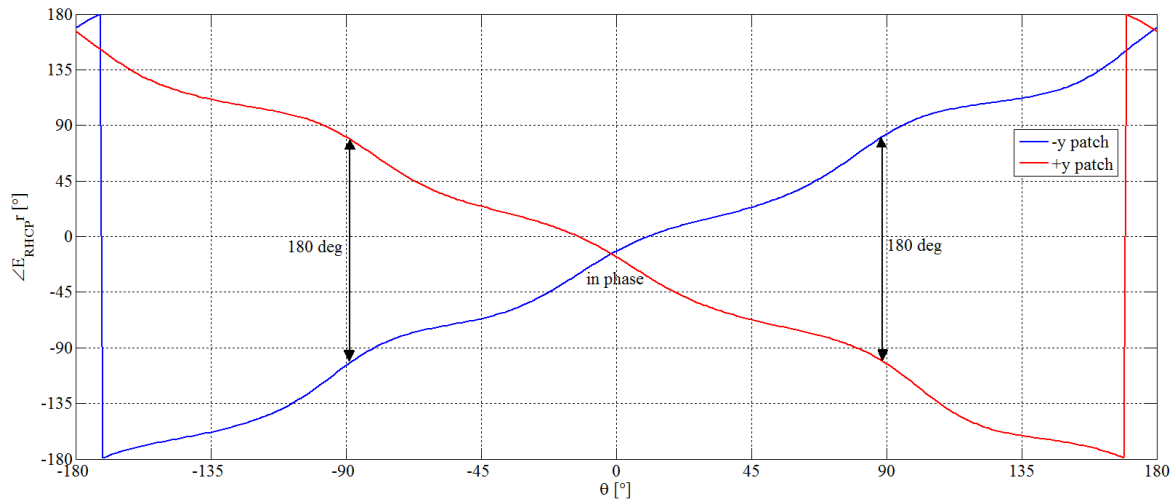


Figure 4.25 Feed phasing effects on shaping the null of the back-to-back patch antenna in the xz -plane. $\phi = 0^\circ$ and $0^\circ < \theta < 360^\circ$. Both gains are with respect to a RHCP receiver. Refer to Figure 4.24 for a 3D view.

The phase of the far-field electric fields with the r -dependency removed was simulated for each patch individually with the other patch off. This was done to determine how the far-fields of the two patches were interacting. Figure 4.26(a) shows a plot of the electric field phase of each patch in the xz -plane when both feeds were excited with a 0° phase shift. Since the $+\hat{y}$ -patch is fed with a quarter wave transformer at $\theta = 90^\circ$, the fields at $\theta = 90^\circ$ will have a phase near -90° due to the e^{-j90° phase shift of the transformer. The $-\hat{y}$ -patch on the other hand is fed with a quarter wave transformer at $\theta = -90^\circ$, therefore, the fields at $\theta = -90^\circ$ will have a phase near $+90^\circ$ due to the e^{+j90° phase shift of the transformer.



(a) Both patches fed with 0°



(b) $-\hat{y}$ -patch = 180° ; $+\hat{y}$ -patch = 0°

Figure 4.26 Analysis of the beam steering using feed phasing by looking at the phase of the electric field in the $\phi = 0^\circ$ cut (xz -plane) as shown in Figure 4.25.

Thus, the electric fields of both patches will be in phase around $\theta = \pm 90^\circ$, which can be verified in Figure 4.25(a) since the gain is maximum there. Both patches are 180° out of phase around integer multiples of $\theta = 180^\circ$. This is reflected in Figure 4.25(a) where the nulls occur at $\theta = 0^\circ, 180^\circ$.

Figure 4.26(b) shows a plot of the electric field phase of each patch in the xz -plane when the $-\hat{y}$ -patch was excited with a 180° phase shift and the $+\hat{y}$ -patch was still excited with 0° . Comparing Figures 4.26(a) and 4.26(b) we can see that the $-\hat{y}$ -patch phase has shifted down 180° . Now, around $\theta = \pm 90^\circ$ the two patches have electric fields that are out of phase, therefore, shifting the nulls to $\theta = 90^\circ, 270^\circ$ in Figure 4.25(b). The electric fields of both patches are now in phase at integer multiples of $\theta = 180^\circ$, which is where the maximum of the pattern in the xz -plane occurs in Figure 4.25(b). A simple relation for the null rotation in the xz -plane versus the phase difference between feed excitations is shown in (4.2).

$$\text{null rotation}_{xz\text{-plane}} = \frac{\angle \text{feed}_{+\hat{y}\text{patch}} - \angle \text{feed}_{-\hat{y}\text{patch}}}{2} \quad (4.2)$$

Possible applications for beam steering of the null in the xz -plane of the antenna would be as follows:

- Locking into satellites directly overhead by optimizing the location of the null to increase signal reliability
- Adaptatively controlling the null to reduce radiation exposure to a human user

4.8. Conclusion

In this chapter, a back-to-back patch antenna was successfully designed, simulated, fabricated, and measured. The fabricated back-to-back patch antenna provided a maximum gain of $+4.5$ dB in the direction broadside to the antenna with an axial ratio of less than 4.5 dB across a 10.5 MHz -10 dB bandwidth. Both specifications are within the acceptable guidelines for Iridium handheld

communication devices. It was shown in Section 4.5, that when a phantom was placed near the patch that was off, the on patch on the other side of the ground plane was negligibly effected by the phantom. Based on the far-field results, this suggests that if the patch facing the human user's body was turned off, the radiation exposure for that individual would be significantly decreased. The SAR simulation carried out in Section 4.6 showed that 3 cm was required between the back-to-back patch antenna and the phantom for SAR levels to be within government restrictions in Canada. This distance will be used as a reference for the impedance monitoring control system in Chapter 5. Lastly, it was shown that the nulls in the plane of the patch could be rotated within that plane by feeding the two patches out of phase.

Chapter 5

Impedance Monitoring System

5.1. Overview

In this chapter, an impedance monitoring based system was investigated to adaptively control the pattern of the back-to-back patch antenna for reducing radiation exposure to a human user. The same “blue phantom” used in Section 4.5 was used to determine the sensitivity of the input impedance of the back-to-back patch antenna in proximity to a human head. By investigating the input impedance sensitivity, it was determined that a method of adaptively controlling the antenna could be formed based on the orientation of the antenna.

5.2. Reflection Coefficient Sensitivity

To study the feasibility of an impedance monitoring based system, the back-to-back patch antenna was set up with the “blue phantom” and the reflection coefficient was measured as shown in Figure 5.1. The “blue phantom” provided a crude representation of the human head. The 180° hybrid coupler that was measured in Section 4.4 was used to split the power between the two patches. With both patches turned on, the main interest was to explore how the reflection coefficient varied as the phantom approached one of the antennas. This was done to simulate a human user placing the phone up against their head.

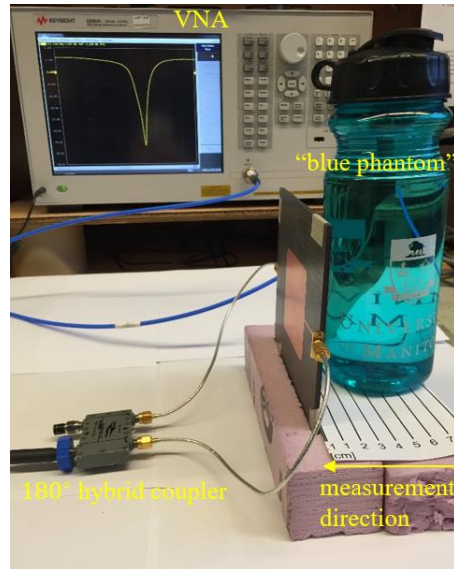


Figure 5.1 Measurement setup with the “blue phantom” to investigate the reflection coefficient sensitivity of the back-to-back patch antenna.

Figure 5.2 shows the measured reflection coefficient as the phantom was gradually moved closer to the back-to-back patch antenna. Table 5.1 summarizes the key points on Figure 5.2. The key points were the reflection coefficient values at the resonant frequency and the upper frequency, f_H , of the -10 dB bandwidth of the back-to-back patch antenna.

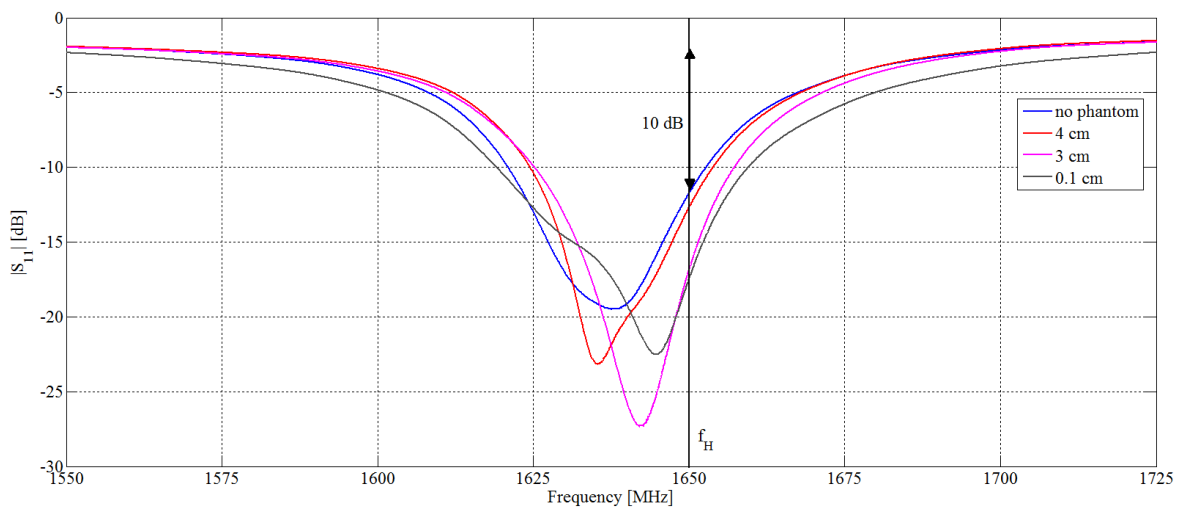


Figure 5.2 Reflection coefficient in the presence of the “blue phantom” with both patches on.

Table 5.1 Resonant frequency shift in the presence of the “blue phantom” with both patches on.

Phantom Distance	$ S_{11} _{min}$	f_0	$ S_{11} _{f_H}$
No Phantom	-19.5 dB	1637.6 MHz	-11.7 dB
4 cm	-23.2 dB	1635.3 MHz	-12.7 dB
3 cm	-27.4 dB	1642 MHz	-16.7 dB
0.1 cm	-22.5 dB	1645 MHz	-17.4 dB

As the phantom came within 3 cm of the antenna, the resonant frequency of the back-to-back patch antenna began to shift higher in frequency. Inside of 3 cm, random fluctuations in the room had a negligible effect on the reflection coefficient. Outside of 4 cm the resonant frequency became dependent on random movements in the room and therefore would not provide a suitable method of detection. The resonant frequency never increased by more than +2.4 MHz for distances of 4 – 50 cm. The +2.4 MHz change occurred at 12 cm. A trend began to occur at the upper frequency band, $f_H = 1650$ MHz, of the antenna as the phantom was moved closer. Once the phantom was moved within 3 cm, the reflection coefficient was always less than -16.7 dB. This will be used as the basis for the operation of the impedance monitoring system discussed in Section 5.3.

The patch facing the phantom was turned off by open circuiting it and terminating its port on the coupler with a matched load. The reflection coefficient of the patch on the opposite side of the ground plane was measured to investigate whether the phantom would affect it. The measured reflection coefficient is shown in Figure 5.3 when the phantom was 1 mm away from the off patch. The two curves almost completely overlap, indicating that when one patch was on and the phantom was on the opposite side of the ground plane there was negligible interaction. This was also confirmed earlier in Section 4.5 when the phantom was placed in the same scenario in the Satimo system with very little change in the radiation pattern occurring.

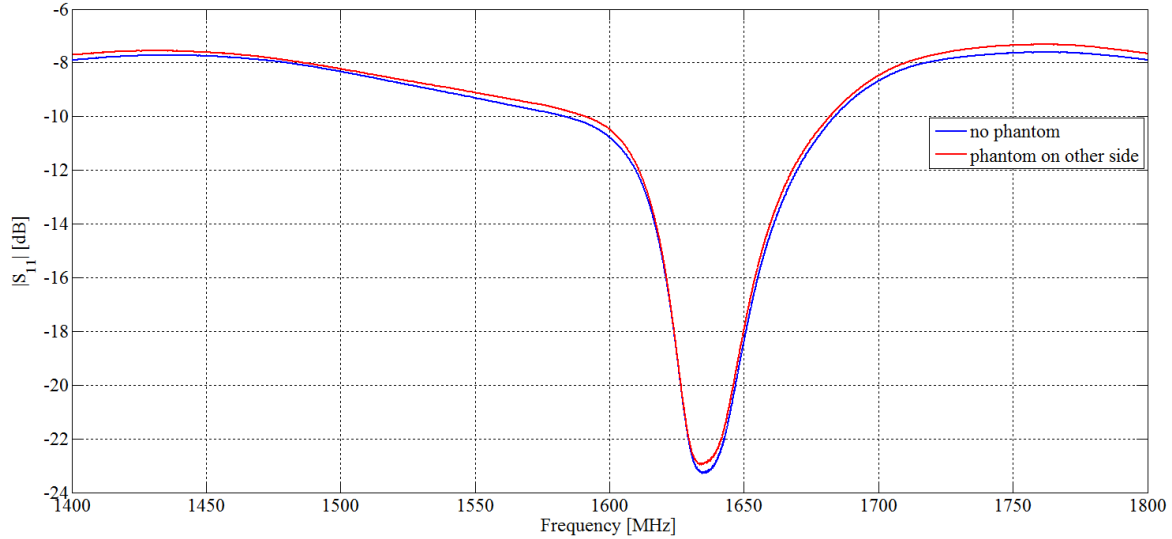


Figure 5.3 *One patch on and one patch off reflection coefficient measured on the VNA. The “blue phantom” was placed 1 mm away from the off-patch side to determine if the phantom influenced the on patch on the opposite side of the ground plane.*

Since there was insignificant change in the input impedance and radiation pattern of the antenna, we can conclude that there would be little interaction with a nearby human body when only the outward facing patch was turned on.

5.3. Operation of the Monitoring System

For the operation of the impedance monitoring system to be feasible with the back-to-back patch antenna designed in Chapter 4, it would first need to be miniaturized to fit within in a handheld device. Assuming this could be done in future work, the initial assumptions for the impedance monitoring system in this thesis are as follows:

1. Impedance monitoring would only occur before the phone transmits
2. Patch 1 would be facing outwards on the front side of the phone and patch 2 would be facing outwards on the back side

3. Only patch 1 would be turned on/off
4. Patch 2 would always be on
5. A user about to start transmitting would have the phone placed up against their head in time for the impedance monitoring system to detect them, otherwise patch 1 would be left on if the person was only sending data or text
6. The antenna would be located at a place on the phone where the user's hand would not cover patch 2

Figure 5.4 gives an example illustration of how the back-to-back patch antenna would be positioned relative to a human user if miniaturized and inside a phone.

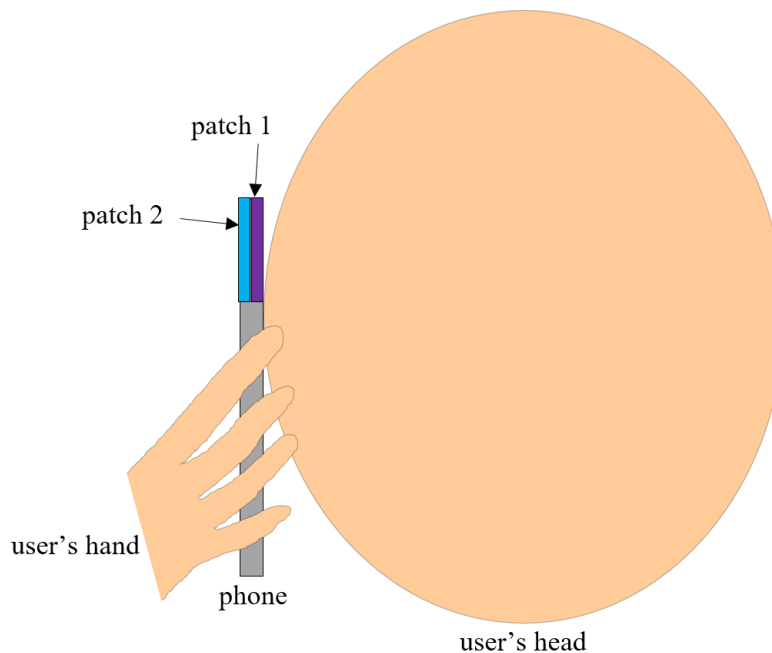


Figure 5.4 An example of a miniaturized version of the back-to-back patch antenna in a phone with a user making a call.

A block diagram of the impedance monitoring system has been shown in Figure 5.5. The through port of the directional coupler would be connected to the phone transceiver, the coupled

port would be connected to a detector and the input port would be connected to the power splitter that goes to the patches. Patch 1 would be connected to a switch that would be terminated in a matched load when the patch is turned off, leaving the patch open circuited. Patch 2 would be connected directly to the output of the splitter and for the case of this thesis would always be left on.

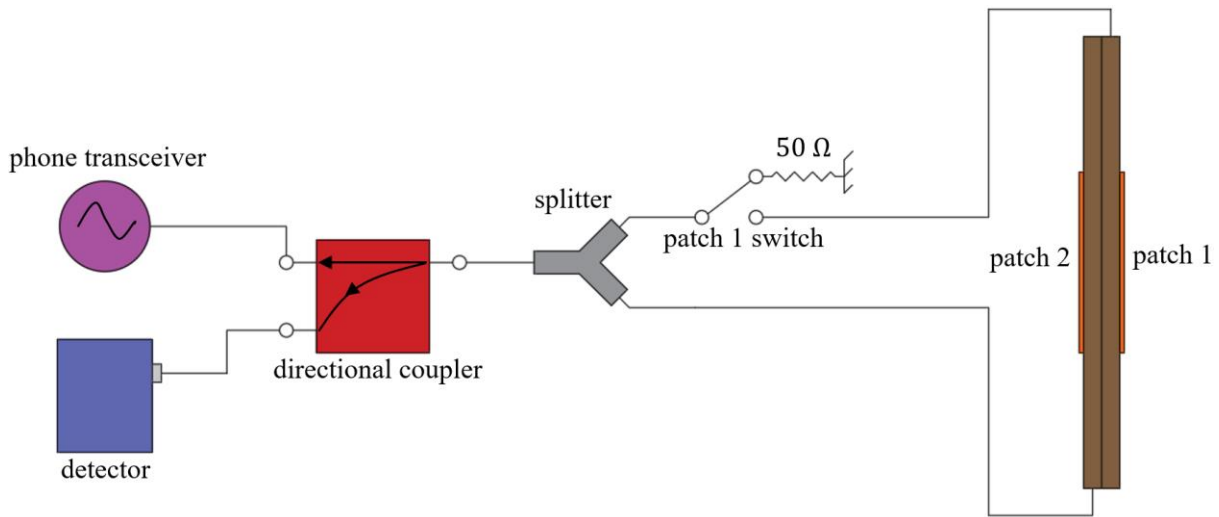


Figure 5.5 High-level block diagram of the impedance monitoring system.

When the phone is not transmitting, both patches would be left on since the power being received from the satellites would be very low due to the large path loss. Any time before the phone was about to transmit, the transceiver would send a single test tone at f_H to determine the power being reflected from the antenna (P_{refl}). The reflected power would be coupled to the detector through the directional coupler. Since the power being reflected from the antenna is related by (5.1), we are effectively measuring the change in input impedance of the antenna.

$$|S_{11}| \text{ [dB]} = 10 \log_{10} \frac{P_{\text{refl}}}{P_{\text{tone}}} = 20 \log_{10} |S_{11}| = 20 \log_{10} \left| \frac{Z_{\text{in}} - Z_0}{Z_{\text{in}} + Z_0} \right| \quad (5.1)$$

$|S_{11}|$ [dB] is the input reflection coefficient magnitude in dB, P_{tone} would be the transmit power of the test tone sent by the transceiver, Z_0 would be the 50 Ω characteristic impedance of the system, and Z_{in} would be the combined impedance of the back-to-back patch antenna system. In Section 4.6, based on the homogenous head phantom, it was determined that SAR levels become unsafe inside 3 cm for a transceiver output power of 2 W. We note that a 2 W transceiver output power is typically the maximum power for an Iridium handheld device [9]. Therefore, the impedance monitoring system would need to turn off patch 1 when it sensed that the user's head was within 3 cm. In the previous Section, it was discovered that a $|S_{11}| < -16.7$ dB at f_H meant the phantom was within 3 cm of the antenna. As a safety buffer, a $|S_{11}| < -15$ dB will be used as the threshold since an inexpensive detector may have an accuracy as poor as ± 1 dB [43]. A $|S_{11}| = -15$ dB is still far enough above the -12.7 dB minimum that occurred outside of 4 cm, which would allow for detector inaccuracies of ± 1 dB. A state diagram of the impedance monitoring system is shown in Figure 5.6.

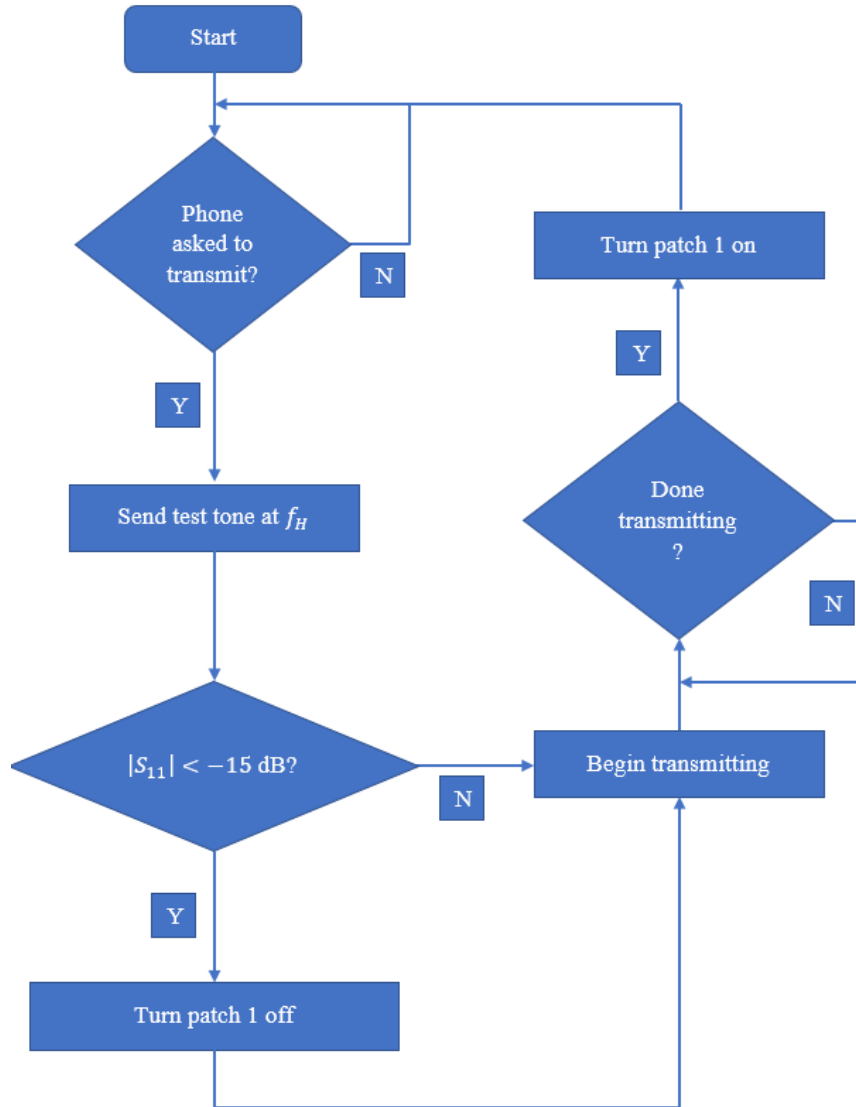


Figure 5.6 State diagram of the operation of the impedance monitoring system.

5.4. Conclusion

In this chapter, an impedance monitoring system for controlling the back-to-back patch antenna was explored. The motivation for this was to adaptively control the antenna to reduce radiation exposure for the human user. Based on the reflection coefficient sensitivity results of the back-to-back patch antenna with the “blue phantom”, a primitive impedance monitoring system was

designed. The system could detect a phantom within 3 cm of the antenna. Any time before the phone was about transmit, the transceiver would be required to emit a single test tone to determine whether a human head was within unsafe distance of the antenna. For data and text, both antennas would likely transmit, however, if the phone was placed up to the head for a call, the patch facing the head would be turned off to stay within SAR limitations.

Chapter 6

Conclusion

A state of the art commercial antenna from Multiband Antennas was measured to provide a blueprint of the radiation properties expected in a mobile Iridium handheld device. The commercial antenna had an omnidirectional pattern with a maximum measured gain of +1 dB and an axial ratio of less than 1.5 dB across a -10 dB bandwidth of 17.5 MHz.

HFSS was used to design a normal-mode helical antenna that mimicked similar characteristics to Multiband Antennas' CSA Stubby model to explore a method of shaping the radiation away from a human head. The normal-mode helix was also fabricated. The reflection coefficient and radiation pattern of the fabricated normal-mode helix was measured. A PEC/PMC based structure was explored for shaping a circularly polarized omnidirectional pattern and a working simulation was created using the designed normal-mode helix. Due to the impractical realization of the PMC, we needed to explore periodic resonant structures called AMCs. An AMC impedance surface model was successfully designed and simulated. Because of the unlikelihood of being able to miniaturize the AMC any further, a back-to-back patch antenna design was explored as an alternative to the adaptive PEC/PMC beam shaping device.

The back-to-back patch antenna design had two separate feeds to allow for on/off control of either patch to minimize radiation exposure to the human user. The back-to-back patch antenna was fabricated and had a -10 dB bandwidth of 27 MHz with a maximum gain of +4.5 dB and an axial ratio of less than 4 dB for an elevation angle $< 70^\circ$ when both patches were on. Since there were no well-defined specifications for mobile handheld satellite devices, the ICAO standard for

Iridium communications was used as a guideline. The ICAO manual specifies that the gain should be greater than -3.5 dB and the axial ratio should be less than 4 dB in the direction of maximum radiation. Therefore, the back-to-back patch antenna has sufficient specifications for Iridium communications. The back-to-back patch antenna was shown to be isolated on each side of the ground plane when a phantom was present on the opposite side of the excited patch with only one patch on. This suggests, that if one of the patches were placed against a human head, it could be shut off and the opposite side patch would have little effect on the human head. It was determined that a distance of at least 3 cm was required between the back-to-back patch antenna and a head phantom to meet SAR regulations for a 2 W transceiver power output. Finally, beam steering of the nulls around the plane of the patches was explored through simulation using different feed phasing between the two patches. It was discovered that a null rotation of 90° occurred for a phase difference of 180° between the feeds.

An impedance monitoring system for adaptively controlling the back-to-back patch antenna was explored. It was determined that the antenna could detect the phantom within 3 cm of it by looking at the reflection coefficient trend at the upper part of the frequency band. Therefore, by shutting off the patch facing the user's head, the system was able to reduce SAR levels to safe levels ($\leq 1.6 \frac{\text{W}}{\text{kg}}$) for a 2 W transceiver power output.

6.1. Future Work

The first thing to explore would be miniaturizing the back-to-back patch antenna to where it could fit within a handheld device form factor. If this was successful, an implementation of the

impedance monitoring system, discussed in Chapter 5, could be fully tested inside a handheld form factor. The effects of a human user's hand on the form factor of the device near the antenna would need to be studied to validate the assumptions in Section 5.3. In [44], a similar approach recently patented by Google discusses the concept of monitoring the reflection coefficient of two or more antennas for adaptively shaping the radiation away from the user to reduce SAR levels. The patent did not show an implementation of the monitoring system with a specific set of antennas.

The impedance monitoring system proposed in this thesis could be tested with two existing commercial patch antennas placed back-to-back. An alternative method of operation for the impedance monitoring system would be to intermittently turn the $+\hat{y}$ - and $-\hat{y}$ - patches on/off and monitor the patch impedances separately. This would allow for on/off control of both patches, which would make the system more adaptive. Using different feed phasing between the two patches of the back-to-back patch antenna could also be explored for adaptive beam steering to optimize signal reception with the satellites and further reduce SAR levels. Another item to explore would be miniaturizing an AMC to the point where it would fit within a handheld device for use with the adaptive PEC/PMC beam shaping device proposed in Chapter 3.

References

- [1] P.W. Lemme, S.M. Glenister, and A.W. Miller, “Iridium aeronautical satellite communications,” *IEEE Aerospace and Electronic Systems Magazine*, vol. 14, no. 11, pp. 11–16, Nov 1999.
- [2] V. Anderson, “Comparisons of peak SAR levels in concentric sphere head models of children and adults for irradiation by a dipole at 900MHz,” *Physics in Medicine and Biology*, vol. 48, no. 20, p. 3263, Sept 2003.
- [3] R. Khanna and R. Saxena, “Adaptive antennas at the mobile handset for reduced radiation hazards: an analysis,” in *IEEE 58th Vehicular Technology Conference*, vol. 5, pp. 3154–3158, Oct 2003.
- [4] *Limits of Human Exposure to Radiofrequency Electromagnetic Energy in the Frequency Range from 3 kHz to 300 GHz*, Industry Canada Safety Code 6, 2015.
- [5] R. Garg *et al.*, *Microstrip Antenna Design Handbook*, Artech House Inc., 2001.
- [6] S. Pratt *et al.*, “An operational and performance overview of the iridium low earth orbit satellite system,” *IEEE Communications Surveys*, vol. 2, no. 2, pp. 2–10, Dec 2009.
- [7] M. Werner *et al.*, “Analysis of system parameters for LEO/ICO-satellite communication networks,” *IEEE Journal on Selected Areas in Communications*, vol. 13, no. 2 pp. 371–381, Feb 1995.
- [8] F. Vatalaro *et al.*, “Analysis of LEO, MEO, and GEO global mobile satellite systems in the presence of interference and fading,” *IEEE Journal on Selected Areas in Communications*, vol. 13, no. 2, pp. 291–300, Feb 1995.
- [9] Solara Remote Data Delivery Incorporated, “Field Tracker 2100,” user’s manual, 2010.
- [10] Certificate of Compliance R&D SAR Evaluation, “SHOUT nano,” RF Exposure Lab, San Marcos, CA, USA, Test report no. SAR.20120617, June 2012.
- [11] R. Gómez-Villanueva, H. Jardón-Aguilar, and R. y Miranda, “State of the art methods for low SAR antenna implementation,” in *European Conference on Antennas and Propagation*, pp. 1–4, Barcelona, Spain, 2010.
- [12] M. Jung and B. Lee, “Sar reduction for mobile phones based on analysis of EM absorbing material characteristics,” in *IEEE Antennas and Propagation Society International Symposium*, Columbus, USA, vo. 2, pp. 1017–1020, June 2003.

- [13] A. Mehrabani, “Low profile spiral antennas over amc ground planes,” MSc. thesis, University of Manitoba, 2008.
- [14] D. Sievenpiper *et al.*, “High-impedance electromagnetic surfaces with a forbidden frequency band,” *IEEE Transactions on Microwave Theory and Techniques*, vol. 47, no. 11, pp. 2059–2074, Nov 1999.
- [15] H. Liu, K. Ford, and R. Langley, “Miniaturised artificial magnetic conductor design using lumped reactive components,” *Electronics Letters*, vol. 45, no. 6, pp. 294–295, Mar 2009.
- [16] S. Kwak, D. Sim, and J. Kwon, “SAR reduction on a mobile phone antenna using the EBG structures,” in *European Microwave Conference*, Amsterdam, Netherlands, pp. 1308–1311, Oct 2008.
- [17] R. Schlub and D. Thiel, “Switched parasitic antenna on a finite ground plane with conductive sleeve,” *IEEE Transactions on Antennas and Propagation*, vol. 52, no. 5, pp. 1343–1347, May 2004.
- [18] A. Sibille, C. Roblin, and G. Poncelet, “Circular switched monopole arrays for beam steering wireless communications,” *Electronics Letters*, vol. 33, no. 7, pp. 551–552, Mar 1997.
- [19] S. Sharma and L. Shafai, “Beam focusing properties of circular monopole array antenna on a finite ground plane,” *IEEE Transactions on Antennas and Propagation*, vol. 53, no. 10, pp. 3406–3409, Oct 2005.
- [20] M. Jacob, J. Long, and D. Sievenpiper, “Non-foster loaded parasitic array for broadband steerable patterns,” *IEEE Transactions on Antennas and Propagation*, vol. 62, no. 12, pp. 6081–6090, Dec 2014.
- [21] H. Liu, S. Gao, and T. Loh, “Circularly polarized electronically steerable parasitic array radiator antenna for satellite,” in *Proceedings of the Fourth European Conference on Antennas and Propagation*, Barcelona, Spain, pp. 1–4, Apr 2010.
- [22] M. Mangoud *et al.*, “SAR reduction for handset with two-element phased array antenna computed using hybrid MoM/FDTD technique,” *Electronics Letters*, vol. 35, no. 20, pp. 1693–1694, Aug 2002.
- [23] B. Toh, R. Cahill, and V. Fucsko, “Understanding and measuring circular polarization,” *IEEE Transactions on Education*, vol. 46, no. 3, pp. 313–318 Aug 2003.
- [24] K. Davies and E. Smith, “Ionospheric effects on satellite land mobile systems,”
- [25] *ICAO Technical Manual for Iridium Aeronautical Mobile Satellite Service*, v1.1, International Civil Aviation Organization, Montreal, QC, Canada, 2006, p. 41.

- [26] D. Chew and S. Saunders, "Meander line technique for size reduction of quadrifilar helix antenna," *IEEE Antennas and Wireless Propagation Letters*, vol. 1, no. 1 pp. 109–11, Feb 2002.
- [27] G. Guo *et al.*, "Design of a quadrifilar helix antenna based on LTCC technology for satellite navigation handset application," in *Antennas and Propagation Asia-Pacific Conference*, Harbin, China, pp. 346–349, Dec 2014.
- [28] J. Hou, X. Sun, and H. Yang, "Design of a high gain quadrifilar helix antenna for satellite mobile communication," in *China-Japan Joint Microwave Conference*, Hangzhou, China, pp. 1–3, Apr 2011.
- [29] A. Balanis, *Antenna Theory*. 3rd ed., John Wiley & Sons, Inc., Publication, 2005.
- [30] J. Kraus, *Antennas*. 2nd ed., McGraw-Hill Book Company, 1988.
- [31] D. Cheng, *Field and Wave Electromagnetics*, 2nd ed., Addison-Wesley Publishing Company, 1989.
- [32] D. Thiel, S. O'Keefe, and J. Lu, "Electronic beam steering in wire and patch antenna systems using switched parasitic elements," in *Antennas and Propagation Society International Symposium*, Baltimore, MD, USA, pp. 534–537, Jul 1996.
- [33] H. Mosallaei and K. Sarabandi, "Magneto-dielectrics in electromagnetics: concept and applications," *IEEE Transactions on Antennas and Propagation*, vol. 52, no. 6, June 2004.
- [34] P. Sharma and K. Gupta, "Analysis and optimized design of single feed circularly polarized microstrip antennas," *IEEE Transactions on Antennas and Propagation*, vol. 31, no. 6, pp. 949–955, Nov 1983.
- [35] F. Chang, K. Wong, and T. Chiou, "Low-cost broadband circularly polarized patch antenna," *IEEE Transactions on Antennas and Propagation*, vol. 51, no. 10, pp. 3006–3009 Oct 2003.
- [36] R. deAssis and I. Bianchi, "Analysis of microstrip antennas on carbon fiber composite material," *Journal of Microwaves, Optoelectronics and Electromagnetic Applications*, vol. 11, no. 1, pp. 154–161, Jun 2012.
- [37] K. Komaki and H. Iwasaki, "Back-to-back patch antenna operated orthogonal polarization for repeater use," in *International Symposium on Antennas and Propagation*, Hobart, Australia, pp. 1–2, Nov 2015.
- [38] H. Iwasaki and N. Chiba, "Circularly polarized back-to-back microstrip antenna with an omnidirectional pattern," *IEE Proceedings – Microwaves, Antennas, and Propagation*, vol. 146, no. 4, pp. 277–281, Aug 1999.

- [39] W. Chen, K. Wong, and C. Wu, "Inset microstripline-fed circularly polarized microstrip antennas," *IEEE Transactions on Antennas and Propagation*, vol. 48, no. 8, pp. 1253–1254, Aug 2000.
- [40] Rogers Corporation, "RT/duroid 5870/5880 high frequency laminates," datasheet, 2016.
- [41] Certificate of Compliance R&D SAR Evaluation, "Radi-Chip with iPhone 5 & iPhone 5s," RF Exposure Lab, San Marcos, CA, USA, Test report no. R&D.20160703, July 2016.
- [42] A. Poston, "Static adult human physical characteristics of the adult head," *Department of Defense Human Factors Engineering Technical Advisory Group*, pp. 72–75, Apr 2000.
- [43] Windfreak Technologies, LLC., "SynthNV," preliminary datasheet, 2014.
- [44] H. Harel *et al.*, "System and method for adaptive beamforming for specific absorption rate control," U.S. Patent 8 422 457, May 14, 2013.

Appendix A

Additional Commercial Antenna Measurements

A second set of helical antennas were received from Multiband Antennas that were supposed to have better tuning than the first set discussed in Chapter 2. Three CSA Stubby and three Embedded CSA Stubby models were donated from Multiband Antennas. The Embedded CSA Stubby had a similar design to the CSA Stubby model, but without the radome covering the top of the antenna. The measurement setup with the VNA was the same as the first set of antennas measured in Chapter 2 and is shown in Figure A.1.



Figure A.1 (a) CSA Stubby mounted on styrofoam while under test. (b) Embedded CSA Stubby mounted on styrofoam under test.

The reflection coefficient plots for the CSA Stubby antennas are shown in Figures A.2 – A.4 and the Embedded CSA Stubby antennas are shown in Figures A.5 – A.7. The resonant frequency and edges of the Iridium band are shown for convenience on each plot.

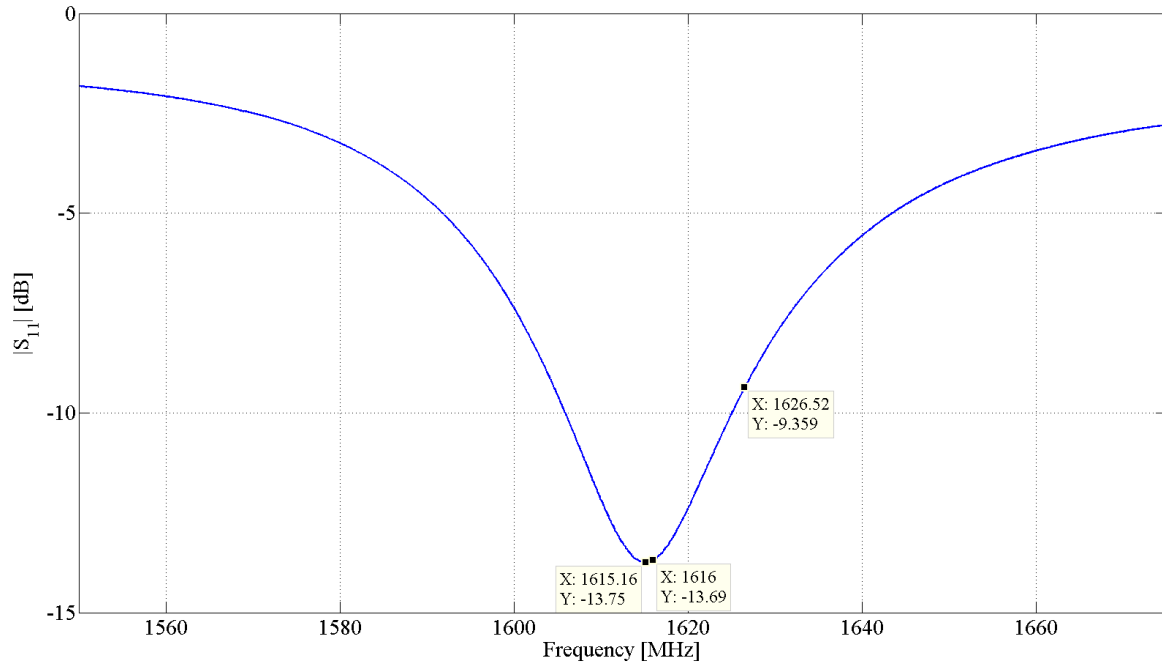


Figure A.2 CSA Stubby 3 reflection coefficient measured on the VNA.

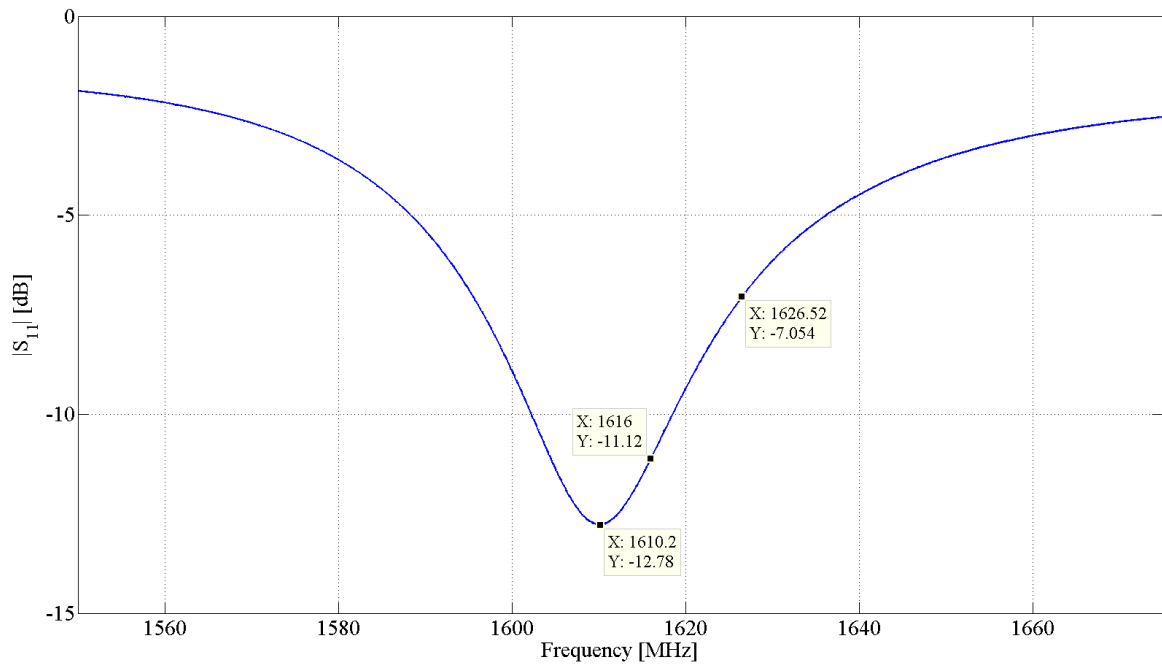


Figure A.3 CSA Stubby 4 reflection coefficient measured on the VNA.

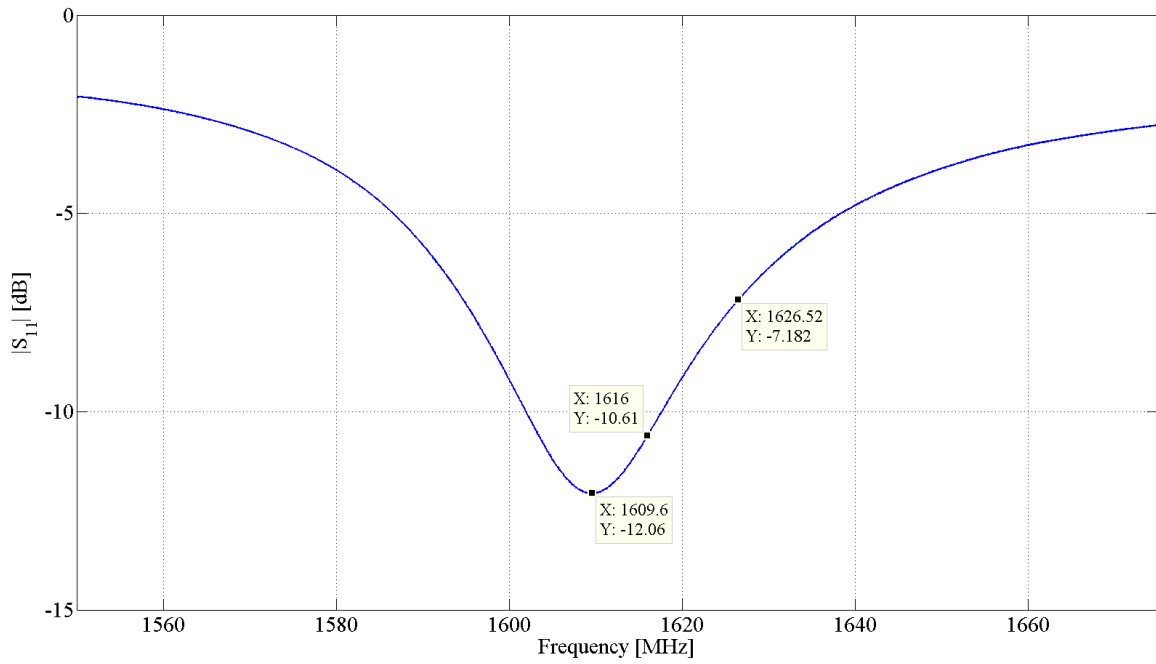


Figure A.4 CSA Stubby 5 reflection coefficient measured on the VNA.

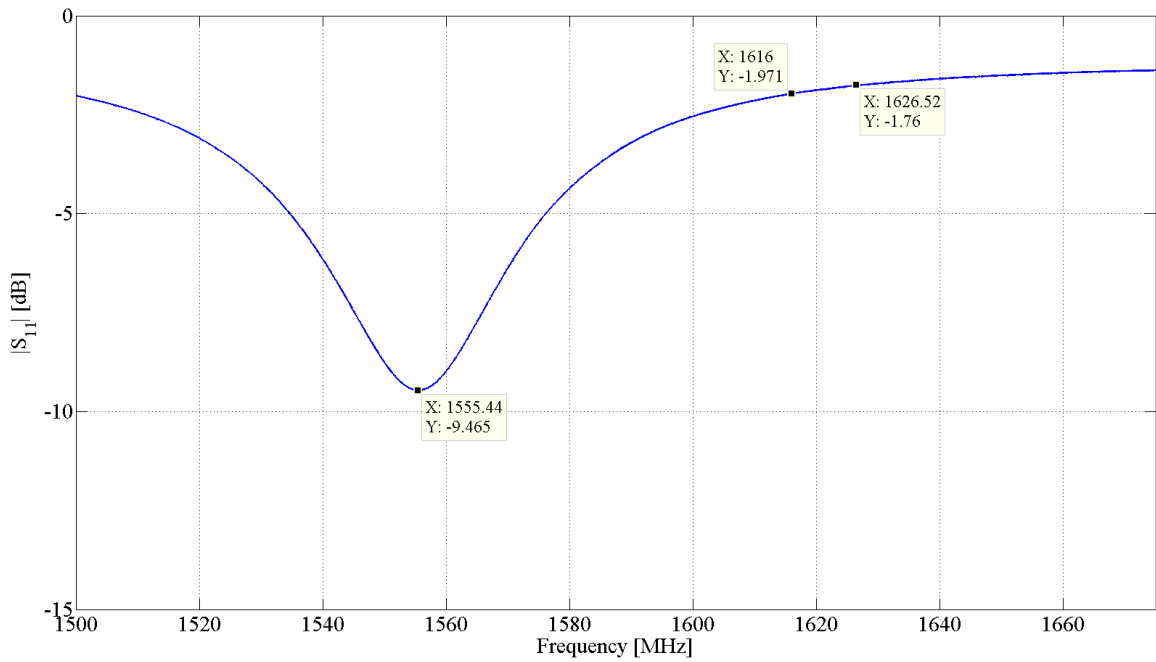


Figure A.5 Embedded CSA Stubby 1 reflection coefficient measured on the VNA.

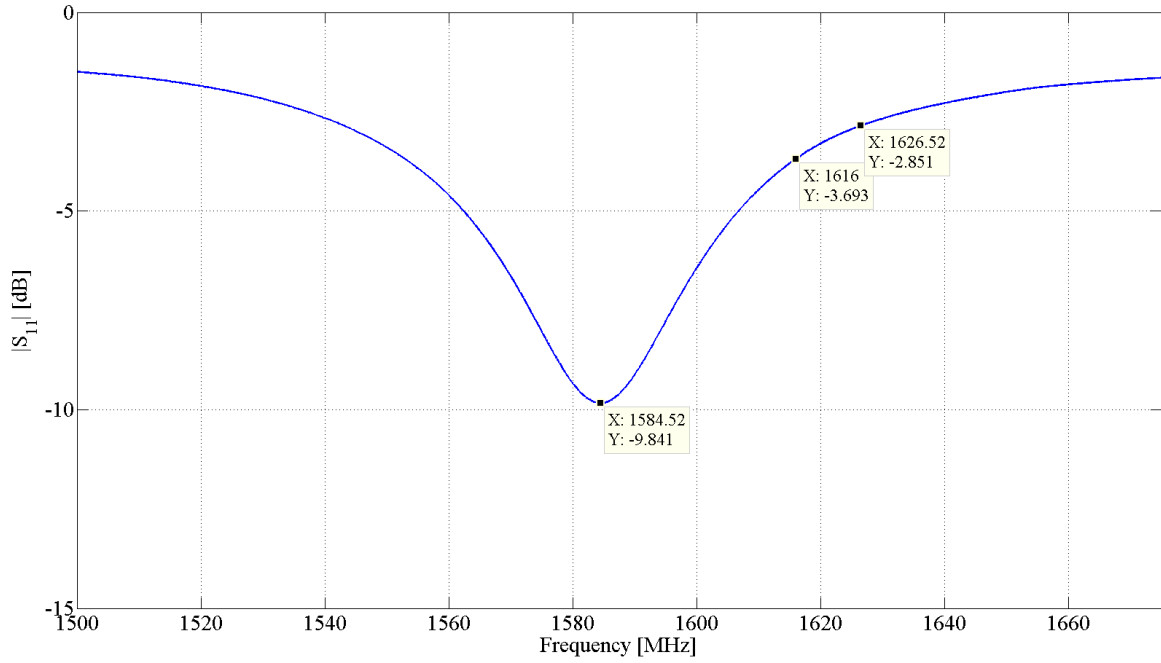


Figure A.6 *Embedded CSA Stubby 2 reflection coefficient measured on the VNA.*

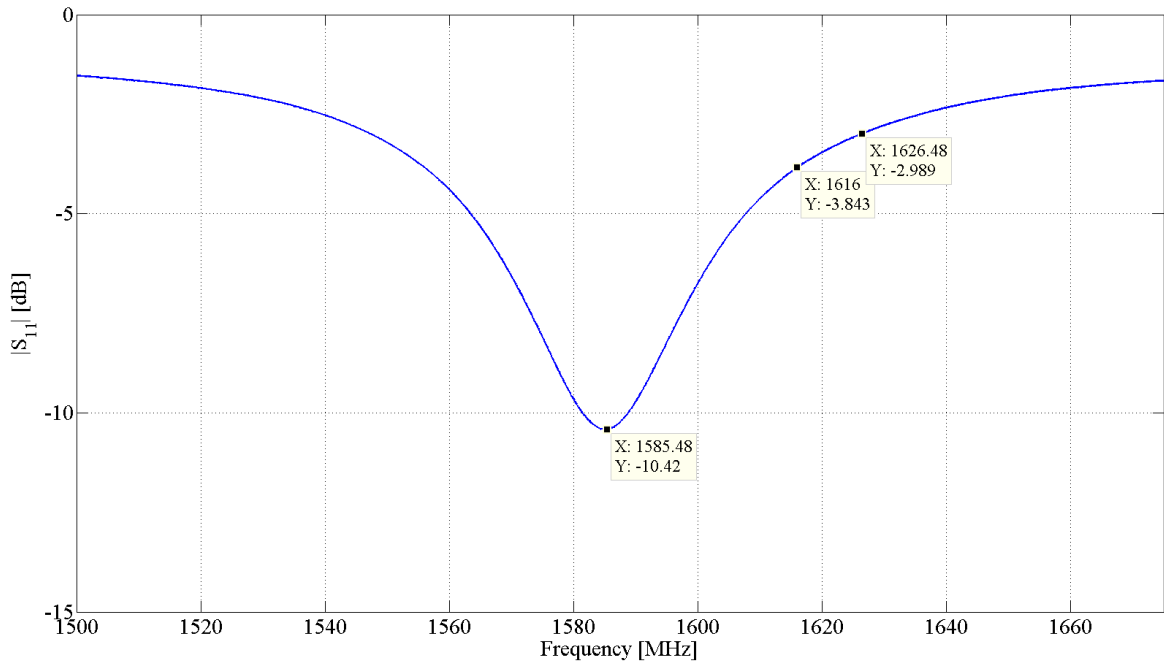


Figure A.7 *Embedded CSA Stubby 3 reflection coefficient measured on the VNA.*